

# Carnegie Mellon University

CARNEGIE INSTITUTE OF TECHNOLOGY

## THESIS

SUBMITTED IN PARTIAL FULFILLMENT OF THE REQUIREMENTS

FOR THE DEGREE OF Doctor of Philosophy

## TITLE

MECHANICAL AND THERMAL CHARACTERIZATIONS OF CRYSTALLINE  
POLYMER MICRO/NANOFIBERS

PRESENTED BY **PENGFEI LI**

ACCEPTED BY THE DEPARTMENT OF  
MECHANICAL ENGINEERING

\_\_\_\_\_  
ADVISOR, MAJOR PROFESSOR

\_\_\_\_\_  
DATE

\_\_\_\_\_  
DEPARTMENT HEAD

\_\_\_\_\_  
DATE

APPROVED BY THE COLLEGE COUNCIL

\_\_\_\_\_  
DEAN

\_\_\_\_\_  
DATE

**MECHANICAL AND THERMAL CHARACTERIZATIONS OF CRYSTALLINE  
POLYMER MICRO/NANOFIBERS**

Submitted in partial fulfillment of the requirements for

the degree of

Doctor of Philosophy

in

Mechanical Engineering

Pengfei Li

B.E., Mechanical Engineering, Shandong University, Jinan, China

M.S., Mechanical Engineering, Washington State University, Vancouver, WA

Carnegie Mellon University  
Pittsburgh, PA

May, 2015

©

Pengfei Li  

---

All Rights Reserved

2015

## **ACKNOWLEDGEMENTS**

I would like to express my appreciation to my advisor, Dr. Sheng Shen (Committee chair), for allowing me the opportunity to work in his research group. This work would not have been completed without his insightful guidance and patience for which I am deeply indebted. In addition to Dr. Sheng Shen, my special thanks also go to the Dowd-ICES Fellowship in 2013, the Berkman faculty development fund, NSF, and DARPA.

I would like to thank Dr. Shi-Chune Yao, Dr. Jonathan A. Malen and Dr. Michael R. Bockstaller for serving on my thesis committee. I would also like to acknowledge Dr. Alan J. H. McGaughey, Dr. Tengfei Luo and Dr. Kedar Hippalgaonkar for their unselfish and unfailing support for this work.

I would like to thank Mr. Ed Wojciechowski and Mr. John Fulmer for their precious insight and valuable assistant. Without their help, I would not continue my research smoothly.

In addition, I would like to express my gratitude to all of my fellow students for their support and friendship. In particular, the encouragement and insight I received from Zonghui Su, Baoan Liu, Jiawei Shi, Ramesh Shrestha, Jinsheng Gao, Lisha Shi, Wee-Liat Ong, Ankit Jain, and Shubhaditya Majumdar, is greatly appreciated. I feel honored to have shared this experience with each of them.

Lastly, my warmest thanks belong to my friends, family and the one beyond everyone of us, our omnipresent Lord, without you, I wouldn't know where I am or where I should go. Thank you so much Lord, for leading me through the misery and offering me the strength. May your name be honored, and glorified.

# **ABSTRACT**

## **MECHANICAL AND THERMAL CHARACTERIZATIONS OF CRYSTALLINE POLYMER MICRO/NANOFIBERS**

by

Pengfei Li

Chair: Sheng Shen

For crystalline polymers, especially those in micro/nanoscale, the number of defects per unit volume is significantly lower than that in the bulk. With extended and aligned polymer chains, the resulting polymer fibers possess remarkably enhanced mechanical and thermal properties and approach the inherent properties of the carbon backbones which form the polymer chains. Together with other unique properties of polymers, such as, low density, easy processability, good biocompatibility, and electrical insulation, the crystalline fibers in micro/nano scale can be used in a broad range of applications, for example, heat spreaders in electronics, high strength ropes, and personnel armors.

This dissertation studies various schemes of polymer crystallization, especially the stress induced crystallization in fiber drawing process. In this work, a two-stage drawing method is finally adopted to produce individual polyethylene (PE) nanofibers. To demonstrate the PE nanofibers possess more enhanced mechanical properties than the commercially available PE nanofibers, an atomic force microscopy (AFM) based force deflection spectroscopy (FDS) technique is explored to characterize the Young's modulus

of the PE nanofibers. By attaching a PE nanofiber onto a specially designed micro trench, and deflecting the nanofiber with an AFM cantilever, we are able to deduce the Young's modulus from the geometry of the trench and the level of deflection on the nanofiber based on Bernoulli's beam equations. The experimentally proved Young's modulus of these nanofibers is 312GPa approaching the theoretical limit of the Young's modulus of PE single crystal.

To study thermal properties of a polysilsesquioxane (PSQ) hybrid crystal, we apply a micro device based thermal characterization method. The micro device consists of two suspended SiNx membranes with built-on Pt coils; the two membranes serve as heater and thermometer during the measurements. The PSQ micro beam is placed between the two membranes. Due to the Joule heating on the heating membrane, heat transfers through the sample to the sensing membrane. By analyzing the steady state heat transfer model, we are able to calculate the thermal conductivity of the PSQ beam. The experimentally measured thermal conductivities greatly help us to understand the heat transfer mechanism in the PSQ hybrid crystal which is formed by hydrogen bonding in the longitudinal direction.

With the same characterization method as used in PSQ thermal characterization, we also measure the thermal conductivity of PE nanofibers. We discover the thermal contact resistance between the nanofiber and the islands is comparable or even bigger than the intrinsic thermal resistance of the PE nanofibers with an assumed thermal conductivity of 20W/mK at room temperature. Cyanoacrylate based super glue and focus ion beam (FIB) assisted Pt deposition are attempted to reduce the thermal contact resistance, however, as demonstrated by the experiments, super glue is likely to lift the nanofiber above the

islands which dramatically increases the thermal resistance. While the FIB assisted Pt deposition introduces great crystal damage on the PE fibers, which results in very low measured thermal conductivities ( $<1\text{W/mK}$ ).



## TABLE OF CONTENTS

<b>ACKNOWLEDGEMENTS .....</b>	<b>ii</b>
<b>ABSTRACT.....</b>	<b>iv</b>
<b>LIST OF TABLES.....</b>	<b>xi</b>
<b>LIST OF FIGURES.....</b>	<b>xii</b>
 <b>CHAPTER 1. Mechanical and thermal transport of crystalline polymeric materials in micro/nano scale .....</b>	 <b>1</b>
<b>1.1 Introduction to polymer crystallization.....</b>	<b>1</b>
1.1.1 Polymer crystallization from a melt and a dilute solution.....	3
1.1.2 Stress-induced polymer crystallization.....	4
1.1.3 Organic-inorganic crystallization by self assembly.....	7
<b>1.2 Mechanical and thermal properties of highly crystalline PE fibers .....</b>	<b>7</b>
1.2.1 Mechanical properties in PE fibers with ultrahigh molecular weight ...	9
1.2.2 Thermal transport in ultrahigh density PE fibers.....	14
<b>1.3 Thermal transport in hydrogen bonded hybrid crystals .....</b>	<b>20</b>
<b>1.4 Motivation and scope.....</b>	<b>24</b>
 <b>CHAPTER 2. Background and Methods.....</b>	 <b>28</b>
<b>2.1 Polyethylene (PE) nanofiber fabrication.....</b>	<b>28</b>
2.1.1 Overview .....	28

2.1.2	Two-stage drawing method .....	31
<b>2.2</b>	<b>Mechanical property characterization for one dimensional materials .....</b>	<b>34</b>
2.2.1	Probing mechanical properties of materials in nano meter scale .....	34
2.2.2	Force deflection spectroscopy .....	36
<b>2.3</b>	<b>Thermal transport characterization for one dimensional polymeric materials</b>	
	47	
2.3.1	Micro devices with suspended structures .....	48
2.3.2	Electrical configuration and thermal model .....	50
2.3.3	Measurement schemes and system characteristics .....	57
 <b>CHAPTER 3. Crystalline polyethylene (PE) nanofibers with the</b>		
<b>theoretical limit of Young's modulus .....</b>		<b>63</b>
<b>3.1</b>	<b>Introduction.....</b>	<b>63</b>
<b>3.2</b>	<b>PE gel preparation and PE nanofiber fabrication.....</b>	<b>65</b>
<b>3.3</b>	<b>Analysis and characterization of the crystal structure of PE nanofibers ....</b>	<b>67</b>
<b>3.4</b>	<b>Young's modulus measurements by the force deflection spectroscopy (FDS)</b>	
method	71	
3.4.1	Verification of the FDS technique with polymethyl methacrylate (PMMA) fibers.....	76
3.4.2	Finite element analysis of the FDS measurement on the PE nanofibers	
	78	

<b>3.5</b>	<b>Results and discussion .....</b>	<b>80</b>
3.5.1	The Young's modulus of PE nanofibers calculated according to the FDS technique.....	80
3.5.2	Size effect of the Young's modulus .....	82
3.5.3	Uncertainty analysis .....	83
<b>3.6</b>	<b>Conclusion .....</b>	<b>85</b>
 <b>CHAPTER 4. Tunable thermal transport in Polysilsesquioxane (PSQ) hybrid crystals .....</b>		
		<b>87</b>
<b>4.1</b>	<b>Introduction.....</b>	<b>87</b>
<b>4.2</b>	<b>PSQ synthesis and characterization .....</b>	<b>88</b>
<b>4.3</b>	<b>Thermal characterization with suspended micro thermal device.....</b>	<b>93</b>
4.3.1	Experiment setup and measurement scheme .....	94
4.3.2	Precision placement of PSQ beam onto the thermal device .....	95
4.3.3	Thermal conductivity measurement results and discussion .....	100
<b>4.4</b>	<b>Non-equilibrium molecular dynamics simulations of PSQ thermal conductivities .....</b>	<b>103</b>
<b>4.5</b>	<b>Conclusion .....</b>	<b>108</b>
 <b>CHAPTER 5. Thermal conductivity of individual crystalline polyethylene (PE) nanofibers.....</b>		
		<b>110</b>
<b>5.1</b>	<b>Introduction.....</b>	<b>110</b>

5.2	Sample preparation and measurement scheme .....	111
5.3	Experiment results and discussion .....	112
5.3.1	Thermal contact resistance between the nanofiber and the islands without adhesion materials .....	114
5.3.2	PE nanofibers clamped with cyanoacrylate super glue .....	118
5.3.3	PE nanofibers clamped by focus ion beam (FIB) assisted platinum deposition .....	120
5.4	Conclusion .....	124
<b>CHAPTER 6. Conclusions and outlook .....</b>		<b>126</b>
6.1	Conclusions .....	126
6.2	Outlook and future work .....	129
<b>References .....</b>		<b>130</b>

## LIST OF TABLES

Table 3-1 FDS performed on PMMA fibers.....	77
Table 3-2 Elasticity Matrix (in GPa) for the material property used in FEA model .....	79
Table 4-1 Initial structure and optimized structure for C6 and C8 .....	104
Table 4-2 Thermal conductivity of PSQ beams with different molecular backbone lengths at 300K.....	106

## LIST OF FIGURES

Figure 1-1 Thermal conductivity versus Young's modulus for a wide range of materials.

The figure is plotted with CES selector from Granta Design Ltd. One goal of this research is to explore a fabrication method to enhance the thermal conductivity and Young's modulus, ultimately to make polymers acquire properties that are comparable to those of metals and alloys as indicated by the arrow. .... 2

Figure 1-2 PE crystallization from a melt. First the PE powders are melted to above 140°C, the PE coils (a) are randomly dispersed in space. When the melt is subject to a super cooling, PE chains partially fold into lamellar structures (b). If the crystallization continues, lamellar structures further grow into spherulites (c). .... 4

Figure 1-3 Polymerization of PE. (a) Ethylene monomer. (b) A repeating unit formed by breaking the double bond of ethylene molecule. (c) A PE chain comprised of covalently connected carbon atoms with two hydrogen atoms attached. .... 8

Figure 1-4 Relation between the Young's modulus and the draw ratio for ultra molecular weight PE under two initial crystallization conditions, the triangles represent the original PE was quenched immediately into water after melting. The dots represent a slow cooling and quenching pretreatment for the molten PE. The figure is modified from reference [23]. .... 10

Figure 1-5 A schematic of microfibrils which contain crystalline blocks with length  $L_d$  and disordered regions with length  $L_d$ , the disordered regions are collections of tout tie molecules, chains ends and amorphous regions. The figure is modified from reference [25]. .... 11

Figure 1-6 Plot Young's modulus of a PE fiber versus TTM fraction $\beta$ in the disordered region, the figure is modified from reference [24]. .....	14
Figure 1-7 Modified from reference [32]. (a) A thermal model of a PE fiber section containing both crystalline and amorphous regions. Where, $y$ is the length percentage of the crystalline region in part I, $1-y$ is the length percentage of the amorphous region in part II, and $x$ , $1-x$ are the width percentages of part I and part II respectively in the fiber section. (b) A thermal circuit representation of the thermal model in (a).....	19
Figure 1-8 (a) A 3D graph of a PSQ bimolecular ring which is composed of 16 carbon atoms, 4 silicon atoms, and 2 oxygen atoms. (b) A 2D projection of a PSQ crystal structure formed by the van der Waals force which binds the sides of the rings and hydrogen bonds which connect the ends of the bimolecular rings. The longitudinal crystal direction is along the carbon chains. The blue circled hydrogen and oxygen are atoms that form hydrogen bonds with molecules in and out paper directions.....	23
Figure 2-1 Schematic of a nanofiber fabrication setup. The heater represented by the red block heats the PE gel to a temperature of $120^{\circ}\text{C}$ which is beyond the melting temperature of PE crystals. The hot plate heats the surrounding air to $90\sim 100^{\circ}\text{C}$ which expedites the solvent evaporation during the drawing process.....	33
Figure 2-2 Silicon trenches fabricated with conventional photolithography and inductively coupled plasma RIE etching. ....	39
Figure 2-3 (a) An optical graph of a PE nanofiber clamped by adhesives and separated to sections marked by white circles where the nanofiber is suspended over the	

micro-fabricated silicon trench, the scale bar is 10 $\mu$ m. (b) An AFM image of the PE nanofiber in (a), the relatively white part in the image represents a little portion of the adhesives, the scale bar is 1 $\mu$ m. ....	41
Figure 2-4 A FD curve obtained on a bare silicon substrate. (a) A cartoon of an AFM cantilever approaching (black arrow) to and retracting (red arrow) from the substrate. (b) A FD curve corresponding to the movement of the cantilever described in (a), with the black curve for approaching and the red curve for retracting. ....	44
Figure 2-5 FD curves of PE nanofiber and rigid silicon substrate. F is the concentrated load applied at the midpoint of the suspended PE fiber or solely on the silicon substrate. Z is the height of the AFM cantilever base. The blue curve represents a total deflection from the AFM cantilever itself and the PE nanofiber. The red curve is the calibration curve which only includes the deflection of the AFM cantilever when it contacts the rigid silicon surface. ....	45
Figure 2-6 An SEM image of a micro device with two suspended islands. The two islands are identical with Pt coils and legs fabricated on the top surface and a bottom SiNx layer as the supporting substrate.....	50
Figure 2-7 Electrical connections of the thermal device for thermal conductivity measurement. The red colored line represents a DC current path which heats the SiNx substrate due to the Joule heating effect. The blue colored line stands for samples to be measured. ....	51
Figure 2-8 Thermal model based on the electrical connections in figure 2-7. ....	53



Figure 2-9 (a) The resistance changes of the heating island $R_{hi}$ and the sensing island $R_{si}$ with time during the cooling down process. (b) The global temperature change of heat sink $T_{hs}$ with time. (c) The resistance changes of the heating island $R_{hi}$ and the sensing island $R_{si}$ with global temperature $T_{hs}$ . .....	60
Figure 2-10 Temperature change (dashed line) measured by the thermal diode and the resistance change (black line) of the heating coil while the global temperature switches from 260K to 270K. The arrows indicate the point where heat transfer reaches to a steady state. ....	61
Figure 3-1 (a) AFM image of a PE nanofiber fabricated through two-stage heating process. (b) An AFM height curve corresponding to (a). The labeled height $d$ is a representation of the diameter of the PE nanofiber. The rough surface is a result of reactive ion etching (RIE) of the silicon substrate during the trench fabrication. The scale bar is $1\mu\text{m}$ . ....	66
Figure 3-2 (a) Semi-crystalline PE gel with crystalline and amorphous regions. (b) PE molecular chains dissolved in Decalin solvent. The PE chains are randomly entangled in the solution. (c) Crystalline PE nanofiber with aligned chains. ....	68
Figure 3-3 (a) A PE nanofiber with a diameter of 80.9nm lying on a bare silicon substrate. (b) TEM SAED pattern of the PE nanofiber in (a) which represents an orthorhombic crystal structure of the nanofiber. (c) A thick PE microfiber with a diameter of $1.05\mu\text{m}$ . (d) A SAED pattern of the microfiber in (c) shows continuous rings. These rings indicate a polycrystalline crystal structure of the thick PE microfiber. And the polycrystalline crystal structure is due to the random orientation of the lamellae in the thick PE microfiber. ....	70

Figure 3-4 (a) AFM image of a typical PE nanofiber suspended over a silicon trench. (b) 3D model of the experimental setup for the FDS technique. (c) FD curves (approach and retraction) obtained on a silicon substrate and the middle point of a PE fiber over a trench. ....	74
Figure 3-5 (a) A typical PMMA fiber suspended over a silicon trench. (b) FD curves obtained on a silicon substrate and the middle point of a PMMA fiber over a trench.....	77
Figure 3-6 (a) Orthorhombic crystal structure of PE. FEA simulations on a PE fiber 102nm in diameter, assuming the fiber is (b) anisotropic and (c) isotropic. The color bar represents the deflection of the fiber in meters.....	80
Figure 3-7 Young's moduli measured for PE nanofibers ranging from 70nm to 260nm in diameter. The average measured Young's modulus indicated by the dash line is 312GPa $\pm$ 108GPa.....	82
Figure 4-1 2D projection graphs of repeating units of (a) octylene-bridged and (b) hexylene-bridged PSQ fibers. Dark field optical images of PSQ products, Octylene-bridged PSQ microbeam (c) crystalline; (e) Amorphous. Hexylene - bridged PSQ microbeam (d) crystalline; (f) Amorphous.....	90
Figure 4-2 (a) Fourier transform infrared spectroscopy (FTIR) spectra of crystalline and amorphous bridged PSQ. (b) Powder X-ray diffraction pattern of octylene-bridged PSQ fibers. ....	92
Figure 4-3 Optical image of a PSQ crystal fiber placed on a suspended micro device with built-in platinum resistance thermometers. The scale bar is 2mm.....	95

Figure 4-4 (a) A SEM image PSQ cluster after a sol-gel process. Water produced during the condensation pulls the PSQ crystal beams together due to a strong surface tension. (b) PSQ crystal beams separated by sliding a glass substrate on top of the PSQ cluster.....	98
Figure 4-5 (a) The total thermal resistance measured versus $L_s/A_{cr}$ in 5 samples at 50K and 300K. (b) Thermal conductivity of both type PSQ fibers at temperatures from 10K to 320K.....	102
Figure 4-6 A Representative NEMD Setup for Thermal Conductivity Calculation.....	105
Figure 4-7 (a) Thermal conductivity of PSQ-C6 as a function of the beam Length. (b) Thermal conductivity of PSQ-C6 from 200K to 400K. (c) Measured thermal conductivities of PSQ-C6 and PSQ-C8 in the temperature range from 250K to 310K.....	108
Figure 5-1 A PE fiber placed on the micro device with suspended islands and legs. The fiber is clamped at both ends with cyanoacrylate based super glue. The scale bar is 10 $\mu\text{m}$ . ....	112
Figure 5-2 Thermal resistance network for steady state heat transfer on the micro device with a PE fiber incorporated. $R_{c1}$ is the thermal contact resistance between the nanofiber and the heating island, $R_{c2}$ is the thermal contact resistance between the nanofiber and the sensing island, and $R_s$ is the thermal resistance of the measured nanofiber. ....	113
Figure 5-3 Total thermal contact resistance plot against contact length $l_c$ (a) and the line contact width $2b$ (b) based on equation 5.1 and 5.2.....	116

Figure 5-4 Thermal conductivities of a PE nanofiber placed on the thermal device with no additional bonding materials.....	118
Figure 5-5 Measured thermal conductivities for two samples clamped by super glue, sample 1 (a), and sample 2 (a). ....	119
Figure 5-6 (a) and (b) are two typical samples bonded with FIB assisted Pt deposition; the circled areas are contaminated by the Pt atoms. (c) A close look of a PE nanofiber clamped on the islands by Pt blocks. ....	122
Figure 5-7 Plots of thermal conductivity versus temperature for two PE samples bonded on the micro device with FIB assisted Pt deposition. ....	123

# **CHAPTER 1. Mechanical and thermal transport of crystalline polymeric materials in micro/nano scale**

## **1.1 Introduction to polymer crystallization**

Polymers play an essential and ubiquitous role in everyday life from vulcanized rubber for tires, Teflon for non-stick pan coatings, Nylon for clothes, to polyethylene (PE) for packaging bags and many more, due to their broad range of properties. Compared to other commonly used materials such as metals and ceramics, polymers have a wealth of unique properties: light, inexpensive and easy for processing. However, as shown in figure 1-1, the Ashby chart tells us bulk polymers exhibit very low Young's moduli below 10GPa [1] and trivial thermal conductivities on the order of 0.1W/mK [2], mainly because these bulk polymeric materials are usually amorphous and filled with voids and impurities. As a result, bulk polymers are normally used in applications without high mechanical strength requirement, and regarded as thermally insulating materials.

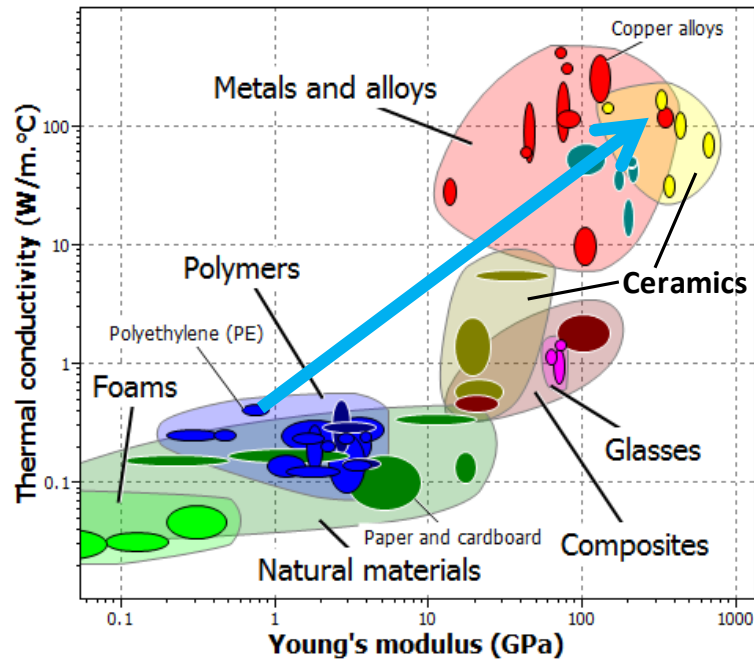


Figure 1-1 Thermal conductivity versus Young's modulus for a wide range of materials. The figure is plotted with CES selector from Granta Design Ltd. One goal of this research is to explore a fabrication method to enhance the thermal conductivity and Young's modulus, ultimately to make polymers acquire properties that are comparable to those of metals and alloys as indicated by the arrow.

Nevertheless these weak properties are not the inherent characteristics of polymers, especially, when we consider the polymers are comprised of long molecular chain with carbon-carbon covalent bonds as intramolecular force. Some materials made of the carbon-carbon chain molecules are reported with exceptional mechanical and thermal properties. For example, the exfoliated pristine graphene, one layer of carbon atoms  $sp^2$ -bonded in a hexagonal pattern, has an estimated Young's modulus of  $2.4 \pm 0.4$  TPa [3] and a room temperature value of thermal conductivity about 4840~5300 W/mK [4]. Similarly,

carbon nanotubes which are rolls of graphene sheets, possess a Young's modulus as high as 1.8TPa [5] and a thermal conductivity over 3000W/mK [6] at room temperature.

In order to harness the high strength and high thermal conductance of the carbon-carbon covalent bond in polymeric materials, especially for those isotactic and syndiotactic polymers which usually crystallize, the long carbon-carbon chains have to be extended and aligned to form crystals. As a result of crystallization, the amount of amorphous regions and defects is greatly reduced, therefore, less stress concentration and less phonon scattering sites lead to a great enhancement on the mechanical strength and thermal conductivity. However, in the bulk, the long carbon-carbon chains are never fully extended but entangled, and only part of the chains are involved in crystalline form which is usually termed as lamella structure, for which even the simplest isotactic polymer, PE is semi-crystalline in bulk.

### 1.1.1 Polymer crystallization from a melt and a dilute solution

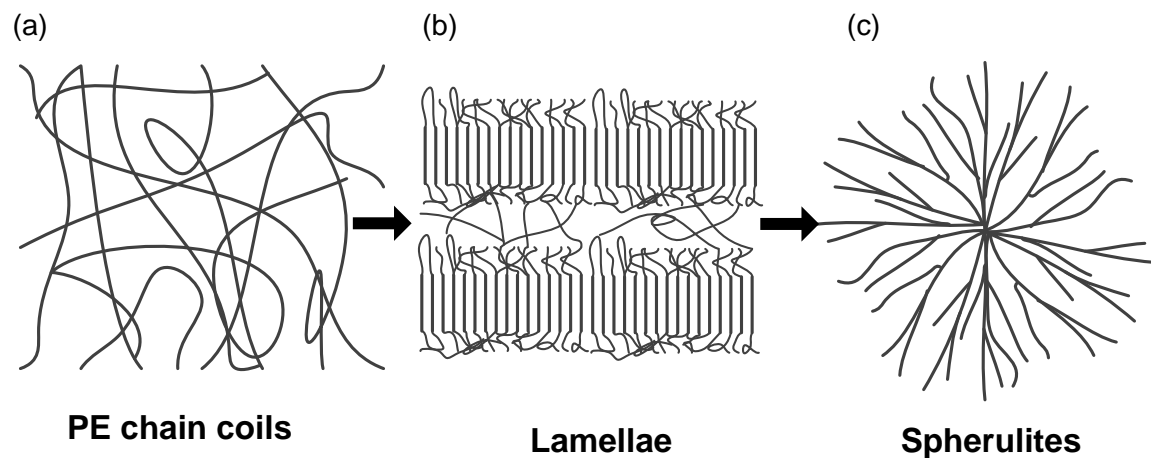


Figure 1-2 PE crystallization from a melt. First the PE powders are melted to above 140°C, the PE coils (a) are randomly dispersed in space. When the melt is subject to a super cooling, PE chains partially fold into lamellar structures (b). If the crystallization continues, lamellar structures further grow into spherulites (c).

Despite polymers in bulk form can never be fully crystalline, through some controlled crystallization processes, the crystallinity of polymers can be greatly enhanced. For example, PE crystallization from a melt [2] under a super cooling temperature 10~20°C below the melting point, PE chains tend to fold into lamella structure, these lamellar crystalline plates further grow into spherulites as shown in figure 1-2. Another method to obtain polymer crystals is to crystallize polymers in dilute solution. Single crystals of PE were formed in tetrachloroethylene. And the lamellar platelets are about several tens of  $\mu\text{m}$  in width and 10~20 nm in thickness [7]. The dimensions of these single crystals are usually larger than the lamellar structures obtained from polymer melts. In the very dilute solutions, the long polymer chains have less chance to touch and entangle with others, therefore, well separated polymer chain coils dispersed in the solution favorably form single crystals with sizes larger than the lamellae from polymer melts. As the concentration of the solution increases, the interactions between polymer chains become stronger and close to those in polymer melts, thus multilayered dendritic structures are frequently observed.

### **1.1.2 Stress-induced polymer crystallization**

Although the highly crystalline structures, such as lamellae, spherulites, and single crystals, are easily demonstrated in previous experiments [8]–[12], these structures are



mostly used in research to study their growth kinetics under various conditions, crystal nucleation theory, or a specific crystal structure of a polymer. These small size crystalline structures cannot be easily adopted for practical applications. To solve this dilemma, researchers have extensively studied another type of polymer crystallization, the stress-induced crystallization, in which, the polymer chains are aligned and oriented under extremely large deformations when external force is applied. The external force during the crystallization process enables a relative movement of the polymer chains, and therefore a great shear stress between molecules helps to align and orientate the long chains in the force direction.

As a typical example of the stress-induced crystallization, polymer films [13]–[15] and fibers [16]–[18] manufactured by an ultra-drawing method have both experimentally and theoretically been proved high Young's modulus and high thermal conductivity, due to the greatly increased crystallinity within these films and fibers. In the ultra-drawing method, a polymer crystal mat prepared by surface growing technique or crystallization in a dilute solution, is heated at a temperature above its melting temperature. This allows the polymer chains to be unfolded and extended from the original lamellar structures. A polymer gel is also commonly used in the ultra-drawing method. In the gel, the solvent swells the polymer chains and greatly reduces the entanglement density. By drawing the gel, the polymers chains are oriented and extended in the drawing direction. However, the gel solution cannot be too dilute. A very low concentration causes few entanglements, and the interactions between polymers chains are too weak to fully extend the polymer chains. For the ultra-drawing method, the polymers used are required to have high molecular weight which ensures a long polymer chains, because short polymer chains

have less distance for friction effect, and the short chains can easily slide away from each other, which greatly reduces the drawability/drawing ratio [13].

The highly crystalline polymers with enhanced mechanical and thermal properties have been found in a wide range of applications. For example, Honeywell Spectra fibers are used to make protective armors due to their extremely high Young's modulus and low density. Composites are also made with these fibers as Spectra Shield® ballistic materials. Tensile structures, such as ropes and cables with various dimensions, are also made with high strength polymer fibers. Applications of these polymers are also found in medical field for implantable devices, due to their compatibility to human body, high strength/softness and great wear resistance [19]. Another important potential of the polymers with high thermal conductivity is the heat transfer application, including heat sinks, heat exchanges. The ever-soaring energy density of the electronic chips produces large amount of heat during operation, for example, 64-bit dual-core Intel Xeon® 7041 Processor has a power dissipation of 165W [20]. For electronic heat dissipation, a highly thermally conductive and electrically insulating thermal interface material is long desired. Crystalline polymer fibers with enhanced thermal properties will be a great candidate to replace the current epoxy materials with high thermal resistance.

With the knowledge of stress-induced polymer crystallization and the great potential on various applications, intensive research had been done to increase the crystallinity and characterize the crystalline polymers, especially polymer fibers. However, the polymer fibers reported by previous research are either in micrometer scale or with a large amount of defective regions. One goal of this research is to produce polymer fibers in nanoscale and to study their mechanical and thermal properties.

### **1.1.3 Organic-inorganic crystallization by self assembly**

The previous two sections mentioned three mechanisms of crystallization, and the produced polymer crystals possess extraordinary enhancements on their physical properties. Yet there is another crystallization mechanism, the self assembly of organic fragments during a sol-gel process, which is less expensive and does not involve intensive fabrication processes, compared with the previous crystallization methods. Within this self-assembly method, two hydrolyzed monomers undergo one-step condensation forming bimolecular rings. The hydrogen bonds and van der Waals force align and connect the rings to create a three dimensional molecular crystalline structures. The self-assembled hybrid crystals have extremely high crystallinity [21]. Even though a lot of efforts have been devoted to the study of the crystallization mechanism and the characterization of the crystal structure, little is known about the thermal transport within this hydrogen bond linked crystals, and therefore we aim to implement novel thermal characterization methods to study the effect of hydrogen bonds on the thermal properties of crystalline materials. This is another goal of the research.

## **1.2 Mechanical and thermal properties of highly crystalline PE fibers**

PE ( $C_{2n}H_{4n+2}$ ), is polymerized from ethylene monomers, as shown in figure 1-3, with proper catalysts, the double bond of ethylene monomers (figure 1-3(a)) breaks and forms one repeating unit which is illustrated in figure 1-3(b). The repeating unit forms strong  $\sigma$ -bonds with its neighboring units, which finally leads to a long molecular chain in figure 1-3(c), the macromolecule of PE. The PE molecule consists of covalently linked carbon backbones with two pendant hydrogen atoms attached to each carbon atom. If a polymer chain doesn't contain branching or cross linking, we call the polymer as a linear polymer.

PE is a typical linear polymer, especially the high density PE, has a very low concentration of defects and a low level of branching, and thus a very high degree of crystallinity can be achieved.

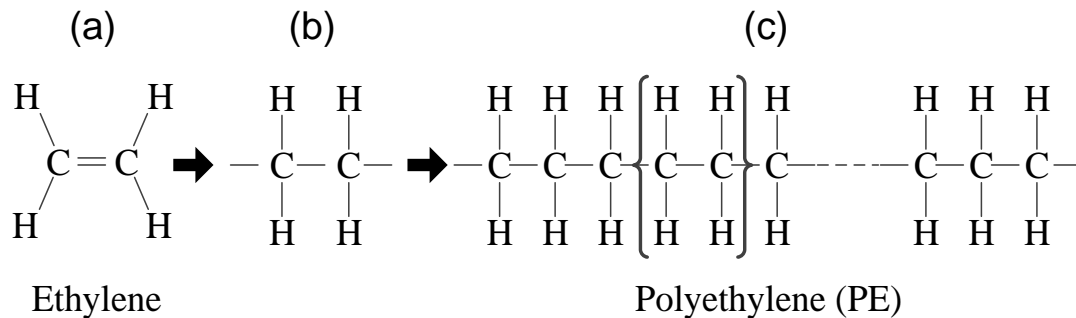


Figure 1-3 Polymerization of PE. (a) Ethylene monomer. (b) A repeating unit formed by breaking the double bond of ethylene molecule. (c) A PE chain comprised of covalently connected carbon atoms with two hydrogen atoms attached.

Due to its extraordinary variability on the semicrystalline morphology, the molecular weight, molecular weight distribution, comonomer type, and comonomer content, PE has been regarded as one of the most common plastics. For example, low density PE (Density, 0.91-0.94 g/cm<sup>3</sup>) has a low degree of crystallinity corresponding to a low melting point, and the resulting product is flexible with reasonable tensile strength. These characteristics have made low density PE useful in applications such as low load packaging and waterproofing. High density PE has a much higher degree of crystallinity (55-77%), which enables the products of high density PE to be very stiff and impermeable. In contrast to the low density PE, the high density PE has been widely used in high load applications such as varieties of water containers, chemical storage tanks, and gas pipes. Because the high linearity of the long PE molecules, upon controlled processes, such as

extrusion, ultra drawing and spinning, the molecular chains can be perfectly oriented and aligned in a parallel fashion, the resulting PE fibers can have mechanical and thermal properties approaching the theoretical limits. These strong fibers are woven to ropes and sheets which have already been applied in sports, military, aviation industries.

### **1.2.1 Mechanical properties in PE fibers with ultrahigh molecular weight**

Because PE fibers contain greatly extended molecular chains with high degree of crystallinity, the mechanical properties of these fibers are enormously enhanced compared with other products derived from PE. Intensive research has been done to study the mechanical properties of PE fibers in micro/nano scale produced in various methods, these fabrication methods will be discussed with details in Section 2.1. Mechanical properties include both tensile properties and compressive properties. For PE fibers, the properties under tension at the axial direction are most interesting due to its practical applications such as wires, ropes, and bullet-proof vests. Therefore, in this section, the tensile properties is mainly discussed, especially the Young's modulus, which is also sometimes regarded as, initial modulus, tensile modulus, elastic modulus or elastic constant. For a PE fiber subjects to an elongation force along the axial direction, Young's modulus is defined as the ratio of the elongational stress to the resulting strain where Hooke's law holds.

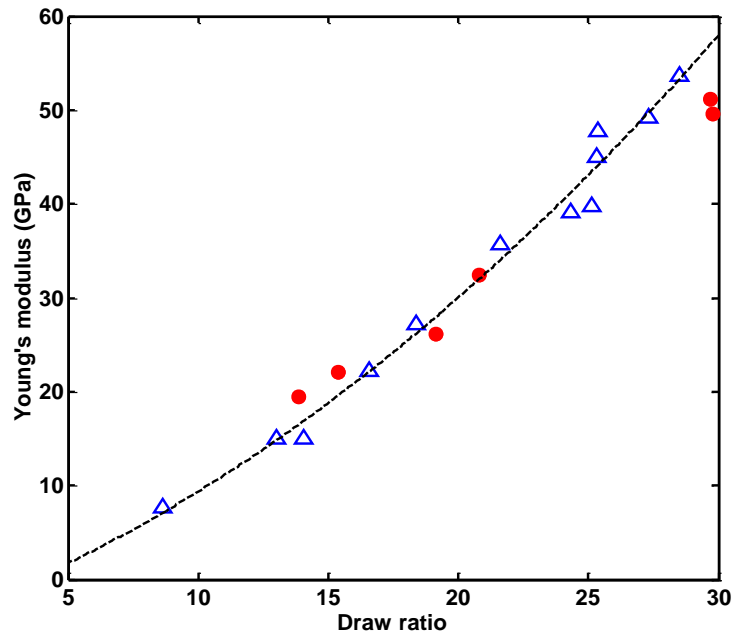


Figure 1-4 Relation between the Young's modulus and the draw ratio for ultra molecular weight PE under two initial crystallization conditions, the triangles represent the original PE was quenched immediately into water after melting. The dots represent a slow cooling and quenching pretreatment for the molten PE. The figure is modified from reference [23].

As reported by previous research, for ultra high molecular weight PE fiber, it's Young's modulus is strongly affected by the draw ratio, a reduction ratio of the cross-sectional areas before and after the fiber drawing [22]. Figure 1-4 shows an approximately linear proportionality between the Young's modulus and the draw ratio [23]. As the draw ratio increase, the melting temperature of the PE fiber increases, which reveals an increased crystallinity in the fiber [22]. When the draw ratio reaches 30, the Young's modulus of the PE fiber is more than 50 GPa. More interestingly, the draw ratio effect is not

influenced by the initial crystallization situations, as shown in figure 1-4, the PE melt that undergoes a slow cooling produces little deceivable crystal structures like spherulites, while a large amount of spherulites can be found in the water quenched PE melt due to the solution's higher viscosity at low temperature. The effect of draw ratio on the Young's modulus gives us a clear direction for making PE fibers with a Young's modulus approaching the theoretical limit.

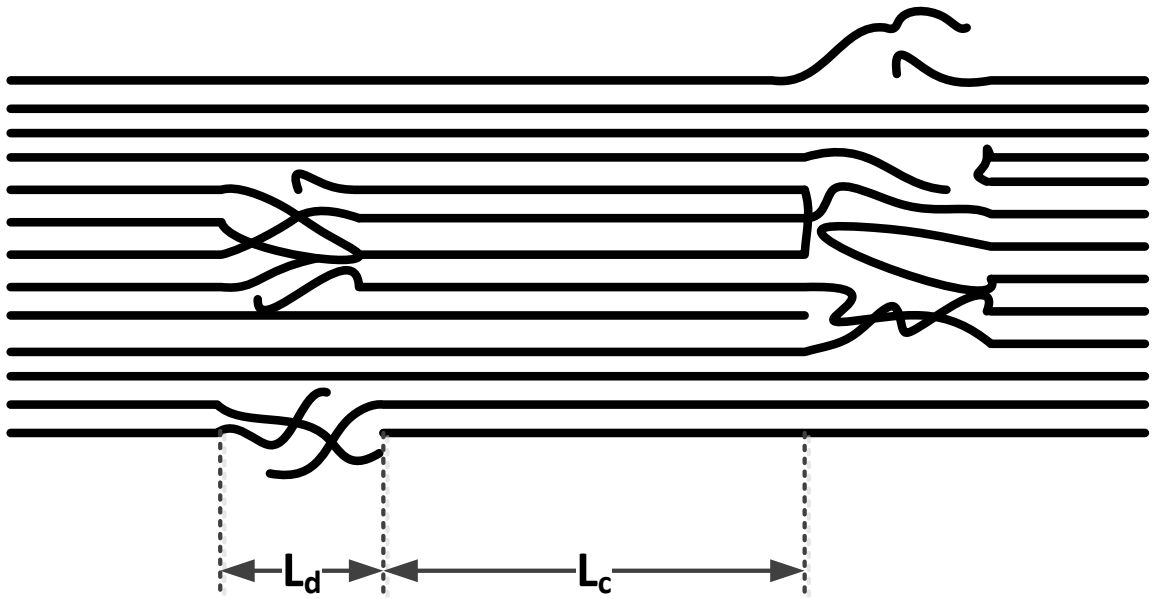


Figure 1-5 A schematic of microfibrils which contain crystalline blocks with length  $L_c$  and disordered regions with length  $L_d$ , the disordered regions are collections of tout tie molecules, chains ends and amorphous regions. The figure is modified from reference [25].

For a gel-spun hot-drawn ultrahigh molecular weight PE fiber, experiments have proved that the fibers contain macrofibrils about 500nm in diameter, and these macrofibrils

consist of microfibrils with smaller diameter around 20nm [24]. A schematic of the microfibrils can be represented by figure 1-5. The microfibrils are comprised of arrays of crystalline regions connected by the disordered sections. The disordered section as shown in figure 1-5 is a group of entangled chains or amorphous regions, chain ends, tout tie molecules (TTMs), and other defects. The TTMs are molecular chains connecting the crystalline regions and are believed to be the major load carriers for the stress transport in the disordered regions, because the amorphous regions carry negligible load. The fraction  $\beta$  of the TTM in the disordered regions and the ratio  $L_d/L_c$  of the length of the disordered region to that of the crystalline region together determine the Young's modulus of the PE fibers. The relation can be described by equation 1.1 below:

$$E = E_c \frac{1 + L_d / L_c}{1 + L_d / (\beta L_c)}, \quad (1.1)$$

where  $E$  is the true Young's modulus of a fiber,  $E_c$  is the theoretical Young's modulus of PE single crystal which is estimated about 350 GPa. As the crystallinity  $x$  of a PE fiber can be expressed by equation 1.2:

$$x = \frac{L_c}{L_d + L_c} + \beta \frac{L_d}{L_d + L_c}, \quad (1.2)$$

and rearrange equation 1.2, we have:

$$L_d / L_c = (1 - x) / (x - \beta), \quad (1.3)$$

and insert equation 1.3 to equation 1.1, we obtain:

$$E = E_c \frac{\beta}{1 + \beta - x}, \quad (1.4)$$



where both  $E$  and  $x$  can be directly measured in experiments. From equation 1.4, the TTM ratio  $\beta$  can then be calculated.

The equation 1.1 is plotted in figure 1-6. It can be clearly observed from the figure 1-6 that both the ratio  $L_d/L_c$  and the TTM fraction  $\beta$  greatly affect the measurable Young's modulus. To achieve a higher Young's modulus, fiber fabrication methods can be focused on enlarging either the length of the crystalline regions or the TTM fraction in the disordered regions, or both. However, the failure strength  $\sigma_f$  is related to the theoretical tensile strength  $\sigma_{th}$ , which is reported to be about 33 GPa [25] by:

$$\sigma_f = \beta * \sigma_{th} . \quad (1.5)$$

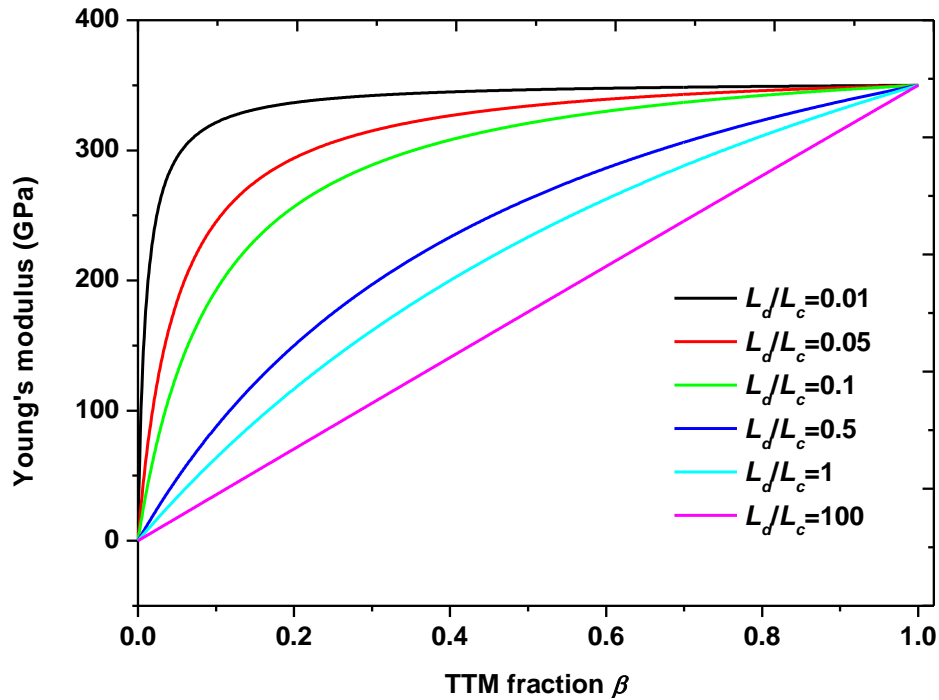


Figure 1-6 Plot Young's modulus of a PE fiber versus TTM fraction  $\beta$  in the disordered region, the figure is modified from reference [24].

And therefore the TTM fraction  $\beta$  is of more importance than the ratio  $L_d/L_c$ . This also gives us another direction for the fabrication of PE fibers, which is to align the molecular chains in the disordered regions.

### 1.2.2 Thermal transport in ultrahigh density PE fibers

The thermal conductivity of a single PE chain is predicated about 350 W/mK from molecular dynamics simulations considering the internal degrees of freedom of CH<sub>2</sub> [26]. Under at some conditions [26], the thermal conductivity of the single chain can be even divergent as the chain length goes higher. This is due to the inherently strong covalent C-C bonds within the molecular chain. Therefore we expect that a polymer fiber which consists of these aligned polymer chains possesses a much higher thermal conductivity compared with the PE semicrystalline bulk where amorphous regions and crystallites mixed together.

For an isotropic dielectric material, phonons are major energy carriers in heat transfer, and therefore the thermal conductivity  $k$  of has a general form of:

$$k = \frac{1}{3} \int_0^\infty C(\omega) (V_g(\omega))^2 \tau(\omega) d\omega, \quad (1.6)$$

where  $C$  is the heat capacity,  $V_g$  is the group velocity, and  $\tau$  is the relaxation time of phonons. They are all dependent on the angular frequencies  $\omega$  of phonon modes. For PE fibers, in the radial direction, PE chains are bonded via van der Waals force which is

much weaker than the C-C covalent bonds in the longitudinal direction. As a result, as demonstrated by previous results [27], the shear modulus is much smaller than the tensile modulus. Therefore, we expect the thermal conductivity of the highly anisotropic fiber is dominated by the longitudinal modes, for which, we rewrite equation 1.6 as:

$$k = \int_0^{\infty} C(\omega) (V_{gx}(\omega))^2 \tau(\omega) d\omega, \quad (1.7)$$

where  $V_{gx}$  is the group velocity in the longitudinal direction. Note that there is no orientation average factor 1/3 in equation 1.7 due to the anisotropic property of PE fiber. In equation 1.7, the group velocity can be estimated as [28]:

$$V_{gx} = (E_c / \rho)^{1/2}, \quad (1.8)$$

where  $E_c$  is the Young's modulus in the fiber direction,  $\rho$  is the density of PE single crystal ranging from 0.99 to 0.94 g/cm<sup>3</sup> [12]. Both the Young's modulus and density are temperature independent [28]. Consequently, the longitudinal acoustic velocity doesn't change with temperature. It is also worth to note that  $V_{gx}$  is neither dependent on frequency as both the Young's modulus and density are intrinsic material properties, thus the acoustic velocity term can be moved out of the integral in equation 1.7.

Because  $V_{gx}$  doesn't change with temperature, the temperature dependence of the thermal conductivity can be then explained by the temperature dependence of the heat capacity  $C$  and the phonon relaxation time  $\tau$ . Based on Debye model, heat capacity can be described as:

$$C = 9k_B \left( \frac{N}{V} \right) \left( \frac{T}{\theta_D} \right)^3 \int_0^{\theta_D/T} \frac{x^4 e^{-x} dx}{(e^x - 1)^2}, \quad (1.9)$$

where  $k_B$  is the Boltzmann constant,  $N/V$  is the number of atoms per unit volume,  $\theta_D$  is the Debye temperature, and  $x = \hbar \omega / k_B T$ . Equation 1.9 tells us the heat capacity increases with temperature, especially at low temperatures,  $C$  is proportional to  $T^3$ . Within the lower temperature range, the increase of the heat capacity dominates heat transport. As a result, the thermal conductivity of PE increases with the temperature. On the other hand, when the temperature keeps increasing beyond a threshold, according to the Bose-Einstein distribution, more and more phonon modes are populated. The highly populated phonons have higher chance of collisions compared with that at low temperatures, which greatly reduces the relaxation time the phonons, and this reduction effect starts to dominate the thermal transport in PE fibers. Therefore, a decreasing trend of thermal conductivity is expected to appear at a high temperature range. This has been experimentally proved by a recent study on the thermal conductivity of high-modulus polymer fibers [27].

At a high temperature range, particularly above 350K but below the melting point around 400K, the thermal conductivity is expected to sharply decrease[29]. Although at this temperature range, the crystal structure is not disrupted completely to an amorphous phase beyond the melting point, the inter chain lattice experiences enough change which allows the molecular chains undergo segment rotation which induces phonon scattering. As a result of this morphology-induced phonon scattering combined with the anharmonic

phonon-phonon scattering in the high temperature range, significant reduction of the thermal conductivity is therefore expected.

The thermal conductivity of a PE chain can be as high as 350W/mK theoretically at room temperature, which is comparable to those of some metals, for example, copper has a thermal conductivity of 398 W/mK [30]. However, the experimental values of the PE fibers are still far from this theoretical estimation, and the experimentally demonstrated thermal conductivities of PE fibers are generally below 100 W/mK [31]–[33]. The discrepancy between thermal conductivities of the single PE chain and the highly crystalline PE fiber is mainly caused by two reasons. First, the densely packed PE chains limits the transverse lattice vibrations as compared with an individual chain in the space, therefore, a resultant transverse phonon scattering greatly suppresses the thermal conductivity in the fiber direction [34]. Second, in practice, it is rather challenging to produce a PE fiber with perfectly oriented and aligned molecular chains, and entangled chains and amorphous regions always exist. These aforementioned defective regions are scattering sites for phonons, which therefore lead to a reduction of the thermal conductivity.

For non-ideal crystalline PE fibers which contain both crystalline and amorphous regions, their thermal conductivities can as well be analyzed by a thermal model similar to the TTM mechanical model used to explain the Young's modulus of the PE fibers. The model is depicted as in figure 1-7. In the fiber direction, a PE fiber can be considered as a series of sections shown in figure 1-7(a) [28], [35], [36]. The section consists of two parts in figure 1-7(b), part I contains both crystalline and amorphous regions with lengths as  $y$  and  $1-y$  respectively, and part II is fully made of crystalline PE chains. In the radial

direction, the widths of part I and part II are  $1-x$  and  $x$ . As illustrated in figure 1-7(b), a thermal circuit can be used to analyze the thermal transport in the fiber section. The total thermal conductivity  $k$  of the fiber section can be written as:

$$k = xk_I + (1-x)k_{II} = (k_I - k_{II})x + k_{II}, \quad (1.10)$$

where  $k_I$  and  $k_{II}$  are the thermal conductivities of part I and part II, respectively.

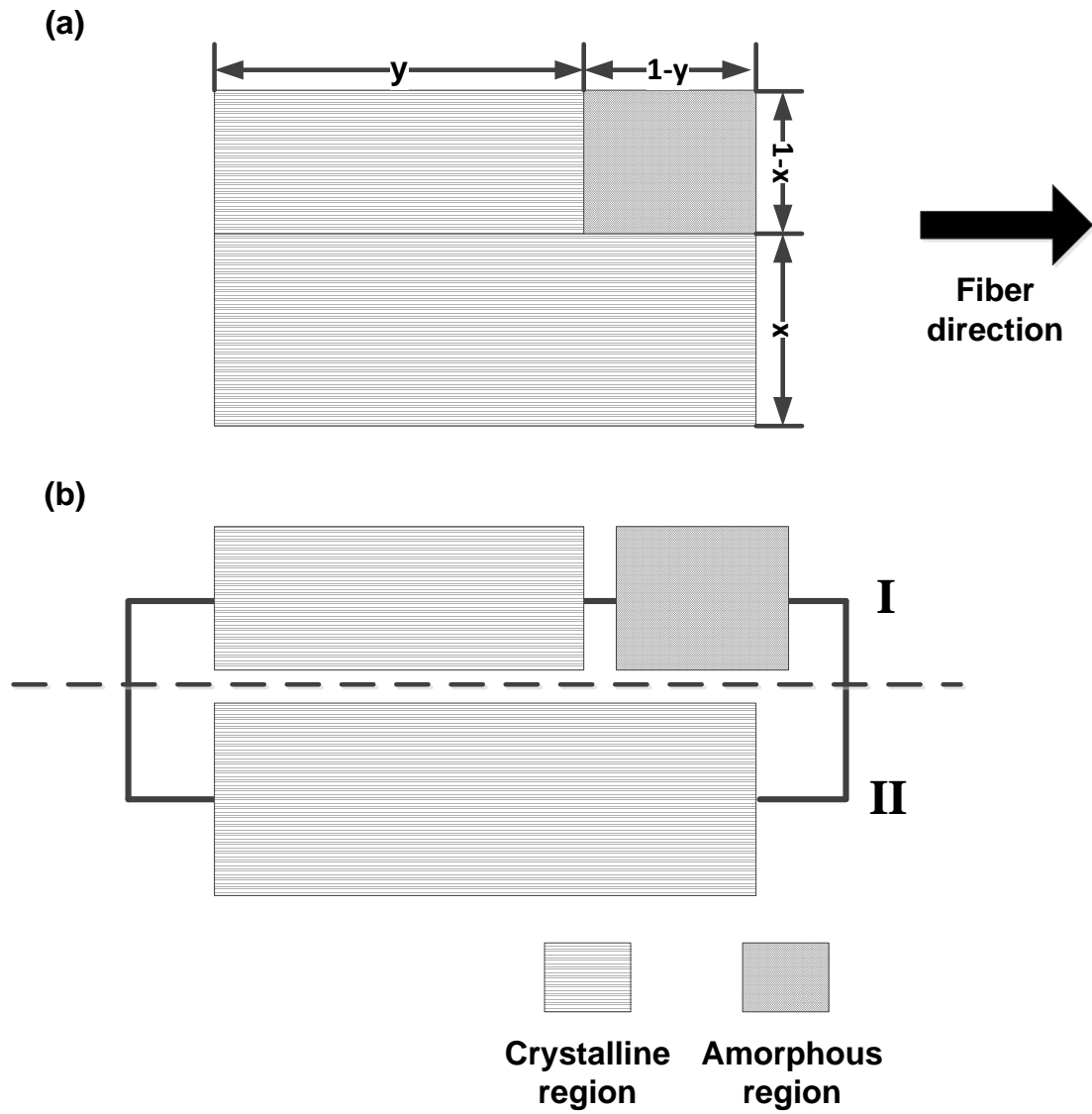


Figure 1-7 Modified from reference [32]. (a) A thermal model of a PE fiber section containing both crystalline and amorphous regions. Where,  $y$  is the length percentage of the crystalline region in part I,  $1-y$  is the length percentage of the amorphous region in part II, and  $x$ ,  $1-x$  are the width percentages of part I and part II respectively in the fiber section. (b) A thermal circuit representation of the thermal model in (a).

For a highly crystalline fiber, the molecular chains or lamellar structures are oriented with little angle deviation in the fiber direction [32]. Therefore,  $k_I$  is approximately equal to  $k_c$ , the thermal conductivity of a PE crystal in the chain direction.  $k_{II}$  is a function of both  $k_c$  and  $k_a$  which is the thermal conductivity of the amorphous region. Then  $k_I$  and  $k_{II}$  have the following forms:

$$k_I = k_c, \quad (1.11)$$

$$k_{II} = \frac{k_c k_a}{k_a y + k_c (1 - y)}, \quad (1.12)$$

Compare equation 1.11 with equation 1.12, we are able to obtain [34]:

$$\frac{k_I}{k_{II}} = 1 + \left( \frac{k_c}{k_a} - 1 \right) (1 - y). \quad (1.13)$$

As confirmed by previous research,  $k_c \gg k_a$ , therefore,  $k_I \gg k_{II}$ . Rewrite equation 1.10, we have:

$$k = k_I x + k_{II} = k_c x + k_{II}. \quad (1.14)$$

From equation 1.14, we notice that the thermal conductivity  $k$  of the PE fiber is dominated by the volume fraction  $x$  of part I. In TTM model, Young's modulus is strongly affected by the volume fraction  $\beta$  of the taut-tie molecules in the disordered region. Here, in the thermal model,  $x$  can also be regarded as the volume fraction of the crystalline region in the disordered region. Clearly, the thermal conductivity of the PE fiber has a direct correlation to the Young's modulus of the fiber [35]:

$$k / k_c = E / E_c = x . \quad (1.15)$$

### 1.3 Thermal transport in hydrogen bonded hybrid crystals

Hydrogen bonds play an important role in a large amount of materials including solids, liquids, and gases. Water, one of the most common substances on earth is a typical example of a hydrogen bonded fluid/solid. Its special properties, such as boiling point, surface tension, crystal form etc., are all closely related to hydrogen bonds. Many large biomolecules, such as DNA and proteins, also contain hydrogen bonds which are very critical for the formation of their special molecular structures. The existence of hydrogen bonds is also responsible for crystallization of some hybrid organic and inorganic crystals, for example, polysilsesquioxane (PSQ) [21]. A hydrogen bond is formed between two strongly electronegative atoms, for example, nitrogen, oxygen, and fluorine. It has a form of  $X-H \cdots Y$ , where, X and Y are highly electronegative atoms, and H is the hydrogen atom. Because hydrogen atom has one electron, it can only form one covalent bond with its neighboring atom. Due to the strong attraction of the X protons, the X-H molecule possesses a high electric dipole moment. As a result, the H proton has a strong interaction with adjacent Y atom which is also highly electronegative.



In the rank of strength of various atomic interactions, hydrogen bonds are between strong chemical bonds (ionic bonds and covalent bonds) and van der Waals' interaction. The covalent bonds have a strongest bond strength on the order of 100 kcal/mol, and the van der Waals force has a weakest bond strength about 1 kcal/mol [37]. Whereas, the strength of hydrogen bonds normally ranges from 2.4 kcal/mol to 24 kcal/mol, with some super strong hydrogen bonds even higher than 24 kcal/mol [38]. Numerous research works [39], [40] have shown the covalently bonded materials such as diamond, graphene, and carbon nanotubes, have a very high thermal conductivity, whereas materials bonded through the van der Waals force are usually treated as thermal insulators, for example, most of the amorphous polymers have thermal conductivity on the order of 0.1W/mk [31].

Therefore, the thermal conductivity of materials is dramatically affected by the type of the bonds which form the materials. Considering the strength of the different bonds, we expect the thermal conductivity of materials formed by hydrogen bonds should be higher than that of materials formed by van der Waals force but lower than that of covalently bonded materials.

It has been proved that the  $\beta$ -strand hydrogen bonding enables the thermal conductivity of the  $\beta$  sheet crystals of spider silk protein to be 1 to 2 orders of magnitude higher than other proteins [41]. Molecular dynamic simulations have shown the enhancement of the thermal conductivity in the strand direction is caused by the intermolecular hydrogen bonds between the strands. The hydrogen bonds significantly increases the stiffness of the protein crystal by suppressing the relative motion of the neighboring strands, and therefore, blue-shift and broaden the phonon modes in the low frequency regime, which consequently increases the overall thermal conductivity of the  $\beta$ -sheet crystal.

Thermal energy transport can be enhanced at silica-water interferences due to the hydrogen bonds [42]. Particularly when the silica surface is hydrophilic (hydroxyl terminated), the hydrogen bonds form between water and the hydroxyl group on the silica surface, and produce a strong coupling, which leads to enhanced thermal transport across the interface. As reported in literature [43], by introducing hydrogen bonds, thermal conductivity of amorphous polymer blends can also be increased from a range of 0.1-0.5W/mK to over 1.5W/mk in ambient conditions. In the two polymer blends (Poly(N-acryloyl piperidine) (PAP) and poly(acrylic acid) (PAA)), hydrogen bonds, which are much stronger than the van der Waals force, link the polymer backbones through low mass and short chemical groups. A continuous thermal network can be achieved when the hydrogen bonds are distributed in the polymer blends homogeneously with a concentration larger than the percolation threshold, and consequently lead to a higher thermal conductivity of polymers even in an amorphous state.

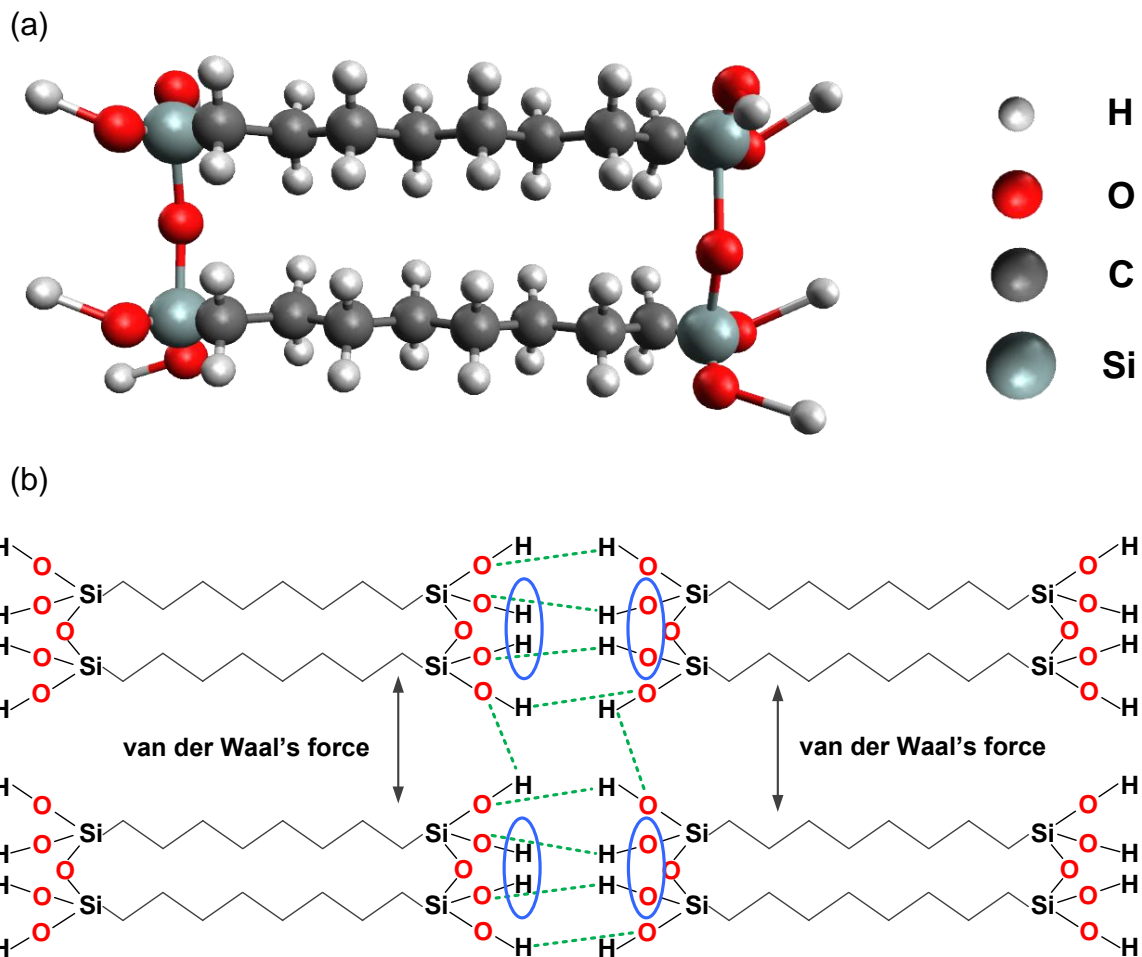


Figure 1-8 (a) A 3D graph of a PSQ bimolecular ring which is composed of 16 carbon atoms, 4 silicon atoms, and 2 oxygen atoms. (b) A 2D projection of a PSQ crystal structure formed by the van der Waals force which binds the sides of the rings and hydrogen bonds which connect the ends of the bimolecular rings. The longitudinal crystal direction is along the carbon chains. The blue circled hydrogen and oxygen are atoms that form hydrogen bonds with molecules in and out paper directions.

PSQ organic-inorganic hybrid crystals can be chemically synthesized by the sol-gel process in a large scale [21]. Due to its hybrid characteristics from the organic and inorganic moieties, it has a potential to be applied in a broad range of fields, for example

catalysts, surface modifiers and coatings [44], [45]. One unique property of the PSQ crystal is its molecular structure as shown in figure 1-8. As a result of hydrolysis and condensation of a precursor (bis(triethoxysilyl)octane (BTEO)), a 22 membered bimolecular ring structure is formed as a repeating unit which is illustrated in figure 1-8(a). Within the ring, two octylene chains are covalently linked by the two oxygen atoms. At each end of the ring, there are four hydroxyl groups which can form hydrogen bonds with the neighboring rings. With the hydrogen bonding and van der Waals force as the intermolecular interactions, the molecular crystal in figure 1-8(b) is therefore self assembled in 3D space due to one step condensation [21].

Along the carbon chain direction or the PSQ crystal longitudinal direction, the repeating units are connected by hydrogen bonds, which have bond strength between the carbon-carbon covalent bond and the van der Waals force. We expect the thermal transport in the longitudinal direction is enhanced. To the best of our knowledge, there is little experimental demonstration of the thermal transport effect of the hydrogen bonds within the organic-inorganic hybrid crystals. It will be interesting to know the alkyl chain length (number of carbon atoms in the bridging groups which connect the silanol groups as shown figure 1-8(a)) effect on the thermal transport of the PSQ crystal, because the alkyl chain length of the bridging group can be tuned by varying conditions in the sol-gel process, which can lead to a tunable thermal conductivity of the PSQ crystal if the alkyl chain length does affect the thermal transport in the hybrid crystal.

## **1.4 Motivation and scope**

The motivation for this work is to develop mechanical and thermal characterization methods, e.g. nanoinstrumentation and microelectromechanical systems (MEMS), for studying mechanical and thermal transport of crystalline polymeric materials in micro/nano scale. The experimental results will provide a fundamental basis for understanding mechanical and thermal properties of crystalline polymeric materials in micro/nano scale. Techniques for producing highly crystalline polymer fibers have been explored for the purpose of finding polymeric materials with remarkably enhanced mechanical and thermal properties. Micro/nano fabrication techniques have been applied throughout this research to manufacture micro devices for the characterization. Chapters of this dissertation are arranged in the following manner:

Chapter 2 reviews the methods for PE nanofiber fabrication and the mechanical and thermal characterization techniques for low dimensional polymeric materials. To increase the crystallinity of the PE fibers, a two-stage drawing method is developed based on gel spinning and tip drawing. With this fabrication technique, an individual fiber can be produced with a diameter in nanometer scale. To characterize the mechanical properties of such a nanofiber, various measurement schemes have been explored and the force deflection spectroscopy technique is adopted due to its accuracy, reliability, and feasibility for measurements in nanometer scale. Analysis of the corresponding mechanical model has been conducted in details. To characterize thermal properties of polymeric materials in micro/nano scale, a suspended micro device based technique is developed and examined for fibrillar materials, and a conventional  $3\omega$  method is also discussed for 2D thin film polymers. Thermal models of both techniques have been investigated as well.

Chapter 3 characterizes the mechanical properties of the PE nanofibers. Young's moduli of the nanofibers have been measured with force deflection spectroscopy (FDS) technique. The measured Young's moduli have an averaged value of  $312 \pm 108 \text{ GPa}$ , which are even higher than some metals/alloys, such as aluminum, copper, and steel. While performing the FDS technique, a nanofiber is precisely placed on a micro fabricated silicon trench with a motorized micromanipulator. After the nanofiber is fixed over the trench by gluing the two ends, an (atomic force microscopy) AFM cantilever is used to scan the fiber and deflect the middle point of the fiber section which is suspended over the trench. With a mechanical model derived from the Bernoulli beam equation, the Young's modulus can be deduced. This chapter also examines the mechanism of the PE crystallization during the nanofiber fabrication process; the crystal structure of PE is confirmed by TEM selective area diffraction pattern.

Chapter 4 introduces an organic-inorganic hybrid crystal, PSQ, which is formed by hydrogen bonding as the intermolecular force in the longitudinal direction. This chapter focuses on the thermal conductivity measurement of the PSQ crystal. In the experiment, a PSQ micro beam is placed on a micro device with suspended structures. By heating one side of the PSQ beam, a steady heat transfer creates a temperature difference across the sample. The temperature difference can be accurately determined by using the micro device. With a modified thermal model based on Fourier's law, thermal conductivities of PSQ crystals are obtained at ambient temperatures ranging from 20K to 320K, with 10K as an increment. The experimental results yield an increasing trend of PSQ thermal conductivity below 130K and a decreasing trend above. In this chapter, non-equilibrium molecular dynamics (NEMD) simulations are conducted to study the phonon behaviors

across the hydrogen bond interface. The simulation results demonstrate a great agreement with the experimental results regarding both the value and trend of the PSQ thermal conductivity.

Chapter 5 describes the thermal characterization of the PE nanofibers fabricated with the two-stage drawing method. This chapter mainly attempts to address the issues of thermal contact resistance between the PE nanofiber and the supporting surface. Cyanoacrylate based super glue is firstly tested as an intermediate material to reduce the thermal contact resistance. The measured thermal conductivities of the nanofiber reveal a crystal like trend with varying ambient temperature. Platinum deposition assisted with focus ion beam system is also utilized to tackle the contact problem, however, due to the ion beam effect. The PE fibers shift from crystalline state to amorphous, for which, the crystal like trend of thermal conductivities is not observed.

Chapter 6 finally summarizes the major contributions of the dissertation. The future work and possible challenges along with their potential solutions are also highlighted in this chapter.

## CHAPTER 2. Background and Methods

### 2.1 Polyethylene (PE) nanofiber fabrication

#### 2.1.1 Overview

As mentioned in Section 1.1.2, stress-induced polymer crystallization has been demonstrated to yield polymer fibers/films with high crystallinity on a large scale. The polymer fibers with increased crystallinity have been applied in various applications, due to their remarkably enhanced mechanical, thermal, and chemical properties [19], [25], [27], [46], [47]. Besides the ultra-drawing method as described in Section 1.1.2, other manufacture techniques, such as surface growth method [48]–[51], spinning [22], [52], [53], extrusion [54] and electrospun [55]–[59] have also been implemented to produce polymer fibers, especially PE fibers.

In the surface growth technique, PE is dissolved in suitable solvents, such as p-xylene. The solution is then filled into a Couette flow apparatus which is comprised of a cylindrical vessel and a rotating inner cylinder. At a proper crystallization temperature, for example, 103°C [49], a PE seed crystal which is grown from the p-xylene solution is pressed against the rotating cylinder. A microfiber with a diameter in the range of 5 to 40 microns continuously grows at the end of the seed crystal. While the microfiber is growing, it is wound on a variable speed take-up roll. The microfibers fabricated by this method are completely made of nanofibrils in the Shish-Kebab structure which signifies a very high crystallinity and molecular orientation in the microfibers. The surface growth technique yields a much higher fiber growth speed (31cm/min) than a free growth where the seed crystal is placed in the gap between the vessel and the inner cylinder. The



significantly increased growth rate is attributed to PE molecules adhered on the surface of the rotator, which is a phenomenon commonly observed at the liquid and solid interface. Due to the high crystallinity of the microfibers, a Young's modulus of 105GPa can be achieved [18]. However, the fiber breakage at high take-up speed inhibits a wide commercial adoption of this technique.

Whereas polymer spinning technique has long been studied and already applied in mass production of polymer fibers for commercial use. Based on the initial state of the spinning polymers, and the post processes after the spinning step, the spinning technique can be classified into melt spinning solution spinning and gel spinning. In melt spinning [60], [61], the initial polymer is heated to a temperature much higher to its melting point, for example, in PE melt spinning [61], the extrusion temperature reaches 210°C, which is 70°C higher than the melting point of PE. The molten polymer is then pumped through a spinneret capillary. A take-up spool is used to stretch and collect the extruded fibers. During the stretching process, elongation flow in the polymer melt aligns and orientates the molecules along the fiber direction. Fibers with moderate crystallinity can normally obtained by this technique. However, this technique is only limited to thermal plastic polymers and the very high extrusion temperature reduces effectiveness of the chain-extension process [62].

The terms, solution spinning and gel spinning, are sometimes interchangeable. Both of these two techniques require polymers to be dissolved in suitable solvents, the mixture then passes through a spinneret with holes, and finally fibers emerge from the spinneret holes. In both techniques, after the spinning step, substantially stretching of the fibers is followed to induce high degree crystallinity [22]. The difference between the solution

spinning and gel spinning is whether the spinning temperature is over the melting point of polymer crystals. If the spinning temperature is above the melting point, the network exists in the gel state completely disappear and the molecules in the solvents are in random coil state, the corresponding procedure is normally regarded as solution spinning, and vice versa.

A typical example of gel spinning is the ultra-high molecular weight PE fiber [63], [64], which is challenging for melt-spinning, because the extremely long and entangled PE chains in the melt hinder the full extension of PE molecules. In the PE gel spinning, PE is first dissolved in an appropriate solvent at a temperature above the PE crystal melting point ( $>140^{\circ}\text{C}$ ). After cooling the mixture to room temperature, the solution turns into a gel state. The gel is then extruded through a spinneret to form a gel fiber at a temperature below the melting point. The gel fiber further subjects to solvent removal and a hot drawing step at a temperature around the melting point. The fibers obtained from the gel spinning technique are proved very strong with a tensile strength of 3.5GPa [25], [64].

While the conventional spinning techniques started from 1970s [22], [53], [62], electrospinning gained substantial research interest in the 1990s [58], with the advent of nanotechnology. Using the electrospinning technique, polymer fibers can be easily scaled down to nanoscale which is very challenging for the conventional spinning techniques. There are many unique properties for nanoscale polymer fibers, for example, a remarkably high surface area greatly enhances the catalysis performance [65], and the nanoscale size is highly beneficial for filtration membranes, tissue engineering scaffolds etc [66]. As a result of great academic and commercial interests, there are many review articles on the electrospinning technique [65]–[67]. In general, an electrospinning system

has three components, a vessel with a fine capillary needle attached, a collecting apparatus often made of metals which also serve as a counter electrode, and a high voltage power supply. During the electrospinning process, the vessel is filled with polymer solution, a high electric field (100-500kV/m [58]) is applied between the vessel needle and the counter electrode. As a result, a Taylor cone is formed at the end of the needle. Beyond a voltage threshold, an electric force outbalances the surface tension of the polymer solution; a jet is formed within the electric field. Due to the instability and high speed of the jet, the polymer fiber can be stretched and shrunk to nanoscale. With the electrode spinning method, a large variety of polymer fibers have been produced, for example, Nylon-6,6 [68], polyacrylonitrile (PAN) [56], polymethyl methacrylate (PMMA) [69], titanium oxide (TiO<sub>2</sub>) [70], PE [59], [71] etc.

### **2.1.2 Two-stage drawing method**

As mentioned above, the conventional spinning method can only produce polymer fibers in micro meter scale. Although the electrospinning method has succeeded in mass fabrication of the polymer nanofibers, the crystallinity is not as high as fibers obtained by the conventional spinning method [59], probably due to the lack of a post hot drawing step. With the goal of characterizing an individual PE nanofiber with high crystallinity, we adopt a two-stage tip drawing method. As illustrated in figure 2-1, our method is a combination of gel spinning and tip drawing. To fabricate a PE nanofiber, we first dissolve PE powder (ultrahigh molecular weight PE; dimensionless relative molecular mass of  $3-6 \times 10^6$ ; Alfa Aesar) in Decalin at 140°C to prepare a PE gel. The dilute solution has a concentration of 0.8 wt%. The dissolving process is conducted inside a glove box filled with argon gas to avoid molecular degradation. During the dissolving process, the

mixture should be continuously stirred to prevent local over heat, and enhance the uniformity of the solution. Particular care should also be taken to avoid bubble generation during the stirring process.

After the white PE powder is completely dissolved, the mixture becomes a transparent viscous fluid and the beaker containing the liquid is immediately put into a cold water bath. This quick water quenching step can suppress the formation of large lamellar crystals, which can prolong the time needed for further remelting of PE. Because a large super cooling temperature, around 95°C below the equilibrium melting temperature, significantly decreases the thickness of the lamella at meta-stable state [72]. After about 30 minutes when the liquid is cooled down to room temperature, the translucent PE gel is made. The translucent color is due to the mixture of the randomly coiled PE chains and the uniformly dispersed lamella in the solution.

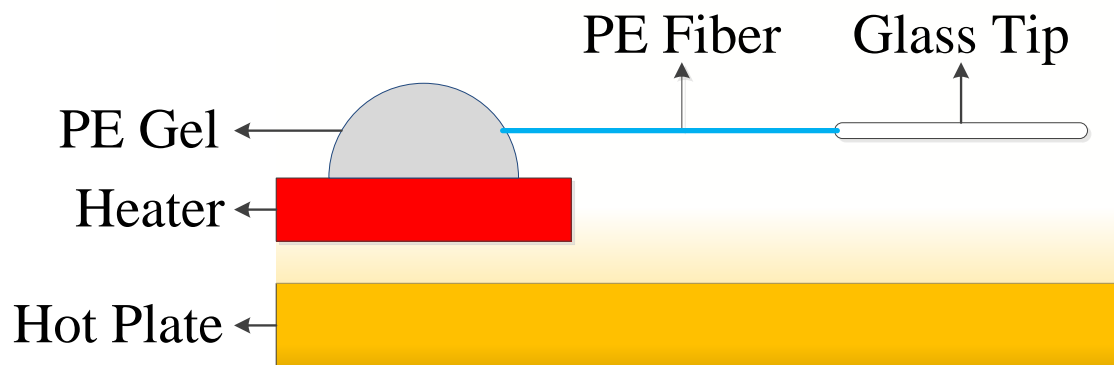


Figure 2-1 Schematic of a nanofiber fabrication setup. The heater represented by the red block heats the PE gel to a temperature of 120°C which is beyond the melting temperature of PE crystals. The hot plate heats the surrounding air to 90~100°C which expedites the solvent evaporation during the drawing process.

Following the PE gel preparation, a two-stage heating process is implemented to produce highly-crystalline PE nanofibers [31]. A hot plate is used to uniformly heat the air above at 90~100°C. A 5 mm by 5 mm silicon chip is suspended about 1 cm over the hot plate. A small heater is attached to the back of the chip. The heater and the chip together form a PE gel holder whose temperature can be adjusted to melt the gel in a controllable period of time. The gel is heated at 120°C on the silicon chip for a few seconds until the translucent gel turns into a clear liquid. A glass tip fixed to a micromanipulator is then used to horizontally pull a microfiber with a length of hundreds of microns. The microfiber suspended over the hot plate is heated by the hot air. The microfiber is then slowly drawn so that its size is scaled down to nanometer level, and during this drawing process, the fiber is subject to the second stage heating. The entire drawing process is conducted under a dark-field stereo microscope and takes 1~2 minutes.

With the two-stage drawing method, we are able to obtain individual PE nanofibers with very high crystallinity. Unlike the conventional gel spinning method where the PE solution passes through the spinneret holes which causes transverse flow. In the two-stage drawing process, the fibers are free in space without any effect from the solid walls, therefore the drawn solution experiences almost pure elongation flow which creates uniform acceleration along the drawing direction [52]. Especially when the shear rate is

beyond a threshold [73], polymer chain extension undertakes a sharp coil-stretch transition. Upon solvent evaporation and PE solidification, the extended and aligned chain structure sustains in the fabricated fibers, which consequently ensures an extraordinary high crystallinity.

## **2.2 Mechanical property characterization for one dimensional materials**

### **2.2.1 Probing mechanical properties of materials in nano meter scale**

With the development of nanotechnology, a variety of one dimensional materials have been produced and extensively studied, for example, metal nanorods, carbon nanotubes and polymer nanofibers [74]. Due to a decrease in the number of defects per unit length compared with the bulk, one dimensional material is predicted to possess enhanced mechanical properties. However, the conventional bending and pulling tests are hard to be implemented for mechanical study of the nanosize materials [75]. Therefore, it is of great interest for researchers to develop tools and techniques to characterize the mechanical properties of these one dimensional materials in nano meter scale.

Natural resonance vibration method has been successfully used to measure the Young's modulus of carbon nanotubes [76] and carbon nanofibers [56]. The method is based on resonant excitation of nanofibrils in situ in a transmission electron microscope (TEM) or scanning electron microscope (SEM). In the method, the nanofibril is attached to a thin tip, for instance, an atomic force microscopy (AFM) cantilever tip or an ultrafine metal wire. A piezoactuator drives the whole assemble to vibrate. By scanning the driving frequency applied on the nanofibril, we are able to find its first harmonic (the

fundamental frequency) where the amplitude of the vibration reaches maximum. The first harmonic has a direct relationship with the Young's modulus of the nanofibril as shown in equation 2.1:

$$f_0 = \frac{\beta_0^2}{2\pi} \frac{d}{L^2} \sqrt{\frac{E}{16\rho}}, \quad (2.1)$$

where  $f_0$  is the fundamental frequency of the nanofibril,  $\beta_0$  is a coefficient for the fundamental mode of vibration,  $d$ ,  $L$ ,  $\rho$ , and  $E$  are respectively, the diameter, length, density and Young's modulus of the nanofibril. From equation 2.1, we can calculate the Young's modulus. However, polymer nanofibers are hard to be characterized with this method, because the very long electron exposure time can induce large irreversible morphological damage.

Nanoindentation is also reported [77]–[79] as a feasible method to study the mechanical properties of nanomaterials. In the method, a nanoindenter tip is brought to contact with and indent the measured material. A loading and unloading displacement curve is then obtained during the indentation process. The force gradient  $S$  of the initial part of the unloading curve has a correlation with an effective modulus  $E_r$  [77]:

$$S = 2\beta \sqrt{\frac{A}{\pi} E_r}, \quad (2.2)$$

where  $\beta$  is a geometric factor of the indenter, and  $E_r$  is affected by both the modulus of the indenter  $E_i$  and the modulus of the measured sample  $E$ :

$$\frac{1}{E_r} = \frac{1 - \nu^2}{E} + \frac{1 - \nu_i^2}{E_i}, \quad (2.3)$$

where  $\nu_s$  and  $\nu_i$  are Poisson's ratio of the sample and the indenter. It is important to know that equation 2.2 works with the condition that the deformation during the indentation is purely elastic [77], [80]. It is still an open question that whether the equation is still applied in nanoscale [80]. Especially for polymer nanofibers, the Young's modulus is highly anisotropic, it is not proper to implement the nanoindentation method for polymer nanofiber characterization.

Besides the two methods mentioned above, bending tests assisted with an AFM have also been extensively explored for mechanical property characterization of nanomaterials. Among all bending tests, there are mainly two categories, the lateral force bending test [74], [81], which deflects the nanofilaments in a direction perpendicular to the AFM tip, and the vertical force bending test [80], [82]–[84] in which the deflection of the samples is along the AFM tip direction. The later is also referred to as force deflection spectroscopy technique or three point bending technique. In the following part of this dissertation, we call the technique as force deflection spectroscopy to avoid confusion. The two type bending tests are all based on Bernoulli's beam equations and rely on the high special resolution of the AFM. Although both techniques have been used to successfully extract the mechanical properties of nanofilaments, the lateral force bending technique suffers tricky calibration of the torsional mode of the AFM cantilever [80], which makes the force deflection spectroscopy (FDS) technique surpass the former technique, and for the same reason, we use the FDS technique for our polymer nanofiber characterization.

### **2.2.2 Force deflection spectroscopy**



Even though the FDS technique outperforms other techniques due to a number of advantages mentioned in the section above, it involves the fabrication of a substrate with micro trenches and a few tedious sample preparation steps which are usually time consuming. Generally there are three major tasks before the FDS measurement: 1. Design and fabricate silicon chips with micro trenches of dimensions suitable for the mechanical properties of nanomaterials to be measured. The trenches are usually fabricated by photolithography and reactive ion etching on a silicon wafer. 2. Place the samples on the silicon chip and firmly clamp the samples on the trench. 3. Scan the sample assembly made in the second step using an AFM to select the samples with good clamping condition on the trench. These sample preparation steps are further stated with details in the following sections.

#### **2.2.2.1 Silicon trench fabrication**

We fabricated the silicon trenches/holes with the conventional photolithography. The entire fabrication process is illustrated in figure 2-2. The process starts with a 4" intrinsic silicon wafer. On the silicon wafer, we first spin a layer of AZ 4110 photoresist at 4000 rpm. The resulting film thickness is about 1.1  $\mu\text{m}$ . The coated wafer is baked at 90°C on a hot plate to remove moisture and slightly harden the photoresist. After the soft bake step, the silicon wafer with photoresist is exposed to ultra violet (UV) (wavelength of 320nm at 5mW/cm<sup>2</sup>) in a contact aligner (Karl Süss MA6) for 60 seconds. Following the exposure step, we immerse the silicon wafer in a developer (AK 400K: DI water, 1:4) for 75 seconds. Gentle agitation is applied to ensure a uniform development. After the development, the wafer is subject to deionized (DI) water rinsing and N<sub>2</sub> blow drying.

To fabricate micro size trenches/holes with vertical sidewalls, we choose deep reactive ion etching (DRIE) for an anisotropic etching to avoid undercut which normally happens in wet etching. A STS Multiplex ICP RIE system is used for the DRIE. During the dry etching process, the wafer is placed in a vacuum chamber (100mTorr) filled with reactive gases  $O_2$  and  $CF_4$  with flow rates of 3.1 sccm and 25 sccm, respectively. RF power of 100W is applied to induce Ar gas plasma for enhancing the Si etching rate. With this particular recipe, the etching rate is about 0.15 microns/min. For 500nm deep trenches/holes, the dry etch step takes about 4 minutes. The final step after the dry etching is to remove the photoresist residual in AZ 400T stripper at 50°C for 2 minutes. The cleaned wafer is then cut into dies (5mm  $\times$  5mm) by a dicing saw.

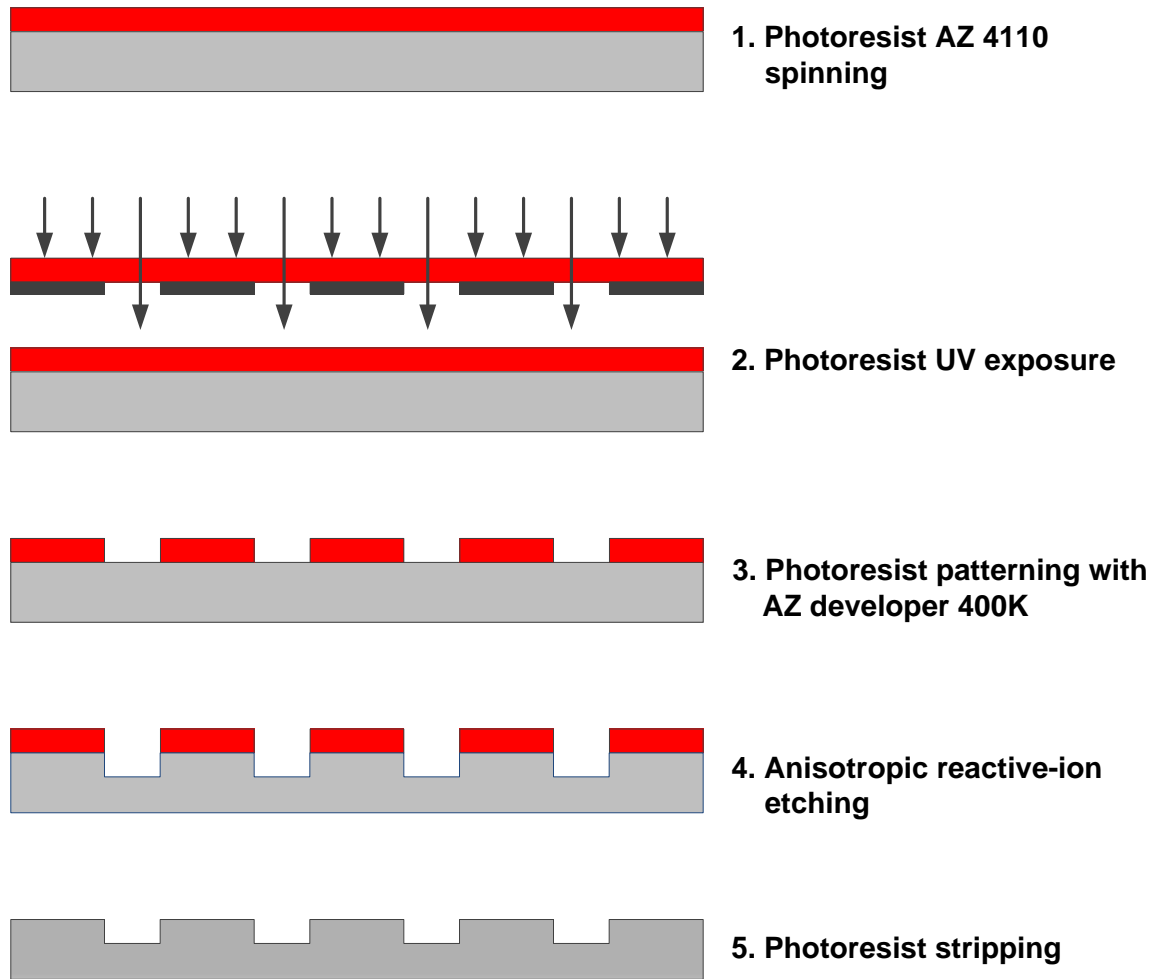


Figure 2-2 Silicon trenches fabricated with conventional photolithography and inductively coupled plasma RIE etching.

#### 2.2.2.2 Sample preparation for FDS measurements

After the two-stage drawing process, a PE nanofiber sways over the hot plate. The diced silicon chip with micro-fabricated trenches is lifted to touch the PE nanofiber. Under a stereomicroscope, we apply a drop of epoxy on the PE nanofiber at each edge of the silicon chip in order to fix it on the substrate. The epoxy usually takes about 20 minutes to cure at room temperature. The silicon chip with the PE nanofiber is then removed from

the setup after the fully cure of the epoxy. The cured epoxy has enough gripping strength to hold the nanofiber on the silicon chip, which enables us to pull and break the PE nanofiber between the drawing tip and the small heater where the PE gel is placed.

The silicon chip is then positioned under a high magnification microscope (Nikon, Eclipse LV 100 DA-U). A high resolution motorized micromanipulator (MPC-200-ROE, Sutter Instrument Company), with minimal micro step size as small as 62.5 nanometers, is used to drive a rigid copper arm on which a tungsten tip is mounted. The tungsten tip is adopted for adhesive transfer and precisely clamping the PE nanofiber over silicon trenches with width ranging from 5  $\mu\text{m}$  to 10 $\mu\text{m}$ . It is worth to note that there are two reasons for us to choose the tungsten tips: First, the surface tension of tungsten is much larger than the cyanoacrylate based super glue used for clamping. Second, the tungsten tip with an end diameter about 1 $\mu\text{m}$  is rigid enough to manipulate the nanofibers and push them against the substrates. Figure 2-2 shows a successfully clamped PE nanofiber on the silicon substrate. The circled sections are where the PE nanofiber is freely suspended with both ends fixed over the trenches, which satisfies the model of structural beam deflection with both ends fixed.

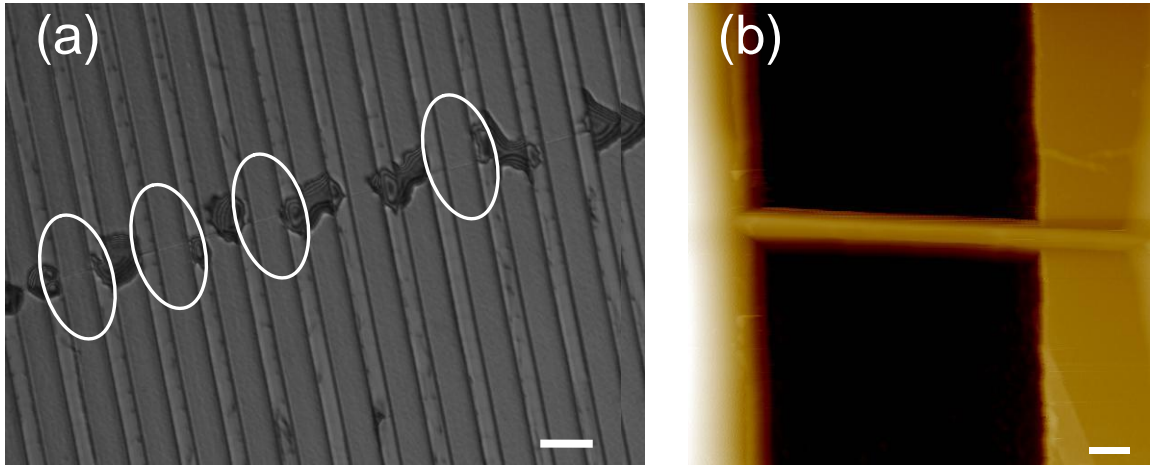


Figure 2-3 (a) An optical graph of a PE nanofiber clamped by adhesives and separated to sections marked by white circles where the nanofiber is suspended over the micro-fabricated silicon trench, the scale bar is 10 $\mu$ m. (b) An AFM image of the PE nanofiber in (a), the relatively white part in the image represents a little portion of the adhesives, the scale bar is 1  $\mu$ m.

Because of the low surface energy of the super glue compared with silicon, super glue tends to freely spread and wet an arbitrarily large area on the silicon substrate; therefore, careful manipulation of the glue with a controlled covering area is critical for a successful clamping. We first place a thin layer of glue around the testing area where there are no trenches and then push the tungsten tip against the edge of the glue film where the glue layer is thinner compared with the center area. With this step, we can avoid a large amount of glue attaching the tungsten tip, and the thin layer of glue allows us to conduct a precisely gluing over a small area about a few square micrometers. The tip which is covered by an appropriate amount of glue is then moved and aligned with the trenches. By dropping the tip to the substrate using the micromanipulator, a downward force is

applied to deflect the tip slightly for pinning down the PE nanofiber. It is found that the glue usually stops flowing when it arrives at the edges of the trenches due to the edge effect in wetting [85]. This edge phenomenon is particularly helpful for our research; because of which, we can have the PE nanofiber exactly pinned at the edges without the trenches partially filled with glue which would potentially limit the natural deflection of the nanofiber under bending tests.

### **2.2.2.3 FDS measurement scheme and its analytical model**

The FDS measurements are based on force deflection (FD) curves (also called force distance curves). The FD curve has been widely employed to study the surface properties of diverse materials by exploring the surface interactions [86]. With proper cantilevers and the high resolution of AFM, the FD curve can display surface force interactions down to piconewtons [87].

A typical FD curve obtained on a bar silicon substrate is illustrated in figure 1-4(b) with x-axis as the height of the cantilever and y-axis as the force on the cantilever. The FD curve has two components, the approaching curve and the retracting curve. While the cantilever approaches the substrate, the distance between the cantilever tip and the sample surface is too large for any interactions, the cantilever remains its original state with zero deflection which is represented by the initial portion of the approaching curve. With the tip very close to the surface, attractive forces, such as van der Waals force, capillary force, electrostatic force etc., causes jump to contact which can be observed as a small dip on the approaching curve.

When the tip and sample are in contact, the height of the cantilever base keeps decreasing. A repulsive force depending on the surface chemistry and physics deflects the cantilever. The repulsive force stays until the cantilever is retracted from the sample surface. It is this portion when the tip stays in contact with the sample surface gives a large amount of information about the sample properties, such as hardness, elastic/plastic deformation etc. For figure 2-4(b), the approaching and retracting portions of the FD curve at full tip-sample contact completely overlaps, demonstrating that there is only elastic deformation which is mainly attributed to the deflection of the cantilever itself. A larger dip can normally be observed in the retracting curve when the cantilever is lifted off from the surface, this is primarily due to two factors, the force deflection curve hysteresis caused by a low spring constant of the cantilever and adhesion forces as a result of the surface chemistry or external substances like water vapor [86].

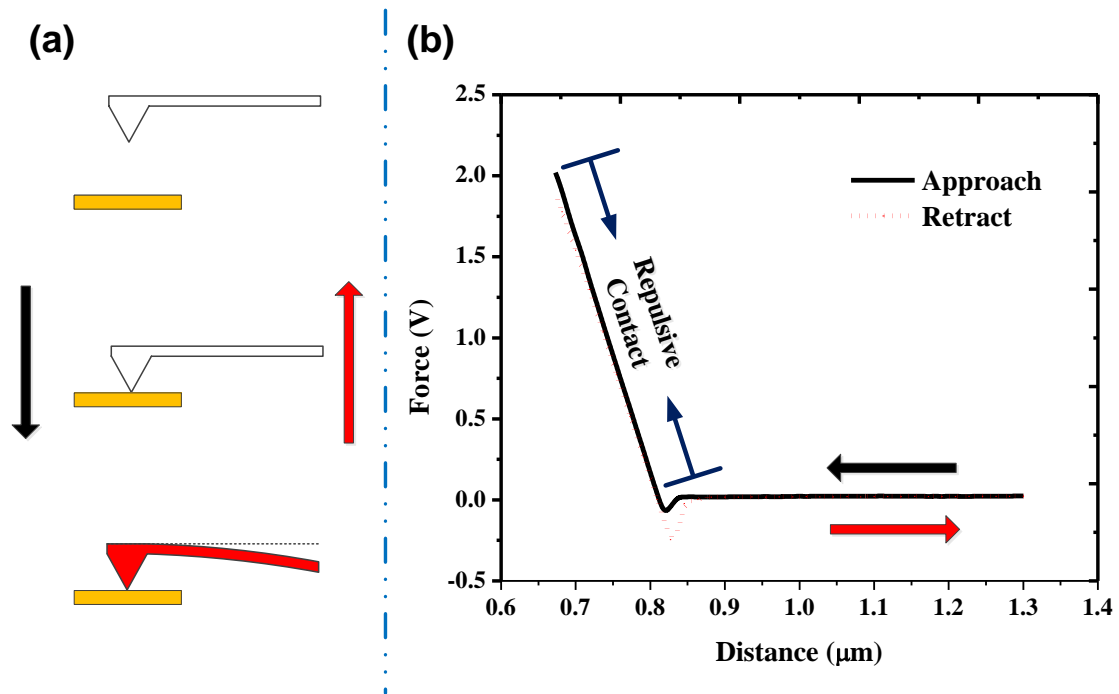


Figure 2-4 A FD curve obtained on a bare silicon substrate. (a) A cartoon of an AFM cantilever approaching (black arrow) to and retracting (red arrow) from the substrate. (b) A FD curve corresponding to the movement of the cantilever described in (a), with the black curve for approaching and the red curve for retracting.

The first step of a FDS measurement is to image the nanofibers using AFM contact mode. Through the images, the middle point of the nanofibers over the trench can be precisely located, and this point is where the AFM cantilever tip applies a force. The force applied causes a deflection of the nanofibers. With the AFM system, a FD curve can be obtained by recording the corresponding deflections while gradually increasing the concentrated force. The FD curve on the nanofibers is a combination of deflections from both the nanofibers and the AFM cantilever. In order to find the sole deflection of the PE nanofiber, FDS measurement is required to be performed on a bare silicon surface to get a FD curve for the silicon substrate.

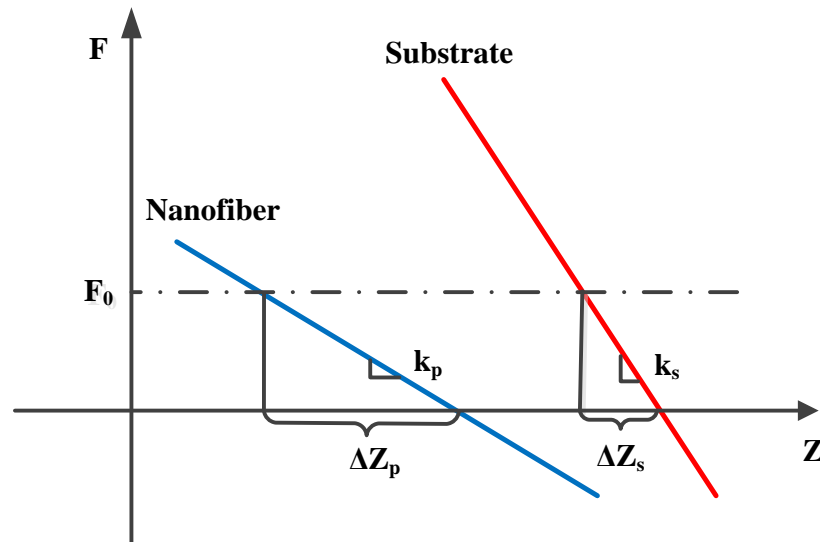




Figure 2-5 FD curves of PE nanofiber and rigid silicon substrate.  $F$  is the concentrated load applied at the midpoint of the suspended PE fiber or solely on the silicon substrate.  $Z$  is the height of the AFM cantilever base. The blue curve represents a total deflection from the AFM cantilever itself and the PE nanofiber. The red curve is the calibration curve which only includes the deflection of the AFM cantilever when it contacts the rigid silicon surface.

Two schematic FD curves, one for a nanofiber and the other one for a silicon substrate, are shown in figure 2-3, where only the linear portions are presented. When the AFM tip is brought to contact with the rigid silicon substrate, only the AFM cantilever bends, and hence with the same applied force  $F_0$ , the deflection  $\Delta Z_s$  corresponding to the cantilever bending is smaller than the combined deflection  $\Delta Z_p$ . The difference between  $\Delta Z_p$  and  $\Delta Z_s$  is the midpoint downward deflection  $\delta$  of the nanofiber. By analyzing figure 2-3, we can express  $\delta$  by the slopes of these two FD curves:

$$\delta = \Delta Z_p - \Delta Z_s = \frac{F_0}{k_p} - \frac{F_0}{k_s} = F_0 \left( \frac{k_s - k_p}{k_s k_p} \right). \quad (2.4)$$

When a homogeneous beam is fixed at both ends and a concentrated load is applied at the center of the beam, the expected maximum deflection at the center is given by the following formula:

$$\delta = \frac{FL^3}{192EI}, \quad (2.5)$$

which is a solution of the Euler-Bernoulli beam equation provided that the longitudinal length of the beam's neutral plane doesn't change during the bending, where  $F$  is the concentrated central load,  $L$  is the length of the original beam, and  $I$  is the moment inertia of plane area associated with the beam. Since  $F_0$  in formula (1) is any load within the corresponding deflection range, we can replace  $F_0$  with  $F$ . Equating formula 2.4 with formula 2.5,

$$\frac{\delta}{F} = \frac{k_s - k_p}{k_s k_p} = \frac{L^3}{192 EI}, \quad (2.6)$$

and substituting the moment of inertia for a circular cross section,  $I=(\pi d^4)/64$ , into formula 2.5, we have the Young's modulus described as:

$$E = \frac{k_s k_p}{k_s - k_p} \frac{L^3}{192 I} = \frac{k_s k_p}{k_s - k_p} \frac{L^3}{3\pi d^4}, \quad (2.7)$$

where  $d$  is the diameter of the cylindrical beam or the diameter of the nanofiber in our case.

Even though FDS can be readily used to measure the Young's modulus of various nanofibrillar materials, three critical points should be carefully examined. First, the spring constant of each AFM cantilever should be calibrated using the *in situ* thermal noise method[88] before each measurement. The spring constants should be carefully chosen to fit the measurement of different materials. If a cantilever is very stiff, the deflection of the cantilever is not noticeable compared with the deflection of the sample, whereas for an extremely soft cantilever, the deflection of the sample is not significant. Both extreme cases can induce large uncertainties in the final calculations of the Young's modulus;

therefore, the AFM cantilevers used for measurements should be carefully selected based on their spring constants. As an example, in our PE nanofiber measurements, we choose AFM cantilevers with spring constants ranging from 2.5N/m to 3N/m, these cantilevers can significantly increase the accuracy of the measurements. Second, a closed-loop piezoelectric z scanner should be used in the measurement, in order to reduce the system hysteresis. Third, considering the validity of Euler-Bernoulli beam equation, the vertical deflections of the nanofibers ought to be limited within the range about the diameters of the tested nanofibers.

### **2.3 Thermal transport characterization for one dimensional polymeric materials**

Thermal transport in low dimensional materials has been intensively studied as a result of the rapid progress in the synthesis and production of these materials with micro/nano scale dimensions. Numerous techniques have been developed to accurately probe the thermal properties. For example,  $3\omega$  method developed in 1990s [89] has been widely used to explore thermal transport in organic and inorganic materials [90]–[92]. However, this method normally needs to fabricate a thermal device on a smooth and flat surface, which makes it impossible for thermal characterization of organic filaments in micro/nano meter scale. Time domain thermal reflectance (TDTR) and frequency domain thermal reflectance (FDTR) eliminate the direct device fabrication on the sample surface; both techniques have been applied for thermal property measurements of sub-micron thin films [93]–[96]. Nevertheless, the pump and probe lasers equipped in the systems have

spot diameters of several micrometers or even larger [94], [95], [97] which are much bigger than the diameter of a polymer nanofiber.

Recently, a method based on bi-material AFM cantilever was used to measure the thermal property of individual PE nanofibers at room temperature, and yielded a thermal conductivity of  $\sim 104 \text{ W/mK}$  for a highly crystalline PE nanofiber [31]. Unfortunately, a particular problem associated with this method is the low signal to noise ratio which imposes a high level of uncertainty on the measured thermal conductivities. Furthermore, the bi-material cantilever method is hard to characterize the thermal properties over a large temperature range, for example, from 10K to 320K, within which the thermal properties can be very interesting and important.

To accommodate the thermal characterization of PE nanofibers fabricated by the two-stage drawing method, we decide to incorporate a micro device with suspended structures in our thermal study of the nanofibers. With the micro device, we can directly measure the thermal conductivities of the nanofilaments by applying a simple steady state heat transfer model [6], [40], [98].

### **2.3.1 Micro devices with suspended structures**

Figure 1-6 shows a typical micro device with two suspended islands. The detailed fabrication process is well documented in previous literature [6], [99]. Briefly, we fabricate the device using a standard wafer-scale micro-fabrication process. The process starts with coating a silicon wafer with  $0.5 \mu\text{m}$  thick silicon nitride with chemical vapor deposition (CVD) first and a second layer of platinum (Pt) with thickness of 30 nm by sputtering deposition. The Pt layer is then patterned to electrically conducting legs and

serpentine coils with photolithography and ion milling. With the SiN<sub>x</sub> layer exposed, another photolithography step together with RIE is conducted to remove the area without Pt structure. A final Si etching step with tetramethylammonium hydroxide (TMAH) or potassium hydroxide (KOH) is performed to release the thermal device. The final width of the conducting legs is about 2 μm, and the line width of the serpentine coil part is around 1.3 μm.

As shown in figure 2-6, a SiO<sub>2</sub> nanowire is placed between the two suspended islands. One of the islands has a DC current passing through for heating one side of the SiO<sub>2</sub> nanowire. Once the heat transfer reaches steady state, a constant temperature difference is built between the two islands. The resistances of the two islands increase with temperature due to a higher possibility of electron collisions. Therefore, the temperatures of the islands can be deduced by measuring the resistance change with a high resolution lock-in amplifier which is described in details in the following section.

There are two common challenges of preparing a thermal device with samples incorporated. The first challenge is how to place the nanowire exactly at the gap between the two islands. It depends on the samples to be measured. For samples which can be individually dispersed in a solution, we can directly cast a drop of the solution on the device, and by chance, out of a number of devices, there are usually some devices with samples just bridging the gap. For samples which can be grown with catalysts, we can simply use the devices as substrates and directly grow the samples between the gaps, for example, carbon nanotubes. For samples that must be picked individually, we should use a micromanipulator to precisely pick the sample and place the sample across the gap. The second challenge is the thermal contact between the nanowire and the islands. For

inorganic materials, for example, nanowires made of  $\text{SiO}_2$  and Si, FIB assisted Pt deposition can usually make good thermal contacts with a resolution of several nanometers. For organic materials with low thermal conductivities, we either simply put the sample on the devices without any bonds or a layer of organic adhesives, because the intrinsic thermal resistance of the sample itself is much higher compared with the contact thermal resistances even with the samples adhering the islands only by the effect of van der Waals force.

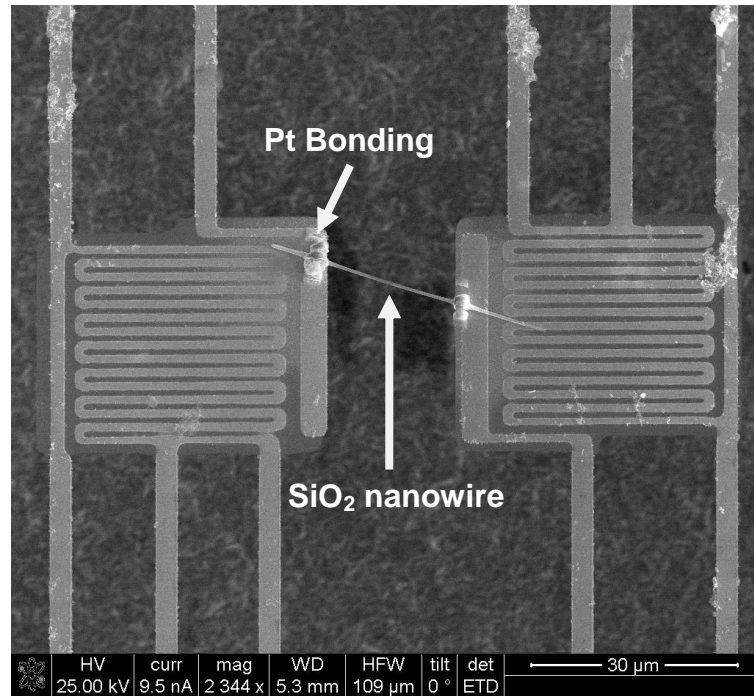


Figure 2-6 An SEM image of a micro device with two suspended islands. The two islands are identical with Pt coils and legs fabricated on the top surface and a bottom  $\text{SiN}_x$  layer as the supporting substrate.

### 2.3.2 Electrical configuration and thermal model

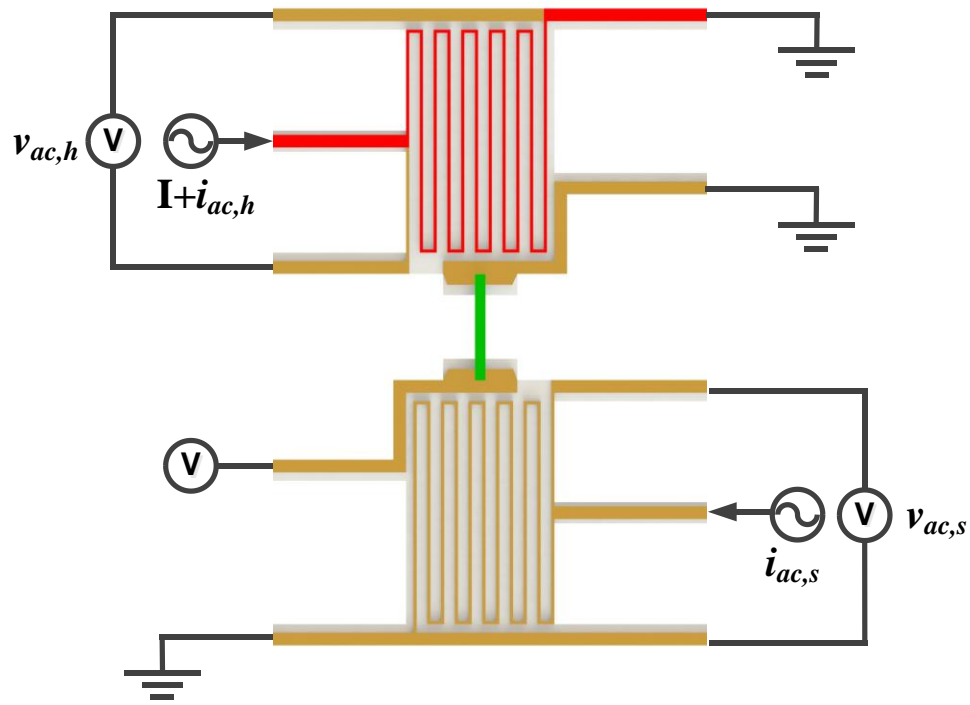


Figure 2-7 Electrical connections of the thermal device for thermal conductivity measurement. The red colored line represents a DC current path which heats the SiNx substrate due to the Joule heating effect. The blue colored line stands for samples to be measured.

As shown in figure 2-7, for each island, there is an alternating current (AC) ( $i_{ac,h}$  and  $i_{ac,s}$ ) flowing through the Pt coil, the AC is supplied by an internal oscillator from a lock-in amplifier. The frequencies of ACs are 1.11kHz and 150Hz respectively for the heating island and the sensing island. The particular frequencies are chosen so that other possible noises, for example, the power-line frequency and its harmonics, can't interfere with signals to be measured. To avoid unexpected temperature rise of both islands caused by the AC, the current is therefore controlled to be within several nanoamperes, for example, 50nA used in our measurements. This is achieved by serially connecting a 100M $\Omega$

precision resistor in the electrical circuits. Using the four terminal sensing method, the resulted first harmonic component of AC voltage drop ( $v_{ac,h}$  and  $v_{ac,s}$ ) across the Pt coil is measured with the lock-in amplifier. Consequently, the accurate resistances of both Pt coils can be deduced from the ratio of measured AC voltage and supplied AC. The electrical resistances of Pt coils on the heating and sensing islands are normally from 1.3K to 5K at room temperature. And the electrical resistances change linearly with temperature, for which, we can detect temperatures of the islands by measuring their electrical resistances of the Pt coils.

In order to produce a temperature difference between the two islands, as show in figure 2-7, a DC ( $I$ ) is applied to the Pt coil on the heating island by a source meter (Keithley 2400). In a typical measurement, the source meter sweeps a DC from 0  $\mu$ A to a maximum current which doesn't produce a temperature difference over 3K between the two islands. For our thermal devices with a PE fiber on, the maximum current above is usually less than 15  $\mu$ A. When the DC flows through the Pt coil, a certain amount of Joule heat regarded as uniformly distributed volumetric heat raises the temperature of the Pt coil. Because the small thickness of SiNx is about 300nm, the heat capacity of the islands is very small, leading to a thermal time constant of the suspended islands on the order of 10ms, so that we assume the temperature the Pt coils is the same as the supporting SiNx islands.



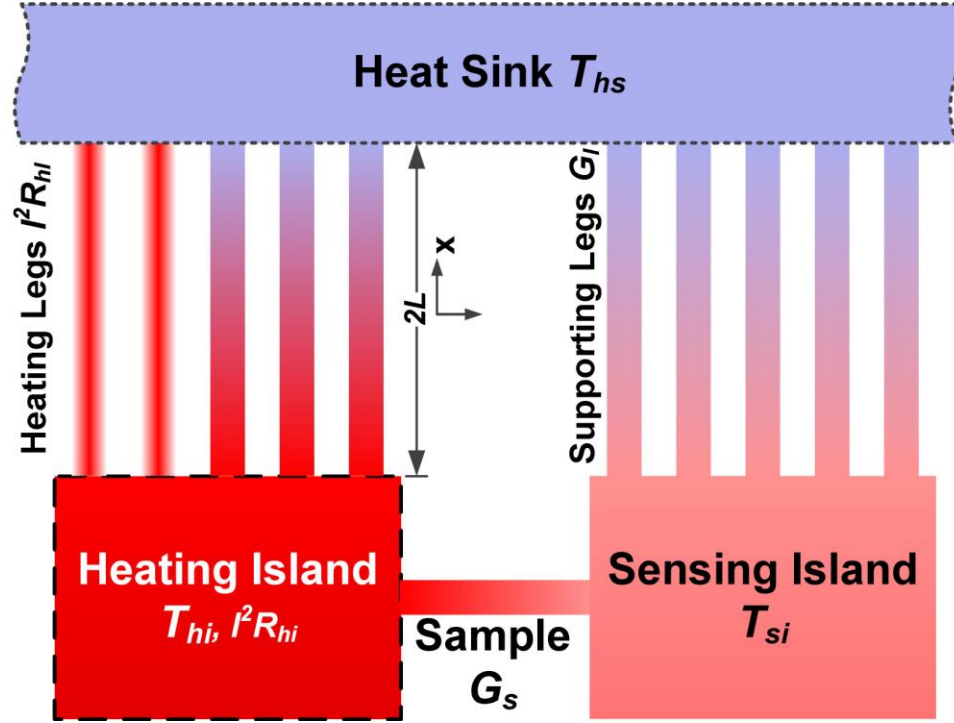


Figure 2-8 Thermal model based on the electrical connections in figure 2-7.

Figure 2-8 illustrates the heat transfer process during the experiments. As a result of the DC applied, Joule heat is produced on both two heating legs and the heating island, and it is dissipated to ambient environment through all 10 supporting legs. Whereas heat transferring through the sample increases the temperature of the sensing island, which further changes the resistance of the Pt coil on the sensing island. By measuring the resistance change with the lockin amplifier, we are able to identify the temperature of the sensing island, the same holds true for the heating island. By knowing the temperature difference across the sample, we can calculate its thermal conductivity.

As mentioned above, the Joule heating on the heating island is dissipated to the environment through the samples to be measured and the supporting legs. However, the

heat transfer through the two heating legs is not the same as the other supporting legs due to their internal Joule heating source. As shown in figure 2-8, considering the energy conservation for a heating island, the power of the heating island can be represented by:

$$P = I^2 R_{hi} = 2Q_{hl} + 3G_l (T_{hi} - T_{hs}) + G_s (T_{hi} - T_{si}), \quad (2.8)$$

where  $I$  is the DC applied onto the Pt coil on the heating island,  $R_{hi}$  is the electrical resistance of the Pt coil on the heating island,  $Q_{hl}$  is the heat dissipation through the heating leg,  $G_l$  and  $G_s$  are respectively the thermal conductance of a non-heated supporting leg and the nominal thermal conductance of the sample,  $T_{hi}$ ,  $T_{si}$ , and  $T_{hs}$  are the temperatures of the heating island, sensing island and the ambient environment. By applying the energy conservation equation for the sensing island, we have:

$$G_s (T_{si} - T_{hs}) = 5G_l (T_{si} - T_{hl}), \quad (2.9)$$

where we assume all the supporting legs have the same thermal conductance due to their exactly same designed dimensions, and thus the power of the heating island is described as:

$$P = I^2 R_{hi} = 2Q_{hl} + 3G_l (T_{hi} - T_{hs}) + 5G_l (T_{si} - T_{hl}), \quad (2.10)$$

In our experiment, the entire device is subject to a vacuum around  $1 \times 10^{-7}$  Torr, for which we can ignore the heat transfer via the residue air molecules and thermal radiation [100]. In figure 2-8, we define the origin of the x axis at the middle point of the supporting legs, and the length of the legs is  $2L$ , we have the heat equation for one of the heating legs as:

$$\frac{d^2 T}{dx^2} + \frac{\dot{q}}{k} = 0 . \quad (2.11)$$

The boundary conditions of one supporting leg is  $T(-L) = T_{hi}$  and  $T(L) = T_{hs}$ , and  $\dot{q}$  is the volumetric Joule heat as a result of the applied DC  $I$  on two of the supporting legs, it can be calculated as:

$$\dot{q} = \frac{I^2 R_l}{2 A_{cr} L}, \quad (2.12)$$

where  $R_L$  is the electrical resistance of one supporting leg,  $A_{cr}$  is the cross section area of the supporting leg. The solution of the equation 2.11 with its boundary conditions is:

$$T = \frac{\dot{q}}{2k} (L^2 - x^2) + \frac{T_{hs} - T_{hi}}{2L} x + \frac{T_{hs} + T_{hi}}{2}, \quad (2.13)$$

and therefore at  $x=-L$ , the interface between the heating island and one heating leg, the heat transfer can be derived from equation 2.13 according to the Fourier's Law:

$$Q_{hl} = -k_l A_{cr} \frac{dT}{dx} = -\dot{q} L A_{cr} + \frac{k_l A_{cr}}{2L} (T_{hi} - T_{hs}), \quad (2.14)$$

where  $k_l$  is thermal conductivity of the supporting leg. By combining equation 2.12 and 2.14, we have:

$$Q_{hl} = -k_l A_{cr} \frac{dT}{dx} = -\frac{I^2 R_l}{2} + \frac{k_l A_{cr}}{2L} (T_{hi} - T_{hs}), \quad (2.15)$$

if we define a thermal conductance of a heating leg as  $G_l = k_l A_{cr} / 2L$ , the heat transferred from the heating island through both heating legs is:

$$2Q_{hl} = -I^2 R_l + 2G_l (T_{hi} - T_{hs}), \quad (2.16)$$

and therefore equation 2.13 can be further written as:

$$P = I^2 R_{hi} = -I^2 R_l + 5G_l (T_{hi} - T_{hs}) + 5G_l (T_{si} - T_{hl}), \quad (2.17)$$

in equation 2.17, we notice that the capability of heat dissipation for the ten supporting legs is reduced by  $I^2 R_l$ , due to the Joule heat effect in two legs. From equations 2.9 and 2.17, we obtain:

$$T_{hi} - T_{hs} = \frac{(5G_l + G_s)}{5G_l(5G_l + 2G_s)} \gamma I^2 R_{hi}, \quad (2.18)$$

$$T_{si} - T_{hs} = \frac{G_s}{5G_l(5G_l + 2G_s)} \gamma I^2 R_{hi}, \quad (2.19)$$

where  $\gamma = (R_{hi} + R_l) / R_{hi}$ . Because the resistances of Pt coils change with temperature, and in our experiments,

$$R_{hi}(T) = R_{hi}(T_{hs}) + \alpha_{hi}(T - T_{hs}), \quad (2.20)$$

$$R_{si}(T) = R_{si}(T_{hs}) + \alpha_{si}(T - T_{hs}), \quad (2.21)$$

where  $\alpha_{hi}$  and  $\alpha_{si}$  are the nominal temperature coefficients of resistance for the heating and sensing islands, they can be obtained by fitting the electrical resistances of the Pt coils with temperature change. Hence, from equation 2.18 to 2.21, we have:

$$R_{hi}(T_{hi}) = R_{hi}(T_{hs}) + \Phi_{hi} I^2 R_{hi}, \quad (2.22)$$

$$R_{si}(T_{si}) = R_{si}(T_{hs}) + \Phi_{si} I^2 R_{hi}, \quad (2.23)$$

where,  $\Phi_{hi} = \alpha_{hi} \frac{(5G_l + G_s)}{5G_l(5G_l + 2G_s)} \gamma$ , and  $\Phi_{si} = \alpha_{si} \frac{G_s}{5G_l(5G_l + 2G_s)} \gamma$ ,  $\Phi_{hi}$  can be obtained

by fitting  $R_{hi}(T_{hi})$  with applied power  $I^2 R_{hi}$ , and similarly, for  $\Phi_{si}$ . Finally, we can calculate the nominal thermal conductance of the measured sample as:

$$G_s = \frac{\gamma \Phi_{si} / \alpha_{si}}{(\Phi_{hi} / \alpha_{hi})^2 - (\Phi_{si} / \alpha_{si})^2}, \quad (2.24)$$

$$5G_l = \frac{\Phi_{hi} \alpha_{si} - \Phi_{si} \alpha_{hi}}{\Phi_{si} \alpha_{hi}} G_s, \quad (2.25)$$

and therefore, with the dimensions of the measured sample characterized, the effective thermal conductivity  $k_{eff}$  is calculated as:

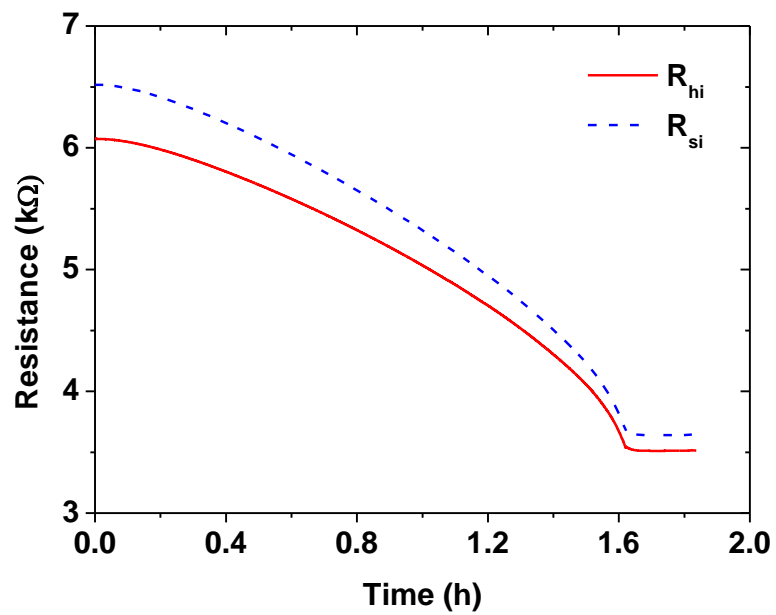
$$k_{eff} = \frac{L_s}{A_{cr}} G_s, \quad (2.26)$$

where  $L_s$  is the length of the measured nanomaterials, and  $A_{cr}$  is the cross section area. Here,  $k_{eff}$  can be regarded as the intrinsic thermal conductivity  $k_s$  of the measured sample only if the thermal contact resistance between the sample and the islands is negligible compared with the thermal resistance of the sample. This will be discussed case by case in the following chapters.

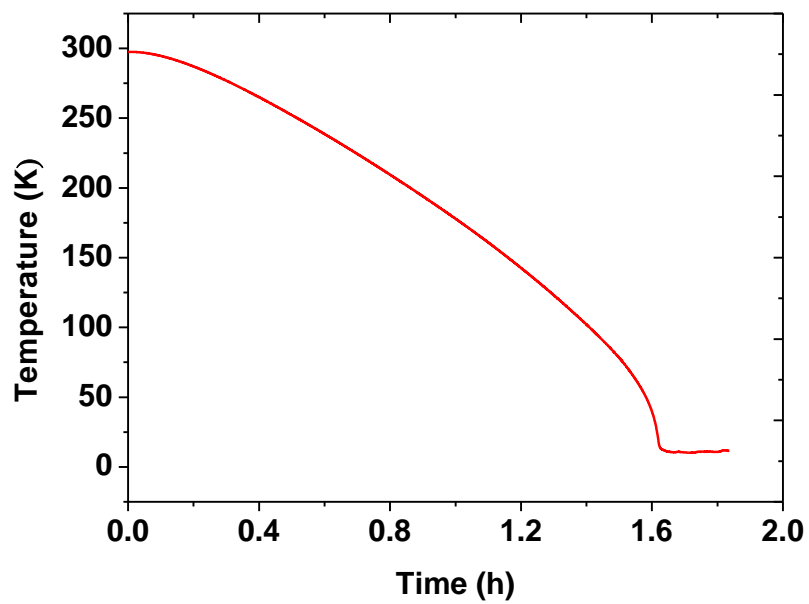
### 2.3.3 Measurement schemes and system characteristics

After a sample is successfully placed and secured on the thermal micro device, we then attach the micro device onto a 24 lead side brazed ceramic dual-in-line package (DIP) (Addison Engineering, Inc.). A small drop ( $<500\mu\text{m}$  in diameter) of silver epoxy is applied between the micro device's bottom surface and the package's surface to reduce the thermal contact resistance. The micro device and the package are connected using  $25\mu\text{m}$  diameter gold wires with a wedge wire bonder (West Bond Inc.). The package with the micro device assembled is then mounted on a copper finger in a cryostat (Model CCS-450 Optical high temperature refrigerator system, Janis research Co.). The global temperature of the cryostat can reach 10K with a closed cycle liquid helium compressor (CTI-Crogenics 8200 Compressor, Brooks automation, Inc.).

(a)



(b)



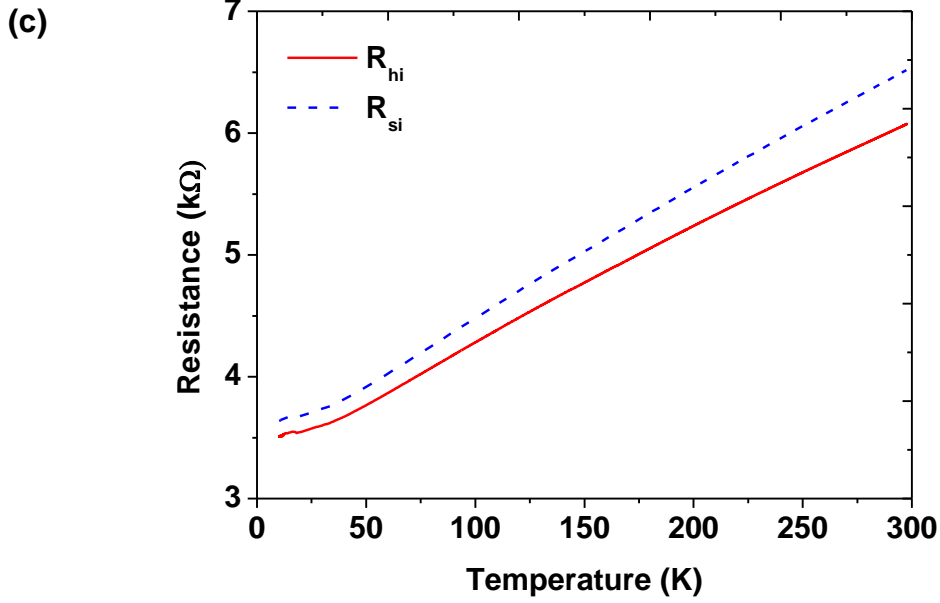


Figure 2-9 (a) The resistance changes of the heating island  $R_{hi}$  and the sensing island  $R_{si}$  with time during the cooling down process. (b) The global temperature change of heat sink  $T_{hs}$  with time. (c) The resistance changes of the heating island  $R_{hi}$  and the sensing island  $R_{si}$  with global temperature  $T_{hs}$ .

The cryostat chamber is evacuated to a vacuum level about  $1 \times 10^{-6}$  mbar ( $7.5 \times 10^{-7}$  Torr). Then we start the compressor to cool down the cryostat. As shown in figure 2-9(a,b), the system usually takes about 1.3 hours to reach 10K. From the cooling down process, we can also check the temperature coefficient of resistance (TCR) for both islands by fitting figure 2-9(a,b). It is noticed that in a low temperature range, especially where the global temperature is below 50K, the resistances are not linearly proportional to the temperature, and therefore, in this particular temperature range, we can't use linear fitting to get the TCRs. Although we can obtain a plot shown in figure 2-9(c), we normally don't use it for calculating the TCRs; instead, we measure the resistances before each steady state



measurement in order to obtain more accurate results. However, the TCRs fitted from both methods are very close with deviation  $<3\%$ . When the system stables at 10K, we begin to conduct our measurements at global temperatures with an increment of 10K.

Although it is impossible to put a thermal couple on the suspended structure and measure the local temperature of the sample, we can examine the temperature difference measured around the thermal diode and the islands by analyzing the transient heat conduction as shown in figure 2-10.

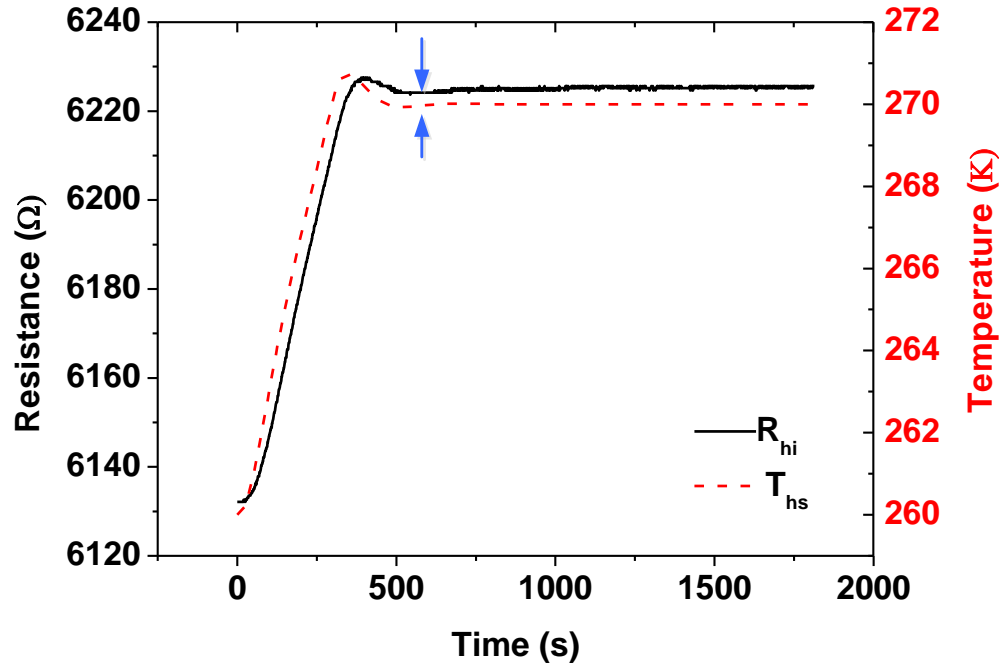


Figure 2-10 Temperature change (dashed line) measured by the thermal diode and the resistance change (black line) of the heating coil while the global temperature switches from 260K to 270K. The arrows indicate the point where heat transfer reaches to a steady state.

As show in figure 2-10, when we alter the global temperature from 260K to 270K,  $R_{hi}$  increases immediately, closely follows the trend of the global temperature, and reaches to a steady state at the same time when the global temperature is stable. The behavior indicates a very small time constant for the thermal system which includes the thermal couple at the back of the ceramic package and the measured sample. And therefore the thermal resistance is minute [101], together with negligible thermal radiation, we are able to reasonably assume that the temperature measured by the thermal diode is equal to the temperature on the sample before applying the DC current for sample characterization.

## **CHAPTER 3. Crystalline polyethylene (PE) nanofibers with the theoretical limit of Young's modulus**

### **3.1 Introduction**

Low-density materials such as polymers usually have low stiffness and strength [102]. In many fields, such as the electronics and space industries, lightweight materials with high strength and stiffness are of great importance in order to enhance reliability and portability. The search for these materials has led to the development of functional polymers that have remarkable mechanical properties [15], [32], [33], [103]. Although bulk polymers usually possess low strength and stiffness due to the entanglement of the molecular chains, crystalline polymers with well-packed and aligned molecular chains can theoretically provide a maximum stiffness that is controlled by covalent bond distortions. Over the past few decades, significant efforts have been devoted to enhancing the chain alignment (and thus the stiffness) through fabrication of polymer (e.g., polyethylene (PE)) fibers using methods such as solution/gel-based spinning [53], [62], [104], [105], surface growth [48], [49], [51], [106], and electrospinning [55], [57]–[59], [103]. Commercially-available oriented PE fibers, with diameters ranging from 10 to 30  $\mu\text{m}$ , currently achieve stiffness (i.e., Young's modulus) of  $\sim 150\text{GPa}$  at room temperature [32], [47], and reported values in the literature are generally below  $200\text{GPa}$  [15], [53], [62], [105], [107], [108]. The values obtained from these conventional methods are two orders of magnitude higher than the stiffness of bulk PE ( $\sim 1\text{GPa}$ ) [109]. Due to the presence of defects such as voids and entanglements, however, the measured values for

PE fibers still fall below the theoretical limit of a single PE molecule or PE single crystals, which is predicted to be as large as 374GPa [110].

Extensive work has been done to measure or predict the maximum Young's modulus of PE. In a PE crystal, interchain interactions have a negligible effect on axial stretching because the axial modulus is much higher than the radial modulus [111]. As such, the Young's modulus of a PE crystal (i.e., the maximum Young's modulus of PE), can be obtained with acceptable accuracy from the response of a single chain [112]. Interpretation of data from Raman spectroscopy and neutron inelastic scattering experiments yielded Young's modulus values of 358GPa [113], and 329GPa [113], [114], respectively. The Young's modulus was estimated from X-ray diffraction studies to be 283GPa [112]. At zero temperature, *ab initio* calculations predicted a Young's modulus of  $305 \pm 30$  GPa [112], and 374.5GPa [110], while that from empirical quantum mechanical calculations was reported to be 315~326GPa [112]. Overall, the predicted maximum Young's modulus of PE spans a range of 280-380GPa.

The microstructure of oriented microfibers consists of amorphous regions and nanocrystalline regions that are induced during the drawing process (also referred to as “Shish-Kebab” structures) [115]. The flow induced shish-kebab structures have been extensively reviewed [116]. Individual crystallites have been observed to be tens of nanometers in lateral dimension [106], [117], [118]. In contrast with microfibers, nanofibers have diameters comparable to the dimensions of the nanocrystallites and can thereby be used to minimize the extent of amorphous regions. With identical lengths, the volume of a nanofiber is at least two orders of magnitude smaller than that of a microfiber. The growth of the amorphous regions of the nanofiber is greatly prohibited,

thus a substantially lower concentration of defects will exist in a nanofiber than in a microfiber.

In this project, we fabricate crystalline PE nanofibers by combining a traditional gel-based spinning method with a tip-drawing technique [31]. We demonstrate, for the first time, that the Young's modulus of PE nanofibers with diameters from 70nm to 260nm can be as high as 312 +/-108GPa, within the range of the predictions of the theoretical maximum. This value is comparable with the best Young's modulus of metal alloys, but the density of the PE nanofibers is one order of magnitude smaller. Crystalline nanofibers, which can potentially achieve the ultimate modulus of polymers, thus open up a new route to manufacture light-weight and ultra-strong polymer fibers.

### **3.2 PE gel preparation and PE nanofiber fabrication**

The detailed fabrication process has been presented in Section 1, Chapter 2. Briefly, we first make PE gel by dissolving as-purchased PE power (ultrahigh molecular weight PE; Alfa Aesar) in Decalin at 140°C. To avoid oxygen induced degradation of the PE molecule, this gel preparation step is conducted in an argon-gas filled glove box. After the PE gel cools down to room temperature, we start to fabricate the PE nanofiber by a two-stage drawing process. In the first stage drawing, a glass tip with a diameter about 10  $\mu\text{m}$  is used to quickly pull a fiber from the PE gel which is heated at 120°C. The fiber normally has a diameter about several micron meters and a length about hundreds of micron meters. The fiber is further stretched in a heated air environment at 90~100°C. And in this second drawing stage, the diameter of the fiber can be reduced to a several hundred nanometers and sometime even below one hundred nanometers.

During the drawing process, a mixed elongational and shear flow is observed [73], [119]. The pulling velocity is on the order of  $50\mu\text{m s}^{-1}$ . The shear rate is estimated to be  $>1500\text{ s}^{-1}$ . The entire fabrication process is conducted under a dark-field stereo microscope and takes 1~2 minutes. The uniformity of nanofibers can be improved by using a lower pulling velocity. However, with the same shear duration, a higher pulling velocity generally results in a larger shear rate and a smaller diameter of a nanofiber.

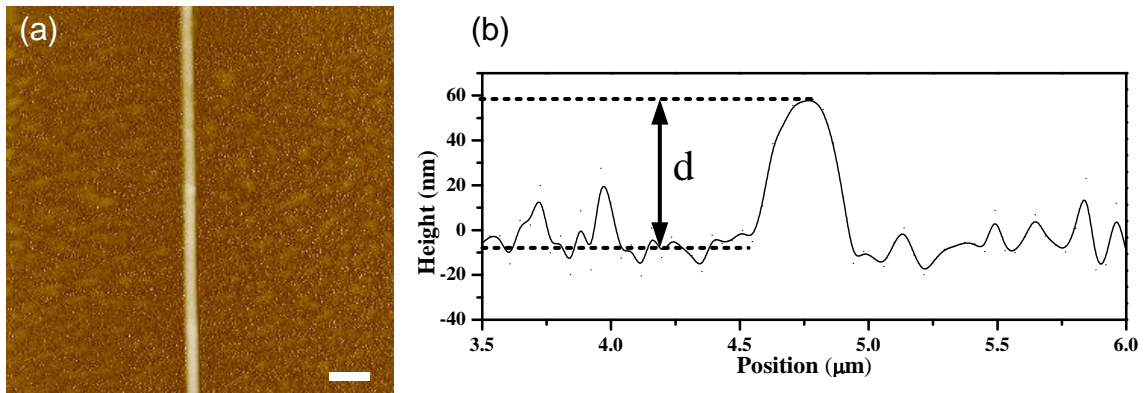


Figure 3-1 (a) AFM image of a PE nanofiber fabricated through two-stage heating process. (b) An AFM height curve corresponding to (a). The labeled height  $d$  is a representation of the diameter of the PE nanofiber. The rough surface is a result of reactive ion etching (RIE) of the silicon substrate during the trench fabrication. The scale bar is  $1\mu\text{m}$ .

The topography of the PE nanofibers fabricated with the two-stage drawing technique is characterized with an atomic force microscope (AFM) (Agilent 5500 SPM) as shown in figure 3-1(a). It can be observed that the size of the PE nanofiber is rather uniform across the AFM scanning range  $10\mu\text{m}$  by  $10\mu\text{m}$ . And there are no defects or contaminations over the length of the PE nanofiber. It can be concluded that the two-stage drawing

technique can reliably produce individual PE nanofibers with enough surface quality and size uniformity for mechanical property characterization. Even though AFM is able to yield very high spatial resolution, however as a result of profile broadening effect due to the tip-sample [120] convolution, the lateral width of the PE nanofibers is significantly larger than their real diameters. Figure 3-1(b) shows a height profile over a cross section of the PE nanofiber in figure 3-1(a). The lateral width of the PE fiber is about 360nm, which is much larger than the height  $d$  which is about 60nm. The elastic deformation of the fibers is proven to be very small during Young's modulus measurements; therefore, the height  $d$  of AFM profile is regarded as the true diameter of the PE nanofiber, the same principle applies throughout this research.

### **3.3 Analysis and characterization of the crystal structure of PE nanofibers**

The states of the PE molecules at each fabrication step are shown in figure 3-1. In the translucent gel (figure 3-1(a)) before the first stage heating, some PE molecular chains are folded locally in the form of small crystallites, usually termed as "lamellae", that are tens of nanometers in height and several microns in length. While some other molecular chains are randomly entangled and distributed in the gel, the "lamellae" serve as common joints for the entangled PE molecular chains. When the gel is heated above the PE melting temperature (120°C) during the first stage heating, both lamellae and entangled molecular chains are dissolved in the solvent, resulting in a uniformly clear solution that contains only entangled PE chain networks swollen by the solvent (figure 3-1(b)). When these PE molecular chains are stretched by the fine glass tip in the second stage heating,

they solidify and align in a common direction (figure 3-1(c)) because the solvent evaporates to the air.

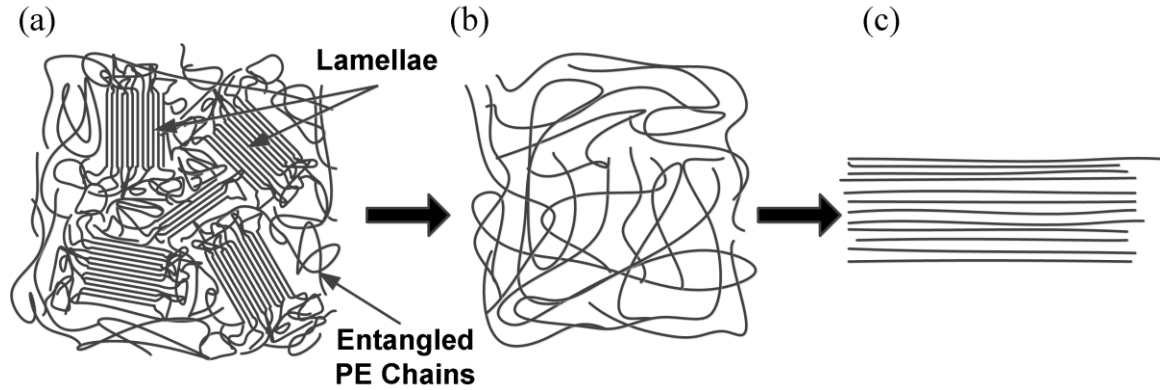


Figure 3-2 (a) Semi-crystalline PE gel with crystalline and amorphous regions. (b) PE molecular chains dissolved in Decalin solvent. The PE chains are randomly entangled in the solution. (c) Crystalline PE nanofiber with aligned chains.

Through the two drawing steps, the fiber diameter can be reduced from several microns to less than 100nm. For instance, a 3  $\mu\text{m}$  thick fiber that is drawn into a nanofiber 80nm in diameter has a draw ratio larger than 1400 (calculated by assuming volume conservation and a cylindrical shape). The large draw ratio enables extreme extension and alignment of the PE chains in the drawing direction due to a large shear rate [116] between chains along the nanofiber. The diameters of the final PE fibers are a few hundred nanometers (or even below 100 nm), which is comparable to the core sizes of Shish-Kebab structures [118]. In this case, the platelet (i.e., the Kebab) growth is significantly suppressed. The solidification of the PE nanofibers after the solvent evaporation maintains the alignment and orientation of the PE molecules (figure 3-1(c)). As a result, the number of defects and impurities is greatly reduced, compared with a



microfiber, which leads to an extremely high crystallinity (>90%). The fabricated PE nanofibers have diameters ranging from 70 to 500nm. An example of an 80.9nm diameter nanofiber is shown in figure 3-2(a). The selected area electron diffraction (SAED) pattern by transmission electron microscopy (TEM) in figure 3-2(b) shows the single-crystal nature of the PE nanofibers, with the *c*-axis (molecular) aligned with the drawing direction and the *a*-axis normal to the fiber axis. In comparison, the SAED patterns of thick fibers otherwise don't produce clear diffraction spots, for example, the SEAD pattern of a thick nanofiber (1050nm in diameter) is composed of unoriented rings of the 110 and 200 reflections from the orthorhombic PE crystals (figure 3-2(c,d)).

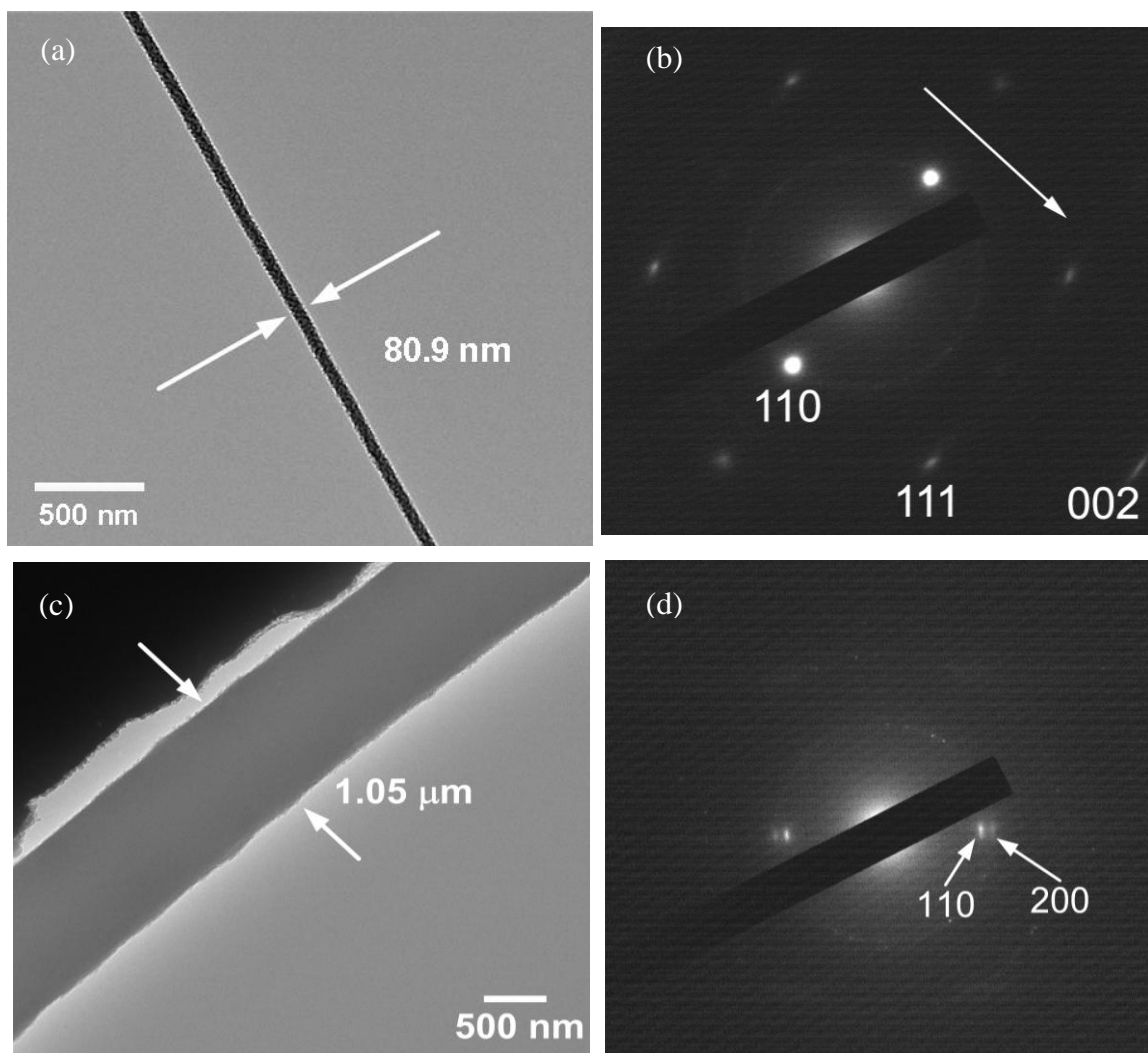


Figure 3-3 (a) A PE nanofiber with a diameter of 80.9nm lying on a bare silicon substrate. (b) TEM SAED pattern of the PE nanofiber in (a) which represents an orthorhombic crystal structure of the nanofiber. (c) A thick PE microfiber with a diameter of 1.05μm. (d) A SAED pattern of the microfiber in (c) shows continuous rings. These rings indicate a polycrystalline crystal structure of the thick PE microfiber. And the polycrystalline crystal structure is due to the random orientation of the lamellae in the thick PE microfiber.

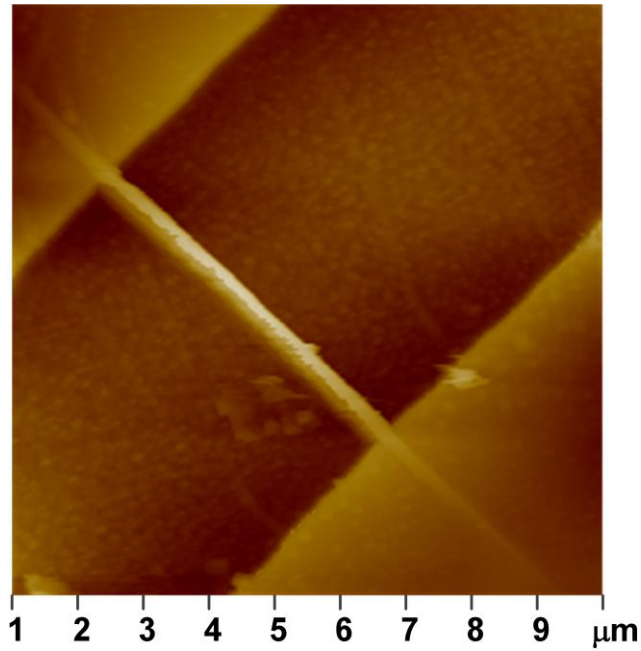
### **3.4 Young's modulus measurements by the force deflection spectroscopy (FDS) method**

A variety of techniques can be used to measure the Young's modulus. Tensile testing is one of the most common methods for characterizing the Young's moduli of thick fibers [121]–[123]. It is very challenging, however, to incorporate individual nanofibers with micrometer or millimeter length scale into the testing systems. While nanoindentation was used to measure the Young's moduli of a single silver nanowire [77], and ZnO nanobelts [78], relatively flat samples are required in order to avoid slip and friction between the indenter probe and the sample surface. Electromechanical resonance analysis by TEM is another alternative for measuring the Young's modulus of nanofibers [56], [76]. The drawback of this approach is that high-energy electron beams degrade polymeric materials during long-time exposure. The force deflection spectroscopy (FDS) technique has recently emerged as a reliable and flexible method for Young's modulus characterization of various nanofilaments [80], [82], [124]–[126]. Compared with the other characterization methods, the FDS technique has fewer requirements for nanoscale samples such as dimensions and material types, and can be easily implemented by an AFM. Here, we employ the FDS technique to measure the Young's moduli of PE nanofibers. A detailed description of this method can also be found in Section 2, Chapter 2.

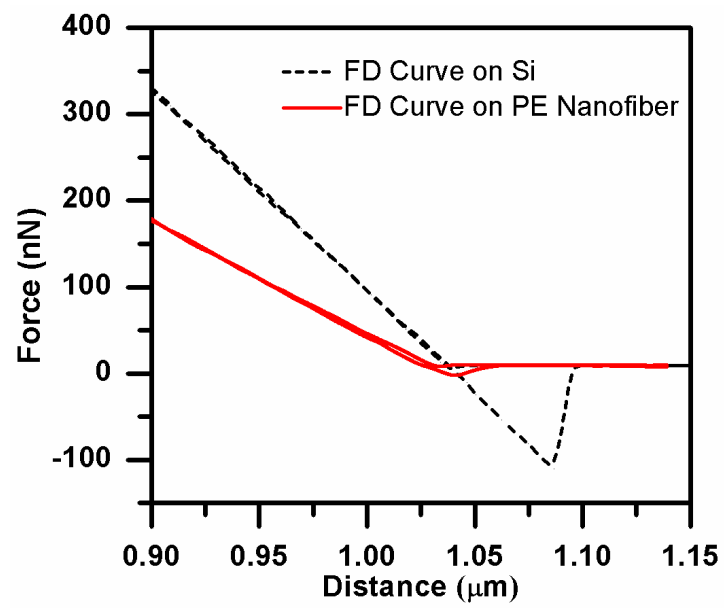
As shown in figure 3-3(a,b), a nanofiber is transferred to a 3mm by 3mm silicon substrate patterned with trenches. The trenches are 500 nm in depth with widths ranging from 5 to 10 $\mu$ m. They are fabricated on a 4-inch silicon wafer using photolithography and reactive

ion etching. The silicon wafer is sliced into the aforementioned substrates ( $3 \times 3 \text{ mm}^2$ ) so that a typical nanofiber spans the width of the chip. Under a high precision microscope (Nikon, Eclipse LV 100 DA-U), we use a tungsten tip (tip diameter  $\sim 1 \text{ }\mu\text{m}$ ) to clamp both ends of the nanofiber across the trenches with super glue (Gorilla Glue Inc., Precision Glue Pen).

(a)



(b)



(c)

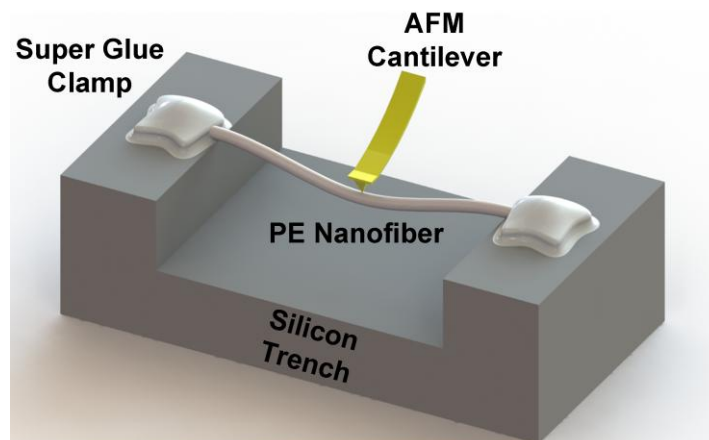


Figure 3-4 (a) AFM image of a typical PE nanofiber suspended over a silicon trench. (b) 3D model of the experimental setup for the FDS technique. (c) FD curves (approach and retraction) obtained on a silicon substrate and the middle point of a PE fiber over a trench.

We probe and measure the deflection of the PE nanofiber with the AFM. The cantilevers are standard silicon probes (Model: FMV; Bruker AFM Probes) with rectangular shapes. The spring constant of each cantilever is calibrated using the *in situ* thermal noise method based on the equipartition theorem [127]. In our experiments, the spring constant of the cantilever must be larger than 1N/m in order to obtain a measurable nanofiber deflection while keeping the bending of the cantilever in the linear region. By scanning the PE fiber using the AFM, we can locate its middle point across the trench. We perform FDS at this middle point to obtain force deflection (FD) curves. The FD curves show the relationship between a force applied on the cantilever and the vertical displacement of the sample. During the FDS test, the AFM scanner is able to move the tip to approach the sample and retract it from the sample. In a typical FD curve, the force is plotted against deflection for both approach and retraction. In figure 3-3(c), the approach and retraction curves overlap well, which indicates that the nanofibers behave linearly with low applied forces ( $< 150\text{nN}$ ).

The FD curve we obtain is a combination of the deflections of both the PE nanofiber (diameter 102 nm, length 5 $\mu\text{m}$ ) and the AFM cantilever. In order to isolate the deflection of the PE nanofiber, we also performed FDS measurement on a bare silicon surface to get an FD curve for the cantilever itself. Two FD curves from experiments, i.e., one on a PE

nanofiber and the other one on a silicon substrate, are shown in figure 3-3(c), including both approach and retraction curves. When the AFM tip is brought to contact with the rigid silicon substrate, only the AFM cantilever bends, and hence with the same applied force  $F$ , the deflection  $\Delta Z_s$  corresponding to the cantilever bending is smaller than the combined deflection  $\Delta Z_p$ . The difference between  $\Delta Z_p$  and  $\Delta Z_s$  is the downward deflection  $\delta$  of the PE nanofiber at its midpoint. By analyzing figure 3-3(c), we can express  $\delta$  by the slopes of these two FD curves as:

$$\delta = \Delta Z_p - \Delta Z_s = \frac{F}{k_p} - \frac{F}{k_s} = F \left( \frac{k_s - k_p}{k_s k_p} \right), \quad (3.1)$$

where  $k_s$  and  $k_p$  are the slopes of the FD curves in figure 1-3(c) for a silicon substrate and a PE nanofiber. When a homogeneous beam is fixed at both ends and a concentrated load is applied at its center, the expected maximum deflection at the center is given by [80]:

$$\delta = \frac{FL^3}{192EI}, \quad (3.2)$$

which is a solution of the Euler-Bernoulli beam equation provided that the longitudinal length of the beam's neutral plane does not change during the bending. In Equation 3.2,  $F$  is the concentrated central load,  $L$  is the length of the original beam, and  $I$  is the moment of inertia of the beam. Combining Equations 3.1, 3.2, and substituting the moment of inertia for a circular cross section,  $I = (\pi d^4)/64$ , the Young's modulus can be expressed as:

$$E = \frac{k_s k_p}{k_s - k_p} \frac{L^3}{192I} = \frac{k_s k_p}{k_s - k_p} \frac{L^3}{3\pi d^4}, \quad (3.3)$$

where  $d$  is the diameter of the nanofiber.

In figure 3-3(c), under a load of 150nN at the middle point, the deflection of a PE nanofiber with a diameter of 102nm is 51nm after subtracting the cantilever deformation from the combined deflection. We limit the deflections of the PE nanofibers to their diameters to: (1) Ensure that the Euler-Bernoulli beam theory is valid for our measurements, and (2) Avoid damage and breakage of both the AFM cantilever and the PE nanofiber. From figure 1-3(c), we can also observe that in this small deflection range, the deflections of the cantilever and the PE nanofiber are both in a linear region, indicating that the deformations are elastic. Within the limited range of force and deflection, we also perform FDS tests on nanofibers placed directly on the substrate. The slopes of the FD curves are nearly identical to those obtained from bare silicon substrates. This result confirms that the tip indentation into the nanofiber and deformation of the nanofiber cross section are both negligible.

#### **3.4.1 Verification of the FDS technique with polymethyl methacrylate (PMMA) fibers**

In order to demonstrate the validity of our experimental setup for the FDS technique, we performed FDS on PMMA nanofibers as well. Figure 3-4(a) shows an AFM image of a PMMA fiber suspended over the trench. For a typical PMMA fiber with a diameter of 402nm, we measure a Young's modulus of 2.1GPa. The FD curves of this fiber are shown in figure 3-4(b). In Table 3-1, we summarized the data obtained for two PMMA fibers. Here,  $d$  is the diameter of the PMMA obtained by AFM scanning,  $L$  is the fiber length suspended over the trench,  $k_s$  and  $k_f$  are the slopes obtained from the FD curves on silicon and on the middle point of the fiber. The Young's moduli ( $E$ ) we obtained for these PMMA fibers are close to the range 2.5~3.1GPa reported by previous research [128].



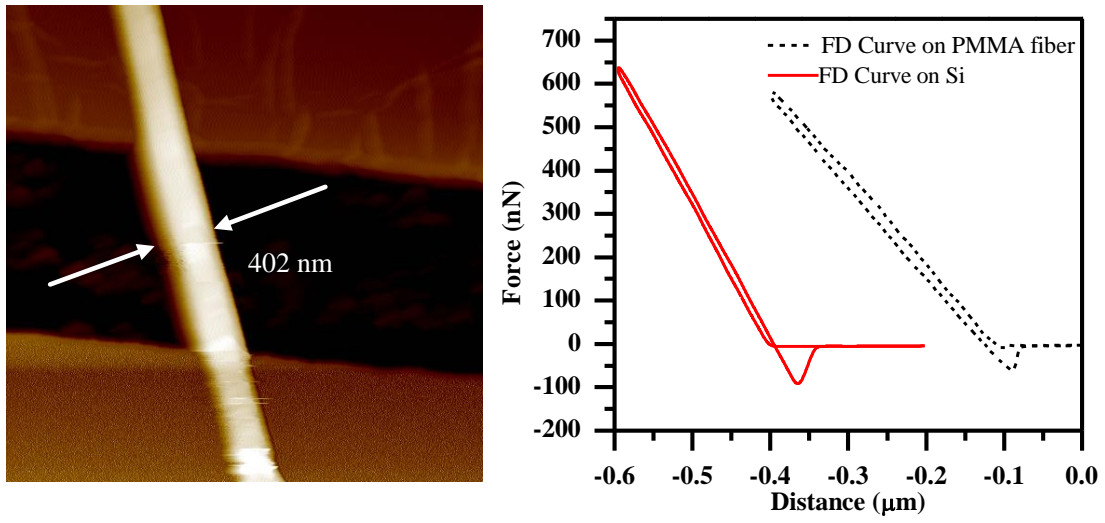


Figure 3-5 (a) A typical PMMA fiber suspended over a silicon trench. (b) FD curves obtained on a silicon substrate and the middle point of a PMMA fiber over a trench.

Table 3-1 FDS performed on PMMA fibers

	<b>d (nm)</b>	<b>L (m)</b>	<b><math>k_s</math> (nN/m)</b>	<b><math>k_t</math> (nN/m)</b>	<b>E (GPa)</b>
<b>Fiber 1</b>	402	4.5	3250	2050	2.1
<b>Fiber 2</b>	544	4.2	2658	1797	1.06

### 3.4.2 Finite element analysis of the FDS measurement on the PE nanofibers

When applying Equation 3.3, the Euler-Bernoulli beam theory assumes that the PE nanofiber is an isotropic material. For nanofibers, however, the axial Young's modulus is much higher than the radial one because the carbon covalent bond along the PE chain is much stronger than chain-chain van der Waals' interactions. Therefore, in order to identify the impact of the anisotropy of the nanofiber on our FDS measurements, we also performed finite element analysis (FEA) for a nanofiber with the same dimensions (diameter 102 nm, length 5 $\mu$ m) as the sample that yielded the FDS curves in figure 3-3(c).

In terms of the orthorhombic PE crystal structure (figure 3-5(a)), we assume that the fiber has an axial ( $z$  direction) Young's modulus of 343GPa (obtained from figure 3-3(c)) and that the Young's moduli in  $x$  and  $y$  directions are 9GPa and 9.5GPa, as obtained from theoretical predictions [14], [111], [129]. And table 3-2 shows the 9 independent elastic constants for an orthorhombic crystal structure, these elastic constants are in Voigt notation and used in our FEA simulation. For an anisotropic PE fiber with a center load of 150nN (figure 3-5(b)), the maximum deflection of the middle point is 62nm, as shown in the FEA simulation result (figure 3-5(b)). It is worth to note that the elastic constants in the elasticity matrix vary in a large range reported from different groups [14], [111], [129], especially for a PE nanofiber, there is still a lack of precise models. However, the deflections are not very sensitive to  $c_{11}$ ,  $c_{12}$ ,  $c_{13}$ ,  $c_{22}$ ,  $c_{23}$  according to the FEA simulations.  $c_{44}$ ,  $c_{55}$ ,  $c_{66}$  do affect the results in a small scale, and if they are bigger than 20GPa, the deflections results become bigger and approach to the results from the isotropic model.

Table 3-2 Elasticity Matrix (in GPa) for the material property used in FEA model

<b>9</b>	<b>5.2</b>	<b>5</b>	<b>0</b>	<b>0</b>	<b>0</b>
<b>5.2</b>	<b>9.5</b>	<b>6</b>	<b>0</b>	<b>0</b>	<b>0</b>
<b>5</b>	<b>6</b>	<b>343</b>	<b>0</b>	<b>0</b>	<b>0</b>
<b>0</b>	<b>0</b>	<b>0</b>	<b>10</b>	<b>0</b>	<b>0</b>
<b>0</b>	<b>0</b>	<b>0</b>	<b>0</b>	<b>10</b>	<b>0</b>
<b>0</b>	<b>0</b>	<b>0</b>	<b>0</b>	<b>0</b>	<b>10</b>

For an isotropic PE fiber with the same dimensions, the maximum deflection from the FEA simulation is 54.2nm (figure 3-5(c)), which agrees well with the analytical solution (54.1 nm) and the experimental result shown in figure 1-3(c). And in the simulation, we apply a Poission's ratio of 0.09 [14]. We note that the anisotropic model gives a deflection 10% higher than the isotropic model and the analytical solution. This result is consistent with another set of FEA simulations for a load of 200nm on the same nanofiber. Since the anisotropic model yields a larger deflection, the derivation in our experiment will gives a lower Young's modulus, which indicates that the real axial Young's modulus of the PE fiber is slightly higher (12% in this case) than our experimentally derived results. For the reported results, we will extract the Young's modulus using the isotropic model rather than FEA because the isotropic model is much simpler and the moduli in the  $x$  and  $y$  are difficult to measure experimentally.

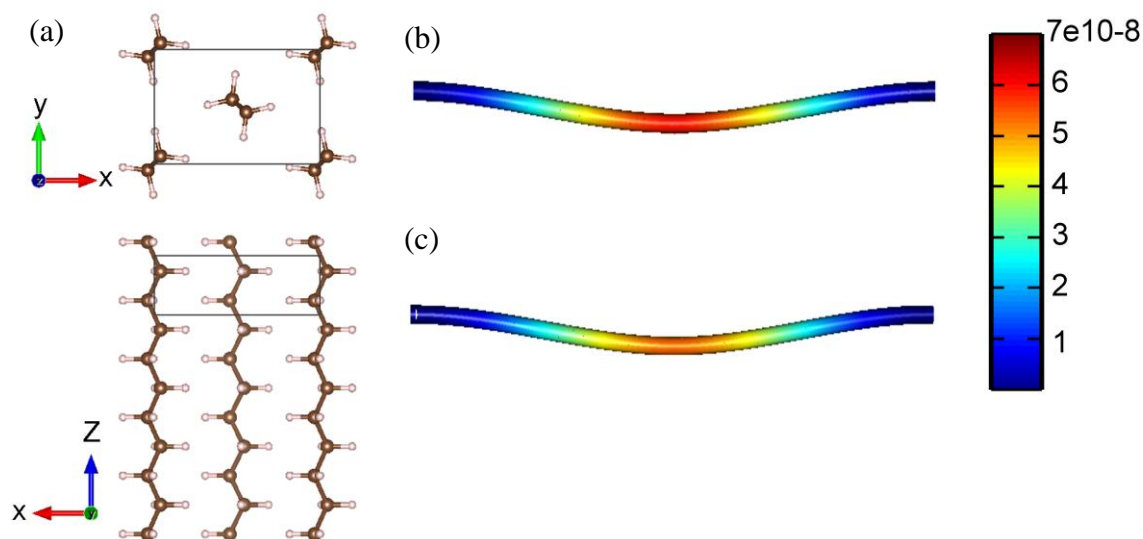


Figure 3-6 (a) Orthorhombic crystal structure of PE. FEA simulations on a PE fiber 102nm in diameter, assuming the fiber is (b) anisotropic and (c) isotropic. The color bar represents the deflection of the fiber in meters.

### 3.5 Results and discussion

#### 3.5.1 The Young's modulus of PE nanofibers calculated according to the FDS technique

Before calculating the Young's modulus, the clamping conditions of the nanofiber at the edges of the trench should be carefully examined because they determine if equation 3.3 is applicable. In our experiments, each FDS test is performed at least five times on the silicon substrate and the PE nanofiber for each sample. For our samples, the slopes of the resulting FD curves on a nanofiber deviate randomly in a very small range ( $\pm 3\sim 4\%$ ). This small deviation confirms that the nanofibers are tightly fixed at both ends and that they don't slide, lift off from the substrate, or plastically deform. Therefore, the adhesion from

the glue and the Van der Waals force between the PE nanofiber and the silicon substrate validate the fixed ends approximation made in equation 3.2. In addition, as mentioned in previous reports, the ratio between the suspended length of the nanofiber and its outer diameter should be at least 16 in order to eliminate the shear deformation of the nanofibers during the FDS test [124]. In our experiments, this ratio is larger than 40 for all measured samples. We can thus properly assume that there exist only elastic tensile and compressive deformations.

Young's moduli have been calculated and are plotted in figure 3-6 for 47 PE samples with diameters from 70nm to 260nm. The average Young's modulus is 312GPa with a standard deviation of 108GPa. This result is significantly higher than the previous experiment results, which all fall below 200GPa [15], [107], [108]. We attribute the exceptionally high Young's modulus to the nearly 100% crystallinity created by the ultra-high drawing process, as shown in figure 3-2(b). Besides the high Young's modulus, we notice that there is a large variation among the measurements. Even at a large draw ratio or shear rate, however, some of the folded or entangled chains cannot be completely eliminated and thus remain in the fiber as defects. Those defects can significantly reduce the Young's modulus of nanofibers. Hence, some nanofibers have a smaller Young's modulus around 200GPa. We believe that there are two potential causes: real variation of different PE nanofibers and the experimental uncertainty. During the fabrication process, when the diameter of the PE fibers reaches nanometer scale, especially for the fibers below 100nm, it is very difficult to precisely control the quality of each nanofiber due to the variation of local temperature, shear force, and evaporation rate of solvent. These parameters are crucial for the formation of the crystallized nanofibers and lead to the

variation of Young's modulus between the samples with the same fiber diameter, especially in the nanometer level.

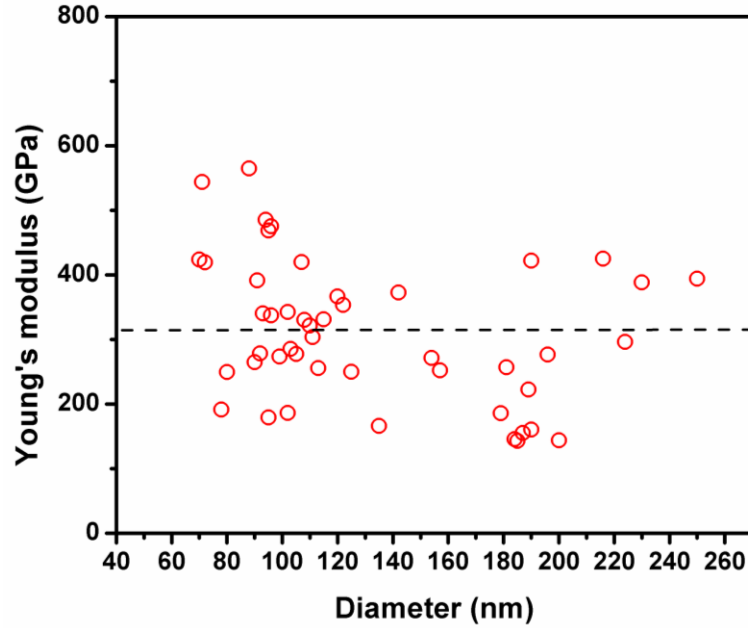


Figure 3-7 Young's moduli measured for PE nanofibers ranging from 70nm to 260nm in diameter. The average measured Young's modulus indicated by the dash line is  $312\text{GPa} \pm 108\text{GPa}$ .

### 3.5.2 Size effect of the Young's modulus

A size effect has been reported regarding Young's moduli of electro-spun polymer fibers [130]–[132]. When the diameter of fibers decreases, the Young's modulus is higher. In our experimental results, we don't observe a clear correlation between the diameter of PE nanofibers and the Young's modulus. This is probably caused by the quality of the nanofibers fabricated with different techniques. With electro-spun technique, a large amount of amorphous regions still exist after the fast spinning process, resulting a

crystallinity lower than 80% [59]. However the crystallinity of our nanofibers is close to 100% so that there isn't much room for the surface effects or supramolecular structure [132] to come into play.

### 3.5.3 Uncertainty analysis

The total uncertainty in the measurements is a composition of multiple uncertainties propagating throughout the experiment. The general formulation for  $E$  is:

$$E = \frac{k_s k_p}{k_s - k_p} \frac{L^3}{3\pi d^4}. \quad (3.4)$$

Let  $K = \frac{k_s k_p}{k_s - k_p}$  and from uncertainty propagation rules, the total uncertainty in  $E$  is:

$$\left( \frac{\delta E}{E} \right)^2 = \left( \frac{\delta K}{K} \right)^2 + \left( 3 \frac{\delta L}{L} \right)^2 + \left( 4 \frac{\delta d}{d} \right)^2, \quad (3.5)$$

where the uncertainty of the nanofiber length is less than 4% after sensitivity calibration of the AFM. The diameter of the fibers is measured at multiple locations along the fiber axial direction. The uncertainty of the diameter is less than 8% accounting for the AFM cantilever sensitivity in the vertical direction and the possible contamination on the nanofiber. Therefore, to completely determine the total uncertainty, the uncertainty of  $K$  has to be derived.

Based on uncertainty propagation rules,

$$\left(\frac{\delta K}{K}\right)^2 = \frac{k_s^2 \left(\frac{\delta k_p}{k_p}\right)^2 + k_p^2 \left(\frac{\delta k_s}{k_s}\right)^2}{(k_p - k_s)^2}, \quad (3.6)$$

where  $k_p$  and  $k_s$  are in nN/m. These two slopes are directly measured in our experiments with a dimension of V/nm. Therefore, we transfer the dimensions of these two slopes using the following equations,

$$k_s = k_{sv} s k_{fc}, \quad (3.7)$$

$$k_p = k_{pv} s k_{fc}, \quad (3.8)$$

where  $k_{sv}$  and  $k_{pv}$  are slopes in V/nm,  $s$  is the deflection sensitivity of the cantilever when it touches on a bare silicon surface, it is also called photodiode sensitivity elsewhere [133], and  $k_{fc}$  is the force constant of the cantilever. In our experiments, by performing FDS on the silicon surface and the nanofiber for at least five times separately, the uncertainties of  $k_{sv}$  and  $k_{pv}$  are 1.5% and 3.74%. Through multiple deflection tests, the uncertainty of  $s$  is obtained to be less than 1.5%. The uncertainty of the force constant  $k_{fc}$  is 5% [134]. Therefore,

$$\left(\frac{\delta k_s}{k_s}\right)^2 = \left(\frac{\delta k_{sv}}{k_{sv}}\right)^2 + \left(\frac{\delta s}{s}\right)^2 + \left(\frac{\delta k_{fc}}{k_{fc}}\right)^2 = 0.015^2 + 0.015^2 + 0.05^2 = 0.003, \quad (3.9)$$

and

$$\left(\frac{\delta k_p}{k_p}\right)^2 = \left(\frac{\delta k_{pv}}{k_{pv}}\right)^2 + \left(\frac{\delta s}{s}\right)^2 + \left(\frac{\delta k_{fc}}{k_{fc}}\right)^2 = 0.0374^2 + 0.015^2 + 0.1^2 = 0.0041. \quad (3.10)$$



For a typical measurement,  $k_s = 2340 \text{ nN/m}$  and  $k_p = 1288 \text{ nN/m}$ , and combined with equation (3.9) and equation (3.10), we have:

$$\left( \frac{\delta D}{D} \right)^2 = \frac{2340^2 (0.0041)^2 + 1288^2 (0.003)^2}{(2340 - 1288)^2} = 0.0248, \quad (3.11)$$

substituting equation (3.11) in equation (3.7), we have:

$$\frac{\delta E}{E} = \sqrt{0.0248 + (3 * 0.04)^2 + (4 * 0.08)^2} = 0.376 = 37.6\% . \quad (3.12)$$

As demonstrated in the uncertainty analysis above, in the FDS method, the measured Young's modulus depends on the characterizations of the PE fiber sizes and AFM cantilever spring constants, which are the dominant sources of errors. The suspended length can be precisely measured by AFM to be within 5% uncertainty. Given that the nanofiber diameter appears to the fourth power in equation 3.3, a  $\sim 8\%$  uncertainty is expected when the diameters are below 100nm. Accounting for uncertainties in the cantilever and nanofiber dimensions, together with the photodiode sensitivity, the maximum relative error in the nanofiber modulus is estimated to be less than 40% as shown in the equation 3.12. Our experimental uncertainties are consistent with previous measurements based on FDS [81].

### 3.6 Conclusion

In conclusion, our experimental results demonstrate a practical method to achieve the ultimate Young's modulus of polymers using nanofibers. With the ultra-drawing technique, we have obtained PE nanofibers with diameters in a range of 70 to 260nm. The PE nanofibers in our experiments possess extremely high crystallinity (i.e., a lower

concentration of defects), which leads to the enhanced Young's modulus. The high Young's modulus of 312GPa of the PE nanofibers can significantly expand the use of PE in various applications which require high strength but low density (below 1000kg/m<sup>3</sup>). Our fabrication method and mechanical characterization technique may be extended to other polymeric materials, such as PMMA, polyacrylonitrile (PAN), and thus pave the way to understand and harness the high strength of polymers.

## CHAPTER 4. Tunable thermal transport in Polysilsesquioxane (PSQ) hybrid crystals

### 4.1 Introduction

Advances in polymer sciences have enabled large-scale synthesis of low-cost polymers with a broad range of properties, leading to various applications ranging from the vulcanized rubber used in the tires of cars to synthetic fibers for creating many common textiles. Bulk polymers are usually in an amorphous form due to the entanglement of polymer molecules, and weak van de Waals bonds between polymer molecules dominate their thermal transport properties. As a result, polymers are generally regarded as thermal insulators with thermal conductivity on the order of 0.1W/mK at room temperature [135]. Most attempts for improving polymer thermal conductivity have been focused on fabricating composite materials, in which high thermal conductivity additives, such as metallic nanoparticles [136], [137] and carbon nanotubes[138], [139], are embedded in polymer matrices. However, the thermal conductivity enhancement of polymer composites is generally limited to within one order of magnitude, significantly below the prediction from the engineering rule of mixing based on effective medium rationale. This discrepancy is attributed to high interfacial thermal resistance between the additives and the polymer matrix.

In contrast with bulk polymers, recent theoretical work suggests that individual polymer molecules, e.g., polyethylene (PE) molecules, are predicted have extremely high thermal conductivity (e.g., ~350W/m K for long PE molecules) because of the strong covalent bonds in molecules [26]. To harness the intrinsic high thermal conductivity of individual

molecules, the molecules in a polymer need to be aligned like a single crystal. The alignment of polymer molecules can be increased by mechanically stretching bulk samples into fibers or thin films [47], [52], [62], [140]. For example, highly stretched crystalline PE nanofibers were demonstrated to have a high thermal conductivity of  $\sim 100\text{W/m K}$  [31]. Due to the chain-chain van der Waals' interaction induced phonon-phonon scattering within each chain, the thermal conductivity of the PE fibers is lower than the theoretically predicted thermal conductivity ( $\sim 350\text{W/mK}$ ) [26] of a single PE chain. Nevertheless, it is technically difficult to employ conventional low-cost chemical methods to synthesize polymer crystals with aligned molecular chains. Whereas, hydrogen bond based polymer crystals can be chemically synthesized in a large scale and potentially have a thermal conductivity higher than that of bulk polymers. In terms of bond strength, hydrogen bonds have a bond strength ( $<5\text{kcal/mol}$ ) that lies in between van der Waals bonds (bond strength  $\sim 1\text{kcal/mol}$ ) and covalent bonds (bond strength on the order of  $100\text{kcal/mol}$ ) [37], [41], [42]. In this chapter, we report the thermal transport measurements and modeling of aligned chains of hydrogen bond based polysilsesquioxane (PSQ) hybrid crystals. We also demonstrate their tunable thermal conductivity by varying the length of alkyl chains.

## **4.2 PSQ synthesis and characterization**

Organic-inorganic hybrid materials [141] have attracted significant interest over the past decades because of their composited tailored properties from both organic and inorganic components [142]–[144]. As one type of hybrid polymers, the PSQ hybrid crystals are synthesized by bridging two Si atoms with organic groups. More importantly, it allows sufficient design flexibility to molecular bonding and alignment across intermolecular

connections. The PSQ hybrid crystals studied in this work are prepared from two precursors with hexylene- and octylene-bridged groups. As shown in figure 4-1(a,b) hexylene- and octylene-bridged crystals are composed of 18- and 22-membered bimolecular rings as repeating units, respectively. Three-dimensional molecular crystalline structures are formed by linking the rings with hydrogen bonds between silanol groups (Si-O-H) and weak van der Waal's interactions between alkyl chains. In a typical synthesis of crystalline PSQ (figure 4-1(c,d) ) bis-(triethoxysilyl)octane (BTO) or bis-(trimethoxysilyl) hexane (BTH) is dissolved in Tetrahydrofuran (THF) under nitrogen and the mixture is cooled down to 5 °C. Then, hydrochloric (HCl) acid is added to this solution, allowing hydrolysis of the precursor. The resultant mixture is stirred for 1 hour and kept static for 1 day at the same temperature. Finally, the white product is filtered, washed with ethanol and dried in air. To synthesize amorphous PSQ as a comparison (figure 4-1(e,f)), BTO or BTH was added to a solution of THF and HCl under nitrogen. The mixture was stirred for 1 hour and stood for 1 day.

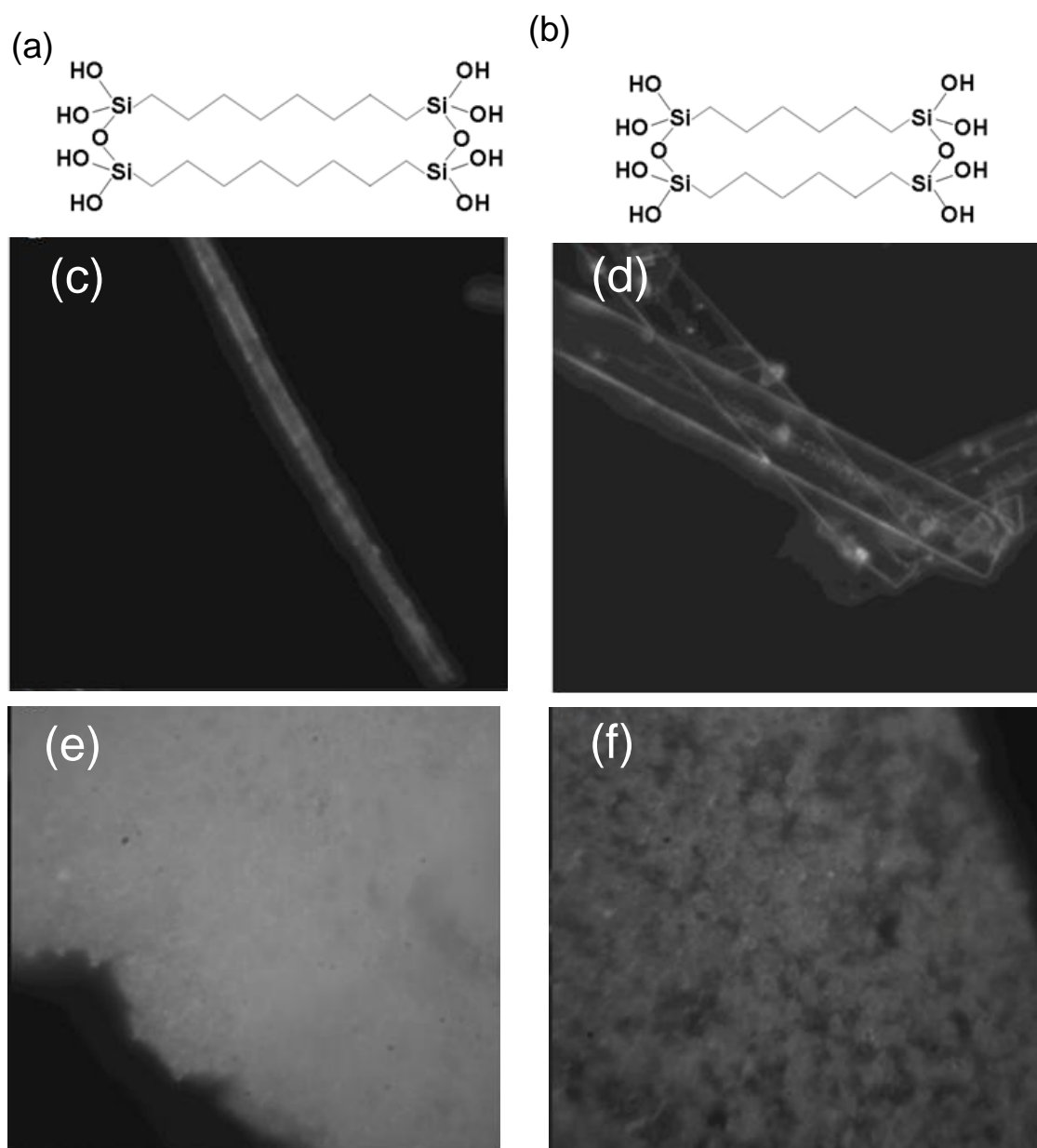


Figure 4-1 2D projection graphs of repeating units of (a) octylene-bridged and (b) hexylene-bridged PSQ fibers. Dark field optical images of PSQ products, Octylene-bridged PSQ microbeam (c) crystalline; (e) Amorphous. Hexylene -bridged PSQ microbeam (d) crystalline; (f) Amorphous.

The morphologies of PSQ hybrid crystals are characterized by a standard dark field optical microscopy with 50x objective (NA=0.65), as shown in figure 4-1(c,d). In comparison with their amorphous counterparts (figure 4-1(e,f)), octylene-bridged and hexylene-bridged PSQ crystalline beams have clearly defined geometries and small surface roughness. The typical dimensions are 1~2 $\mu\text{m}$  in thickness and 2 $\mu\text{m}$  in width. Figure 4-2(a) shows the infrared spectroscopy of octylene-bridged PSQ crystals, the broadband peak around 3250 $\text{cm}^{-1}$  is assigned to the stretching vibration of silanol groups, which indicate that the hydrogen bonded silanol groups restrict the bonding directions [21]. In the amorphous polymer, this broad peak shifts to 3500 $\text{cm}^{-1}$  indicating more isolated silanol groups, which render free three-dimensional cross-link amorphous and less dense structure because the degree of condensation is directly related to the number of residual silanol groups [144]. The bands centered at 2920 and 2854 $\text{cm}^{-1}$  correspond to the symmetric and anti-symmetric stretching vibration modes, respectively, of the C-H in the methylene unit. The narrow bands in the beam (FWHM=22 and 13) compared to those in the amorphous structure (FWHM=43 and 26) indicates the high crystallinity of the internal structure of beams, which is consistent with the observation of in the crystalline alkylsiloxanes [145]. The peak at 1464  $\text{cm}^{-1}$  corresponds to a CH<sub>2</sub> scissoring deformation mode, and a singlet at 906 $\text{cm}^{-1}$  is assigned to the Si-OH stretching mode. Several bands observed between 1165 and 1385 $\text{cm}^{-1}$  are attributed to coupled CH<sub>2</sub> wag modes. All these modes in the beam structure are significantly narrower than that of the amorphous structure, which again confirms its high crystallinity. To quantitatively characterize the crystallinity of the PSQ beams, we conduct powder X-ray diffraction (XRD) analysis. Both hexylene-bridged and octylene-bridged PSQ crystals have similarly

high crystallinity. For example, the crystallinity from the XRD pattern (figure 4-2(b)) is estimated to be ~ 90 % for octylene-bridged PSQ crystals.

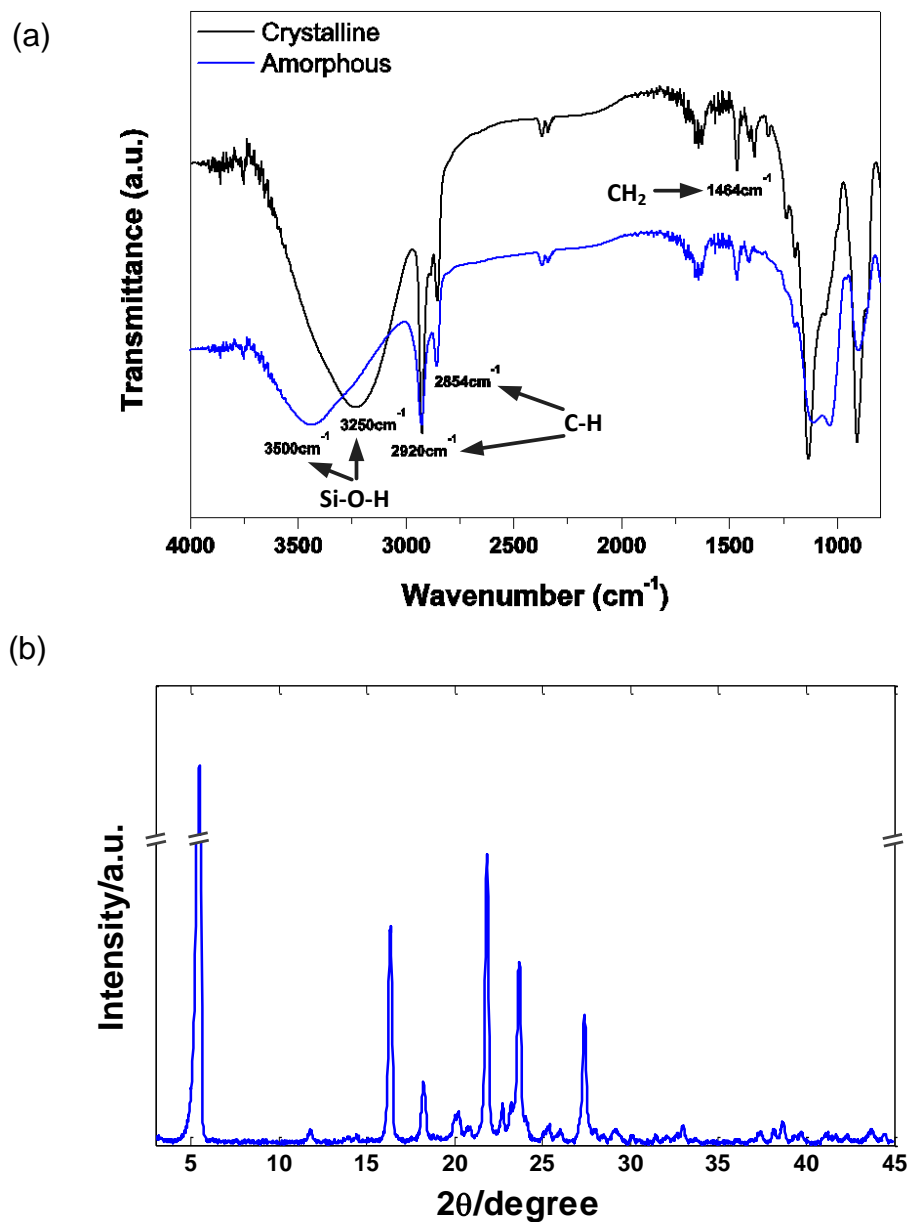


Figure 4-2 (a) Fourier transform infrared spectroscopy (FTIR) spectra of crystalline and amorphous bridged PSQ. (b) Powder X-ray diffraction pattern of octylene-bridged PSQ fibers.



### 4.3 Thermal characterization with suspended micro thermal device

A variety of methods, such as  $3\omega$  method [89], [92], [146], Raman spectroscopy [147]–[149], and cantilever techniques [31], [150], have been used to characterize the thermal properties of materials in micro/nano scale. However, for  $3\omega$  method, usually a mirror-like surface of the sample is required for fabricating a metallic thin heater line and connecting pads, and the thermal model which the method is based on needs a relatively thick sample substrate to satisfy the semi-infinite assumption. While for Raman spectroscopy, a two dimensional thin film is used to cover a channel/hole structure on a substrate, Raman excitation laser incidents on the suspended thin film to raise the temperature. Therefore, this method requires a relative larger area than the laser spot size in order to fit its one dimensional heat transfer model. In the cantilever technique, lasers are used to heat the cantilever and one end of the sample. Due to the laser heating, the cantilever subjects to mechanical deflection which can be detected by a photosensitive detector. The entire system is similar to a modified atomic force microscopy (AFM) system, which is often expensive and requires delicate calibration.

In our experiment, because PSQ crystals are in rectangular beam shapes, the thickness is only around  $1\mu\text{m}$ , and the width is about several micrometers. It is impossible to go through a conventional photolithography process for a  $3\omega$  testing device. At the same time, the beam shape excludes the implement of the Raman spectroscopy due to its mismatch on the heat transfer model. The cantilever method seems feasible; however, the long experiment setup and calibration process hinders an immediate application. Consequently, we choose the suspended micro thermal device to characterize the thermal

properties [151], [152], due to its very high accuracy and reliability, even though rather time consuming device fabrication and sample manipulation processes are involved.

#### 4.3.1 Experiment setup and measurement scheme

The thermal device with a PSQ beam assembled is illustrated in figure 4-3. The detailed description of the measurement scheme is mentioned in Chapter 2, Section 3. Briefly, the device has two suspended SiNx islands fabricated with low pressure chemical vapor deposition and conventional photolithography. On the top of the SiNx islands, a 30nm thick platinum (Pt) layer is sputtered and patterned to thin serpentine coils. The patterned Pt coil functions respectively as a heater and thermometer for the heating island and a thermometer for the sensing island, while they are isothermal. And a PSQ beam is placed on these two islands to transport heat from the hot island to the cold island. At a global temperature  $T_{hs}$ , a temperature difference  $\Delta T$  can be established between the heating and sensing islands by applying a DC current to the heating island. This temperature difference is obtained by measuring the electrical resistances and the temperature coefficients of resistance (TCR) of both islands. With the knowledge of the temperature difference  $\Delta T$ , the heat flux  $Q_s$  across the PSQ beams, and the beam length  $L_s$  and cross section area  $A_{cr}$ , and by solving the steady state heat transfer equations, the thermal conductivity of the PSQ beams can be calculated as [153]:

$$k = \frac{G_s L_s}{A_{cr}} = \frac{Q_s}{\Delta T} \frac{L_s}{A_{cr}}, \quad (4.1)$$

and  $G_s$  is the thermal conductance of the crystal beam.

We conduct the measurement at a range of global temperature  $T_{hs}$  from 20K to 320K, which can be precisely controlled via an external PID temperature controller. And the measurements are conducted with the device placed in a cryostat maintained at a vacuum level below  $1 \times 10^{-7}$  Torr, for which, we are able to ignore the effect of parasitic heat loss through thermal radiation and residual air molecules.

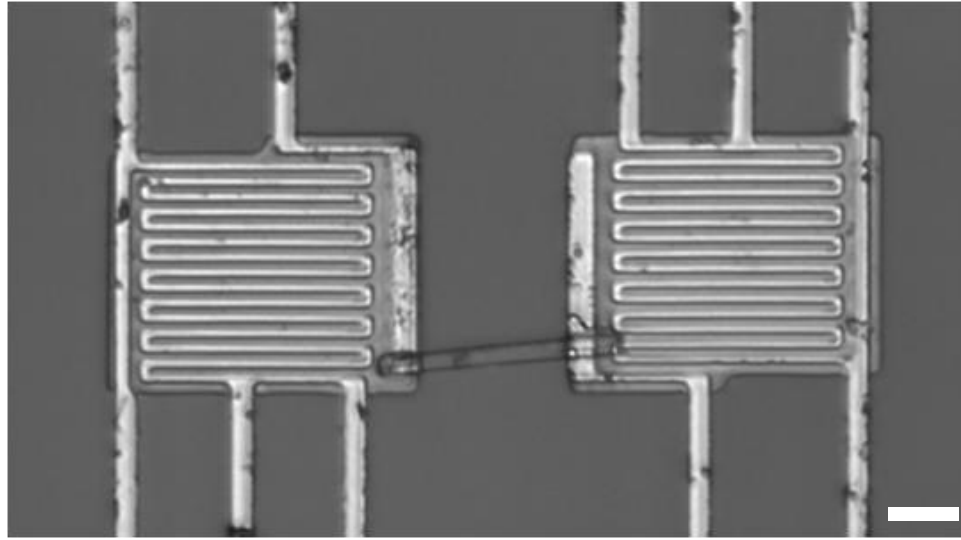


Figure 4-3 Optical image of a PSQ crystal fiber placed on a suspended micro device with built-in platinum resistance thermometers. The scale bar is 2mm.

#### **4.3.2 Precision placement of PSQ beam onto the thermal device**

There are a number of methods developed by previous researchers to precisely place nanowires, nanobelts and nanotubes onto the micro fabricated thermal devices. For example, a spin-on method is used to place Si nanowires,  $\text{SnO}_2$  nanobelts and other nanofilaments on the devices [151]. In this approach, the nanofilaments are first dispersed in isopropanol using sonication. A drop of the solution is then casted on the thermal devices. When the solvent finally dries, there are by chance some nanofilaments bridging

the suspended islands due to the surface tension of the solvent during the evaporation. Another method is based on the spin-on method and chemical vapor deposition (CVD). As the spin-on method, a drop of solution containing catalyst nanoparticles, such as Fe, Mo and  $\text{Al}_2\text{O}_3$  nanoparticles, is placed on the devices. The nanoparticles then distribute on the Pt pads on the two islands and serve as nucleate sites for the growth of nanofilaments such as single walled carbon nanotubes (SWCNTs) [40]. Due to the high temperature  $\sim 900^\circ\text{C}$  growth condition during CVD, the annealing effect usually leads to a very good thermal contact conductance.

Even though the spin-on method and the CVD growth method have a good yield of successful nanofilaments placement, yet, they both rely on sample dispersion in a solvent with sonication, particularly for the CVD growth method, a high temperature condition has to be applied. These two requirements, the dispersion of the nanofilaments and high annealing temperature forbid us to employ the aforementioned techniques for our PSQ crystals. There are two reasons, first, our PSQ crystals are organic-inorganic polymers, and most of solvents dissolve and therefore destroy them. Even with water used as solvent, PSQ crystals in micro beam forms tend to coagulate due to their low Zeta potential which stands for the electrokinetic potential in colloidal dispersions. This coagulate phenomenon can be easily observed once the PSQ crystals touch the water. As mentioned above, sonication is used to assist the dispersion of the nanofilaments in the liquids, however, due to the low Young's modulus of the polymeric materials, the PSQ crystals are easily broken to pieces once the sonication is applied. As a result of the low melting temperature  $<400^\circ\text{C}$  and the synthesis method, apparently, the CVD high temperature growth method is excluded for our research.

Considering the impractical aspects of the spin-on and CVD growth methods, we adopt the tip manipulation method to precisely place the PSQ crystal beams on the thermal devices. With this method, people have attached individual multi-walled carbon nanotubes (MWCNT) on a AFM tip and placed the MWCNT on the thermal device for thermal transport measurements [6], [154]. In our research, the PSQ crystal beams are much larger than the MWCNT. We use a tungsten tip with bigger tip diameter  $\sim 1\mu\text{m}$  to place the PSQ crystal beams onto the thermal device. And the tungsten tip is connected to a high precision motorized micromanipulator.

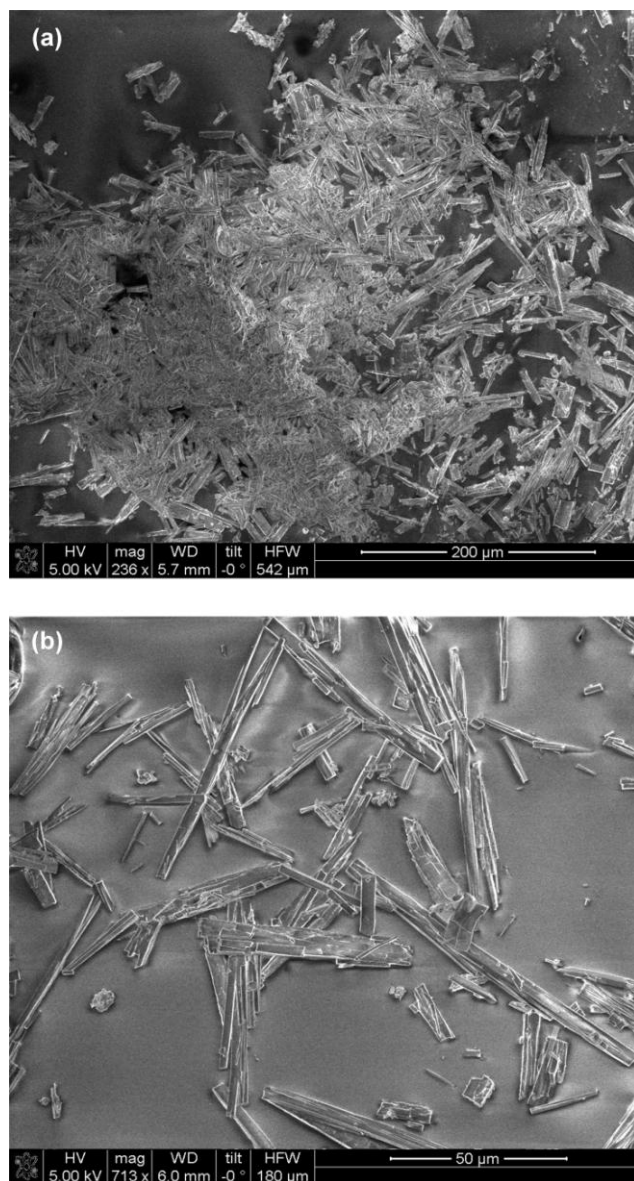


Figure 4-4 (a) A SEM image PSQ cluster after a sol-gel process. Water produced during the condensation pulls the PSQ crystal beams together due to a strong surface tension. (b) PSQ crystal beams separated by sliding a glass substrate on top of the PSQ cluster.

Due to a sol-gel process for the synthesis of the PSQ beams, water is formed during the one-step condensation of two hydrolyzed monomers [21]. As a result, the PSQ crystals are usually clustered together as shown in figure 4-4(a). Therefore, before we perform the

tip manipulation, The PSQ cluster must be separated, so that we can manipulate a single PSQ beam. To separate the PSQ cluster, we first put a PSQ cluster about 1~2mm in diameter on a glass slide and then use another slide to rub against the PSQ cluster. We have tried several substrates for the separation of the PSQ cluster, for example metals (aluminum foil and gold coated silicon substrate), polydimethylsiloxane (PDMS), a bare silicon substrate, a silicon substrate with 95nm thermally grown silicon dioxide and the glass slide. We find the silicon substrate with silicon dioxide and the glass slide has a better separation than the other substrates. The separated PSQ beams are shown in figure 4-4(b). This is because of water induced surface tension between smooth PSQ crystal surfaces and silicon dioxide, and hydrogen bonding formed at the interface due to highly electronegative atoms within the hydroxyl groups on the glass substrate [155].

Even though the strong adhesion force enables the isolation of the PSQ crystals, however, this imposes a further difficulty on lifting the individual PSQ crystal from the glass substrate. Therefore, after the separation step, we conduct an annealing process at a temperature about 50~60°C in 10 minutes. The temperature is well below the glass transition temperature of the PSQ crystal which is around 300~400°C. The purpose of this annealing process is to remove the water residual, and consequently reduce the surface tension. Furthermore, the raised temperature condition induces a small thermal expansion mismatch between the PSQ beam and the glass substrate, which further breaks the hydrogen bonds at the interface. After the annealing process, the PSQ beams can be easily picked up by the tungsten tip due to the van der Waals force. In order to have a good mechanical adhesion and a good thermal contact performance between the Pt pads and the PSQ beams, we first use the tungsten tip to apply a thin layer of silver epoxy on

the Pt pads, and then place the PSQ beam on the thermal device. After about 5 minutes curing time, the PSQ beam is strongly adhered to the thermal device for further thermal characterization.

### 4.3.3 Thermal conductivity measurement results and discussion

As reported elsewhere [156], the background heat transfer between the heating and sensing islands introduces errors and result in an overestimate of the thermal conductance of the PSQ beam. Inspired by previous works, we conduct a control experiment with an empty device under the same measurement conditions as we measure the PSQ beams. However, no noticeable signals are observed from the sensing island. This can be attributed to two reasons: 1) the super high vacuum assures an extremely low concentration of residual gas molecules. 2) The devices used in these measurements have rather large separation gap between the two islands which is at least 15 $\mu$ m. As we know the view factor of thermal radiation is inversely proportional to the squared distance between the two objects, therefore, the thermal radiation across the two islands is negligible, especially compared with a typical thermal conductance of 3.5 $\times 10^{-8}$ W/K at room temperature. We also consider the heat loss on PSQ beam due to thermal radiation to the surrounding. If we ignore the thermal radiation from the surface of the PSQ beam, a relative error below is introduced in the thermal conductivity calculation [157]:

$$\Delta = mL_s \coth (mL_s) - 1, \quad (4.2)$$

where  $m = \sqrt{8\epsilon\sigma T_{hs}^3(w+t)/k_s w t}$ ,  $\epsilon$ ,  $\sigma$ ,  $T_{hs}$  and  $k_s$  are emissivity of the PSQ beam, the Stefan-Boltzmann constant, global temperature, and thermal conductivity of the PSQ



beam, and  $w$  and  $t$  are the width and thickness of the PSQ beam. For a typical PSQ beam measure in our experiment,  $w=2.8\mu\text{m}$ ,  $t=1.04\mu\text{m}$ ,  $L_s=16\mu\text{m}$ , and let  $\epsilon=0.3$ , the relative error  $\Delta$  for ignoring the thermal radiation loss is found to be as small as 0.1%.

Consideration of the thermal contact resistance is of great importance in order to determine the PSQ thermal conductivity accurately. The total thermal resistance  $R_{tot}$ , the sample thermal resistance  $R_s$ , and the thermal contact resistance  $R_c$  satisfy the following equation:

$$R_{tot} = R_s + R_c = \frac{L_s}{k_s A_{cr}} + \frac{1}{R_c'' A_c}, \quad (4.3)$$

where  $R_c''$  is interface thermal resistance per unit area, and  $A_c$  is the contact area between the PSQ crystal beam and the Pt pads on both islands. To evaluate the thermal contact resistance, we plot the measured total thermal resistance  $R_{tot}$  versus  $L_s/A_{cr}$  of 5 different samples at global temperatures  $T_{hs}=50\text{K}$  and  $300\text{K}$  as shown in figure 4-5(a). At each temperature  $R_{tot}$  is in linear relationship with  $L_s/A_{cr}$ , and the extrapolations of the fitted lines are  $-0.321 \times 10^7 \text{K/W}$  and  $-0.89 \times 10^7 \text{K/W}$ , which are negligible compared to  $R_{tot}$ . Therefore, the thermal contact resistance ( $R_c$ ) between PSQ crystal beams and the Pt Pads can be ignored. Equation 4.3 can be reduced to  $R_{tot} \approx R_s$ , which can then be used to extract the thermal conductivity measurement of the PSQ beams.

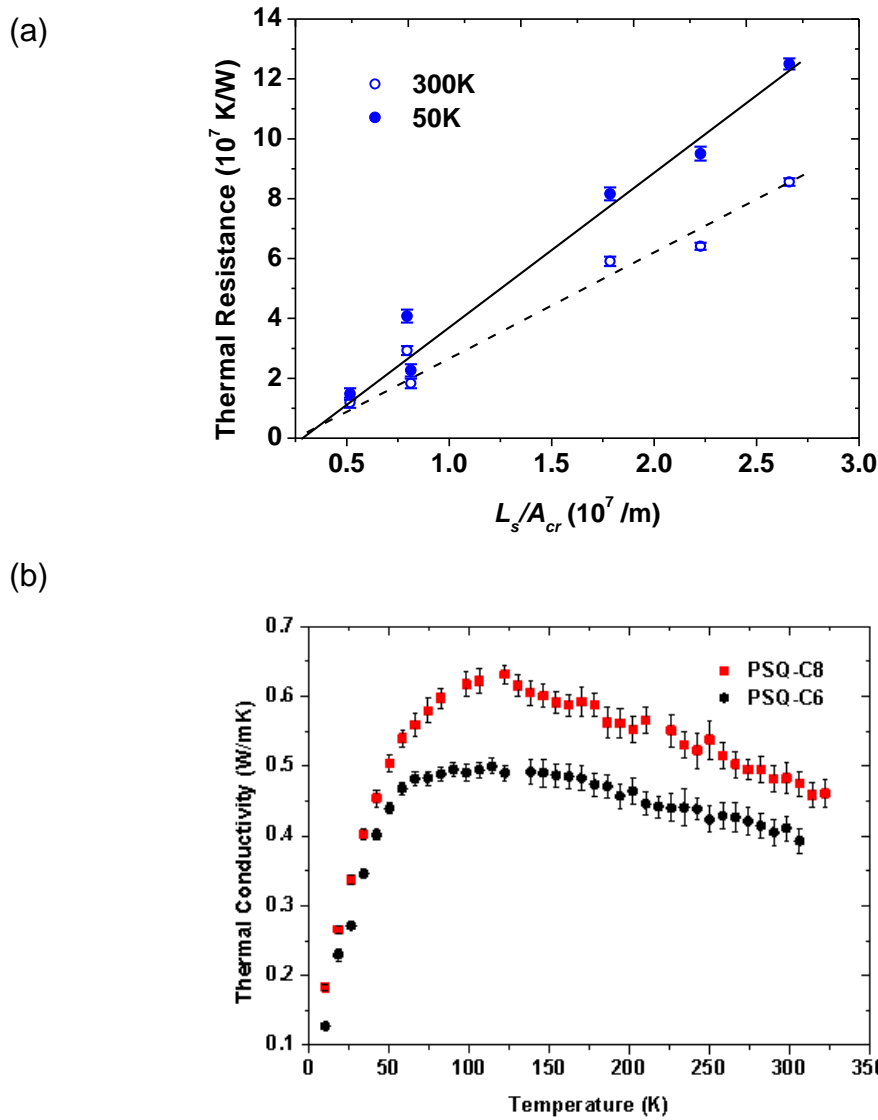


Figure 4-5 (a) The total thermal resistance measured versus  $L_s/A_{cr}$  in 5 samples at 50K and 300K. (b) Thermal conductivity of both type PSQ fibers at temperatures from 10K to 320K.

Figure 4-5(b) shows the typical thermal conductivities of octylene-bridged and hexylene-bridged PSQ beams in the temperature range from 10K to 320K. The thermal conductivity of octylene-bridged PSQ beams is generally larger than that of hexylene-

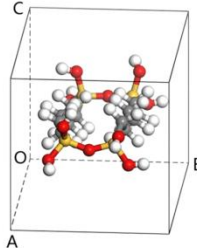
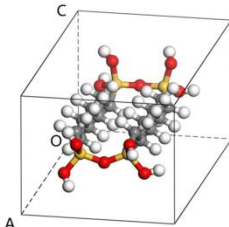
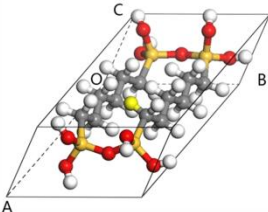
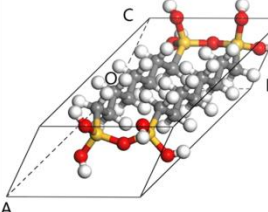
bridged PSQ beams, which can be explained by a lower concentration of hydrogen bonds due to a longer octane chain in octylene-bridged PSQ microbeams. The thermal transport in both octylene-bridged and hexylene-bridged PSQ beams clearly exhibits crystal like behaviors. At the temperatures larger than 150K, the measured thermal conductivities decrease with increasing temperature. This is a signature of the anharmonic Umklapp scattering of phonons in crystals at high temperatures. The temperature dependent thermal conductivity of common high-purity crystals, such as, Si [158] and GaAs [159], generally follows the power law  $T^{-1}$  due to the increase in phonon density. However, for both octylene-bridged and hexylene-bridged PSQ crystals, the thermal conductivity is proportional to  $T^{-0.5}$  at temperatures larger than 250 K.

#### **4.4 Non-equilibrium molecular dynamics simulations of PSQ thermal conductivities**

To understand the thermal transport in PSQ hybrid crystals, we conduct Non-equilibrium molecular dynamics (NEMD) simulations [29], [160]–[163] to calculate the thermal conductivities of octylene-bridged and hexylene-bridged PSQ beams. The repeating units of both octylene-bridged and hexylene-bridged PSQ beams are first constructed and put in an orthogonal unit cell with periodic boundary conditions in all directions (Table 4-1). Condensed-phase Optimized Molecular Potentials for Atomistic Simulation Studies (COMPASS) exported from Material Studio 6 are used to model the molecules [164]. The molecular structures and the unit cells are optimized using multiple algorithms, including Steepest Descent, Conjugate Gradient, and Newton minimization (Smart Minimizer, Discover module of Material Studio 6, Accelrys Inc.). With the minimized

structures and unit cells, simulation supercells are obtained by duplicating the unit cell along all three lattice vectors.

Table 4-1 Initial structure and optimized structure for C6 and C8

	PSQ-C6	PSQ-C8
Initial Unit Cell	 $a = 15.00$ $b = 10.00$ $c = 10.00$ $\alpha = 90.00$ $\beta = 90.00$ $\gamma = 90.00$	 $a = 18.00$ $b = 10.00$ $c = 8.00$ $\alpha = 90.00$ $\beta = 90.00$ $\gamma = 90.00$
Optimized Unit Cell	 $a = 14.29$ $b = 7.78$ $c = 5.06$ $\alpha = 60.99$ $\beta = 89.59$ $\gamma = 96.14$	 $a = 18.82$ $b = 7.82$ $c = 5.03$ $\alpha = 61.02$ $\beta = 90.31$ $\gamma = 97.29$
Constructed Super Cell	35 x OA 4 x OB 6 x OC	30 x OA 4 x OB 6 x OC

- $a = OA, b = OB, c = OC$
- $\alpha = \angle BOC, \beta = \angle COA, \gamma = \angle AOB$

Figure 4-6 shows a representative setup and temperature profile of NEMD. In these simulations, a temperature gradient is created and maintained by using Langevin thermostats controlling the temperatures of the two ends of the simulation domain (figure 4-6). The temperatures of the heat sink and heat source regions are set to 15K lower and higher than the average system temperature, respectively. After steady state is reached, temperature gradient ( $dT/dx$ ) is obtained by fitting the linear portion of the temperature profile, and heat flux can be calculated using  $J = dQ/dt/S$ , where  $dQ/dt$  is the average energy change rates of the two Langevin thermostats, and  $S$  is the cross sectional area.

The thermal conductivity is then calculated by Fourier's law,  $\kappa = -J/(dT/dx)$ . For each simulation, four thermal conductivity values are calculated for different time blocks in the steady state, and the final value is the average of them with the error bar being the standard deviation.

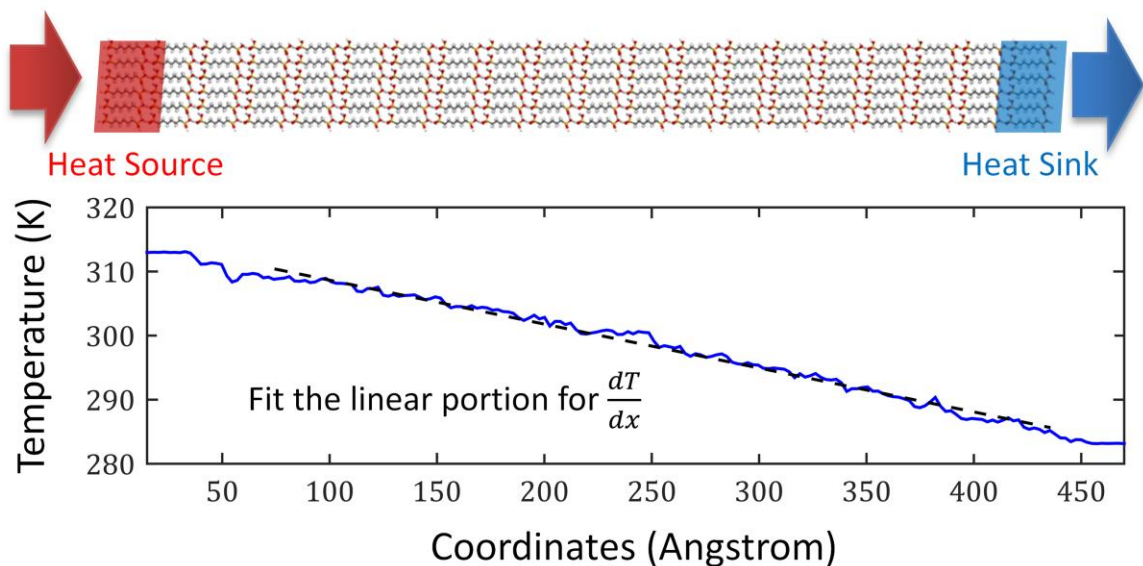


Figure 4-6 A Representative NEMD Setup for Thermal Conductivity Calculation

The PSQ beams are first relaxed at 300K and 1 atmosphere pressure for 1ns in the constant temperature and constant pressure (NPT) ensemble. We then fix the volume and run the simulations in the constant number of atoms, volume and energy ensemble (NVE) to calculate the thermal conductivities using NEMD. Thermal conductivity of three different types of PSQ beams is calculated at 300K, and they are tabulated in Table 4-2.

Table 4-2 Thermal conductivity of PSQ beams with different molecular backbone lengths at 300K

Beam type	Thermal conductivity (W/mK)
PSQ-C8	$1.39 \pm 0.09$
PSQ-C6	$1.21 \pm 0.03$
PSQ-C4	$0.31 \pm 0.04$

It is known that thermal transport within one molecule is very efficient due to the well-ordered atomic structure and strong covalent bonds [165]–[167]. The thermal transport from one molecule to another in the along-beam direction relies on hydrogen bonds. These hydrogen bonds are much weaker than the intrachain covalent bonds, and thus the interfaces work as a bottleneck for thermal transport along the beam. When beams are formed by longer molecules aligning head to tail, the interface density decreases, and thus the effective thermal conductivity of the beam will be higher than that of beam formed by shorter molecules.

Due to the periodic arrangement of the molecular chains in the chain length direction, the formation of phonons that has coherent length longer than the length of a molecule may happen. These phonons see the beams as homogenous materials and can travel distances much longer than the length of one molecule. Such a phenomenon is similar to that seen in superlattices [168]. To show that such phonons can exist in the PSQ beams due to the periodic structure in the beam, PSQ-C6 beams are simulated with different supercell

lengths (figure 4-7(a)). The increasing trend of the thermal conductivity with respect to the beam length shows that thermal conductivity is influenced by the classical size effect: the mean free paths of phonons are limited by the length of the sample. Such an increasing trend is only possible when the system contains phonons with mean free paths larger than the sample length. This means that not all phonons are scattered at the hydrogen interfaces but some of them can travel for much longer distances. These phonons will mainly subject to anharmonic scattering. As the system temperature increase, anharmonic scattering will lower the thermal conductivity (figure 4-7(b)). This should lead to a  $1/T$  relation in the thermal conductivity.

However, there are still some short wavelength phonon modes that are scattered at the hydrogen interfaces. It is known that the interfacial thermal transport can be enhanced at higher temperatures due to more anharmonic transport channels being excited [169], this is especially true for our case in which the interfaces are connected by relative weak hydrogen bonds which are much more anharmonic than stronger covalent bonds. The above-mentioned two competing effects (i.e., anharmonic phonon scattering and interfacial anharmonic coupling effects) are probably responsible to the experimentally observed  $T^{-0.5}$  relation at high temperatures (figure 4-7(c)). It is worth noting that the MD simulation results do not follow the  $T^{-0.5}$  over the whole temperature range. This may attribute to the accuracy of potential used and the error in the thermal conductivity data. Nevertheless, MD simulations qualitatively predict the decreasing trend of thermal conductivity and the data from 250 to 350K agrees reasonable with the  $T^{-0.5}$ .

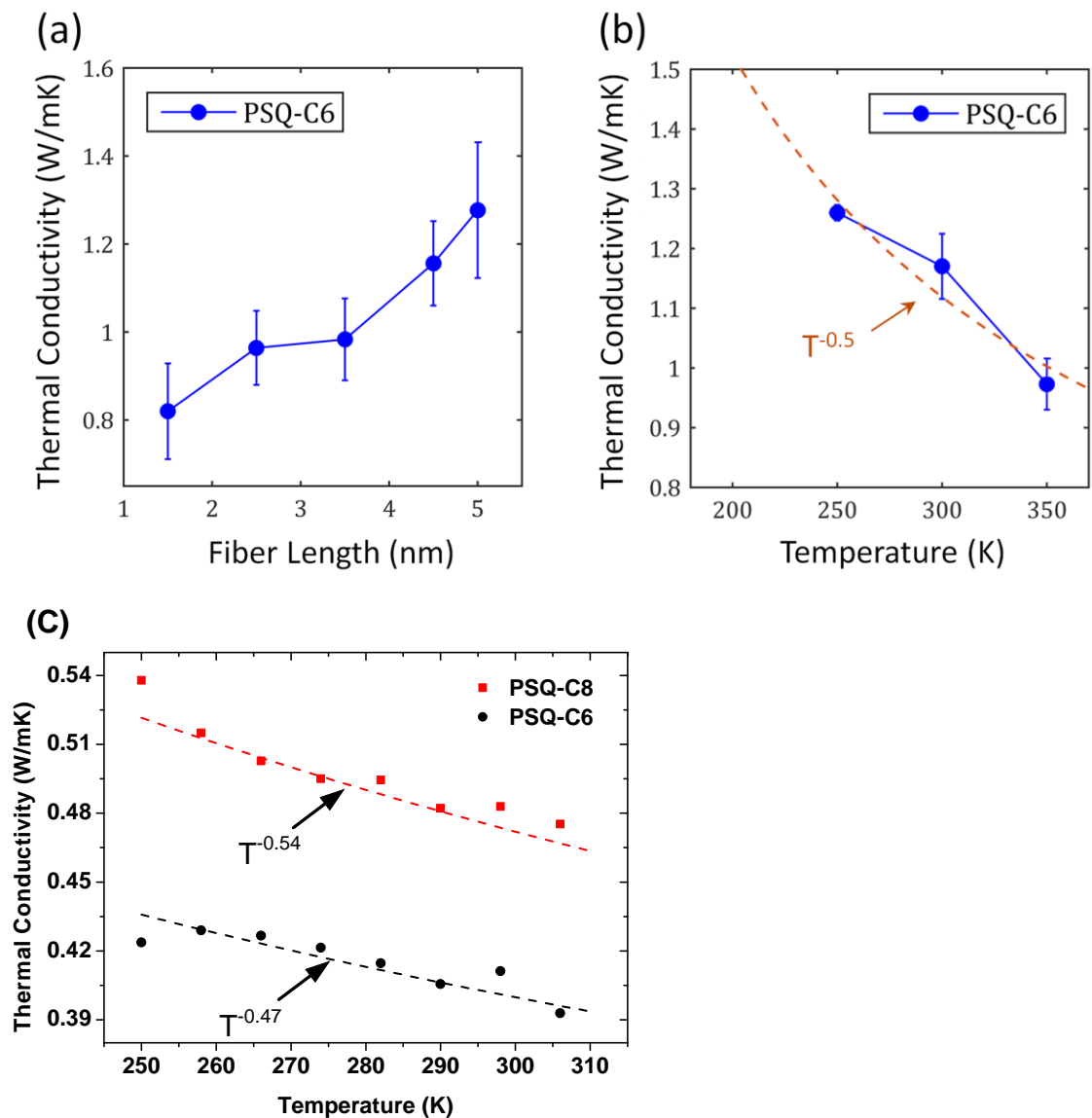


Figure 4-7 (a) Thermal conductivity of PSQ-C6 as a function of the beam Length. (b) Thermal conductivity of PSQ-C6 from 200K to 400K. (c) Measured thermal conductivities of PSQ-C6 and PSQ-C8 in the temperature range from 250K to 310K.

## 4.5 Conclusion

In summary, a so-gel process with two precursors is adopted to produce the octylene- and hexylene bridged PSQ crystalline beams. Both the infrared spectroscopy and x-ray



diffraction pattern indicate that the hydrogen bond linked PSQ crystal structures have high crystallinity (~89%). We measured the thermal conductivity of hydrogen bond based PSQ beams. The thermal conductivity of the Octylene-bridged PSQ beams is measured to be higher than the hexylene-bridged ones. The thermal conductivities for both types of beams increase at low temperatures while decreasing at high temperatures, which is attributed to the Umklapp scattering of phonons exist in high-purity crystals. The NEMD simulations reveal that the thermal transport in PSQ crystals displays both coherent phonon transport behavior and interfacial thermal transport feature. The experimental and simulation results in this work clearly demonstrate the tunable and crystal-like thermal transport in PSQ hybrid polymer crystals, which paves the way of practical thermal applications for polymer crystals.

## CHAPTER 5. Thermal conductivity of individual crystalline polyethylene (PE) nanofibers

### 5.1 Introduction

Crystalline polyethylene (PE) nanofibers have been demonstrated with Young's modulus of  $\sim 312$  GPa [170], which approaches the theoretical limit [24]. Also, for ultradrawn single crystal mat [15], it has been experimentally proved that, the axial Young's modulus along the molecular chain direction is approximately in linear relationship with its thermal conductivity, and the measured maximum thermal conductivity reaches a value of  $\sim 41.8$  W/mK with a corresponding Young's modulus about 250 GPa at a temperature of 295K. The linear relationship can be explained by the crystallinity and crystallite orientation within the ultradrawn material. The PE nanofibers produced by the two-stage drawing method is believed to possess a similar level of crystallinity and lamellar orientation as discussed in Chapter 3. Accordingly, from the linear proportionality between the Young's modulus and the thermal conductivity, we expect the thermal conductivity of our PE nanofibers reach a value at least 58 W/mK.

Recently, with the development of highly reliable and accurate thermal measurement techniques, great interests have been revived on the characterization of thermal transport in polymer fibers with high moduli. For example, time domain thermoreflectance (TDTR) is applied to measure the axial thermal conductivity of a commercially available PE microfiber (Dyneema®) [27]. The TDTR technique yields a temperature dependent thermal conductivity with its maximum around 100K, and the room temperature value is  $\sim 18$  W/mK. However, in this work, the measured PE fibers have diameters around  $20\mu\text{m}$

and the spot size of the laser used in the system is about  $5.4\mu\text{m}$  in diameter. As a result, we are not able to perform the measurements using the TDTR technique on our PE nanofibers. While on the contrary, a bi-cantilever technique has been developed and successfully measured a thermal conductivity of  $104\text{W/mK}$  for a PE nanofiber ( $131\text{nm}$  in diameter,  $290\mu\text{m}$  in length) at room temperature [31]. Nevertheless, a particular problem associated with this technique is low signal to noise ratio which greatly degrades the accuracy of the results. Furthermore, due to experimental limitations, the temperature dependence of the thermal conductivity is not yet determined for the PE nanofibers. In this chapter, we measure the thermal conductivities of PE nanofibers over a temperature range of  $20\text{K}$  to  $320\text{K}$ , by implementing a micro device with suspended structures where the nanofiber can be placed. This method has been used to measure nanofibrils of various materials and proven with great reliability and precision [98], [156], [171], [172].

## **5.2 Sample preparation and measurement scheme**

The detailed measurement scheme has been discussed in Chapter 2, Section 3. Briefly, as shown in figure 5-1, a PE fiber is placed on the two heating and sensing islands by a manipulator. To examine the thermal transport at the interface between the fiber and islands, we apply a small drop of cyanoacrylate based super glue or deposit platinum (Pt) at each end of the fiber to fix it on the islands. At a global temperature, one island is heated by passing a DC current through the platinum coil. The heat generated on the coil due to the Joule effect is then dissipated to the ambience via the PE nanofiber and the supporting legs. When the heat transfer reaches a steady state, a constant temperature difference  $\Delta T$  is established across the PE nanofiber. By knowing the temperature coefficient of resistance of each Pt coil, we are able to deduce the absolute temperature of

each island after measuring the resistance of each coil with Lockin amplifiers, and therefore the temperature difference  $\Delta T$  can be found. Together with the knowledge of the heat transferred through the nanofiber and the dimensions, we then obtain the thermal conductivity of the nanofiber by applying the Fourier's law.

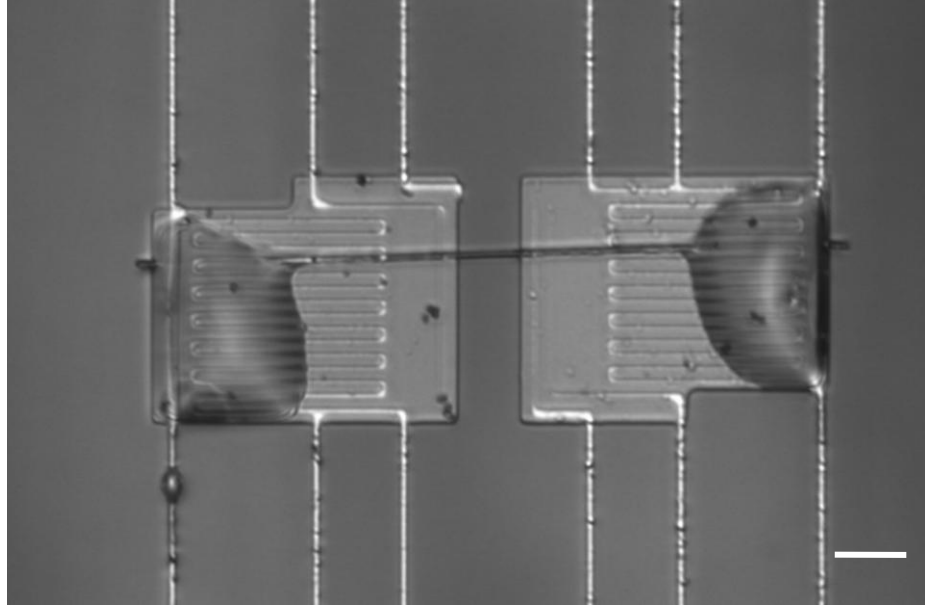


Figure 5-1 A PE nanofiber placed on the micro device with suspended islands and legs. The nanofiber is clamped at both ends with cyanoacrylate based super glue. The scale bar is 10  $\mu\text{m}$ .

### 5.3 Experiment results and discussion

As mentioned in Chapter 2, Section 3, the effective thermal conductivity  $k_{eff}$  is equal to the intrinsic thermal conductivity  $k_s$  of the sample only if the thermal contact resistance can be ignored. This condition is particularly important because the thermal conductivity of PE is very high with a previously reported value of 104W/mK at room temperature.

An equivalent thermal circuit in figure 5-2 can be used to represent the steady state thermal transfer during the measurements:

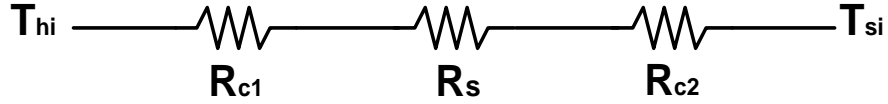


Figure 5-2 Thermal resistance network for steady state heat transfer on the micro device with a PE fiber incorporated.  $R_{c1}$  is the thermal contact resistance between the nanofiber and the heating island,  $R_{c2}$  is the thermal contact resistance between the nanofiber and the sensing island, and  $R_s$  is the thermal resistance of the measured nanofiber.

Following figure 5-2, we can write the total thermal resistance  $R_{tot}$  as following:

$$R_{tot} = R_{c1} + R_s + R_{c2}, \quad (5.1)$$

because the contact conditions on both islands are very similar in terms of the geometry of the contacts and the amount of super glue applied, we can assume  $R_{c1} \approx R_{c2}$ . By knowing the length  $l$  of the nanofiber suspended over the gap and the diameter  $d$ , equation 5.1 can be written as:

$$R_{tot} = 2R_{c1} + \frac{l}{k_s A} = 2R_{c1} + \frac{4l}{k_s \pi d^2}, \quad (5.2)$$

where  $k_s$ , and  $A$  are the thermal conductivity and the cross area of the PE nanofiber respectively. And we can also write  $R_{tot}$  as:

$$R_{tot} = \frac{4l}{k_{eff} \pi d^2}, \quad (5.3)$$

substitute equation 5.3 for  $R_{tot}$  in equation 5.2, we have:

$$\frac{4l}{k_{eff} \pi d^2} = 2R_{c1} + \frac{4l}{k_s \pi d^2}. \quad (5.4)$$

Rearrange equation 5.4 the effective resistance  $k_{eff}$  is related with  $k_s$  as following:

$$k_{eff} = \left( \frac{1}{2R_{c1} / R_s + 1} \right) k_s. \quad (5.5)$$

From equation 5.5, we notice that only if  $R_{c1} \ll R_s$ ,  $k_{eff} \approx k_s$ . For nanofibers which are sufficiently long and small in diameter, this condition normally applies if thermal conductivity of measured samples is very small (e.g.  $\sim 1\text{W/k}$ ) [100], [156]. We examine the heat transfer of the nanofiber with three bonding methods: 1. The nanofiber is placed on the islands and only line contacts form with no additional bonding materials. 2. Cyanoacrylate based glue is applied to bond the nanofibers on the islands. 3. A layer of platinum is deposited around the nanofiber on the islands.

### 5.3.1 Thermal contact resistance between the nanofiber and the islands without adhesion materials

If a PE nanofiber is placed on the micro device, temperature of the nanofiber portion in contact with the island varies along the fiber length, this portion of the nanofiber can be treated as a fin, and therefore the total thermal contact resistance  $R_c$  between the nanofiber and two islands is [173]:

$$R_c = \frac{2}{\sqrt{\frac{k_{\parallel} \pi d^2}{4 R_c'} \tanh \left( l_c \sqrt{\frac{4}{k_{\parallel} \pi d^2 R_c'}} \right)}}, \quad (5.6)$$

where  $k_{\parallel}$  is the longitudinal thermal conductivity of the nanofiber,  $d$  is the nanofiber diameter,  $l_c$  is the length of the nanofiber contacting the islands, and  $R_c'$  is the thermal resistance of a unit contact length between a cylinder and a flat surface [174]. To calculate  $R_c'$ , we follow McGee et al.'s line contact model [174], [175]:

$$R_c' = \frac{1}{\pi k_{\perp}} \ln \left( \frac{2d}{b} \right) - \frac{1}{k_{\perp}} + \frac{1}{\pi k_{Pt}} \ln \left( \frac{d}{\pi b} \right), \quad (5.7)$$

where  $k_{\perp}$  is the transverse thermal conductivity of PE crystal about 0.2W/mK at room temperature [34],  $k_{Pt}$  is the thermal conductivity of Pt which is about 71W/mK, and  $b$  is the half line contact width of the nanofiber in the perpendicular direction of the nanofiber.

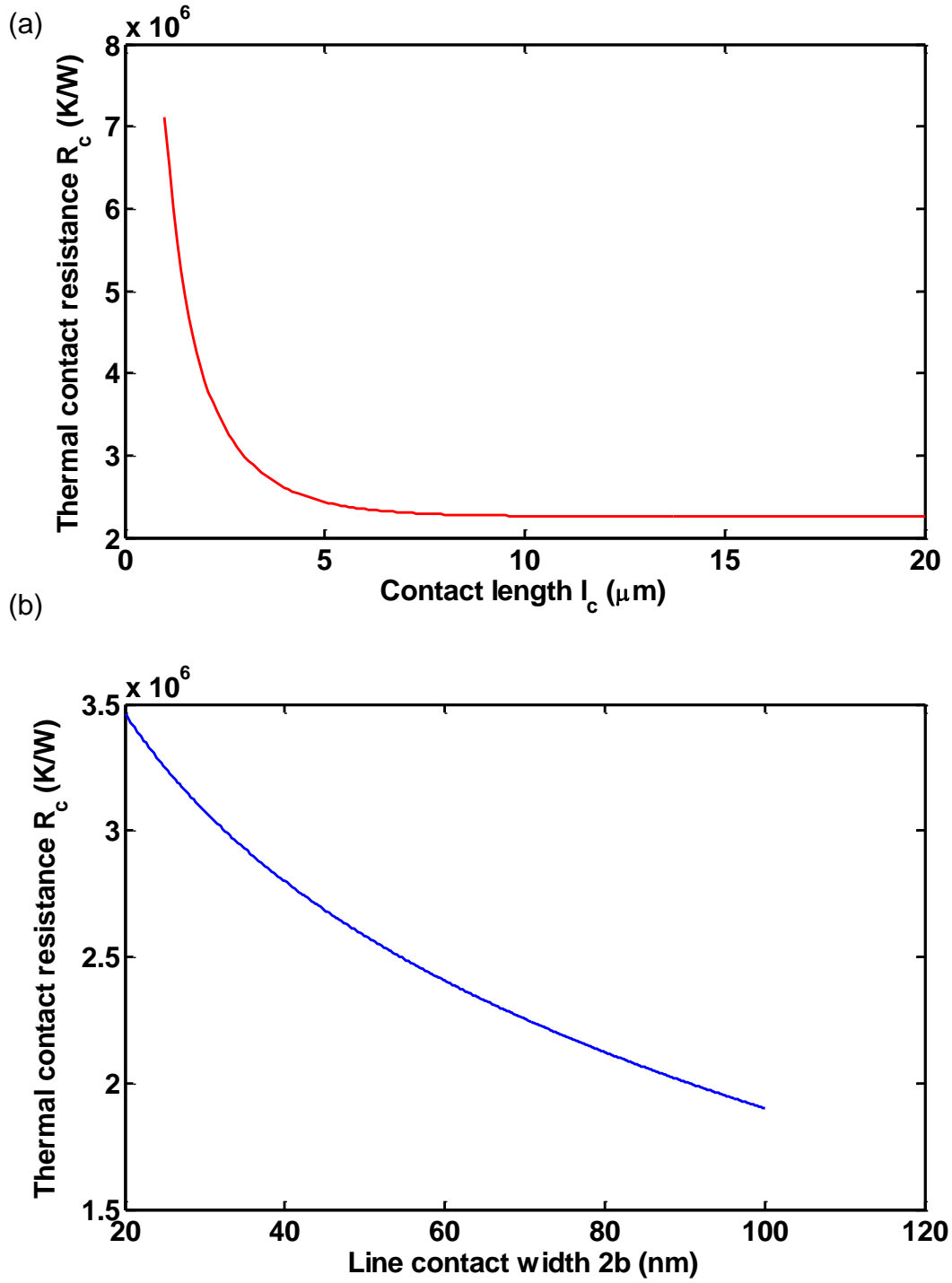


Figure 5-3 Total thermal contact resistance plot against contact length  $l_c$  (a) and the line contact width  $2b$  (b) based on equation 5.1 and 5.2.



For a nanofiber with diameter about 441nm, based on equation 5.1 and 5.2, the calculated total thermal contact resistance is plotted in figure 5-3. As shown in figure 5-3(a), the total thermal contact resistance decreases as the contact length increases, and asymptotically approaches  $2.26 \times 10^6$  K/W. Figure 5-3(b) also shows a decreasing trend of the total thermal contact resistance with respect to the line contact width. However, the line contact width of a nanofiber is normally considered very small as a result of a small deformation caused by weak van der Waals force [173]. For a PE nanofiber 441nm in diameter and 24.29 $\mu$ m in length, if the thermal conductivity is assumed to be 20W/mK at room temperature, the intrinsic thermal resistance of the fiber is  $9 \times 10^6$  K/W which is only about 4 times as big as the total contact resistance. Additionally, in reality, the thermal contact is never ideal, gaps, contaminations and other defects all contribute to a much larger thermal contact resistance than the ideal case. Thermal conductivities of a PE fiber with a diameter of 441nm and a length of 24.29 $\mu$ m is measured and shown in figure 5-4.

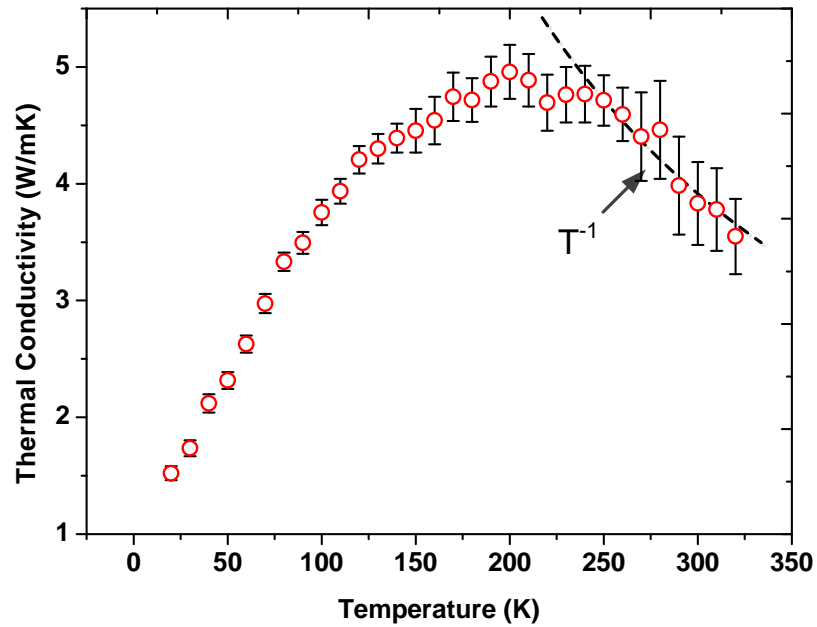


Figure 5-4 Thermal conductivities of a PE nanofiber placed on the thermal device with no additional bonding materials.

### **5.3.2 PE nanofibers clamped with cyanoacrylate super glue**

Based on the discussion in the last section, we decide to apply cyanoacrylate super glue in an attempt to reduce the thermal contact resistance. After the sample gluing on the micro device, we then attach the device onto a ceramic package and connect the device with the ceramic package using gold wires. The assembled ceramic package is placed in a cryostat with a vacuum level as high as  $1 \times 10^{-7}$  Torr. We measure the thermal conductivity of PE nanofibers from 20K to 320K with a temperature interval of 10K.

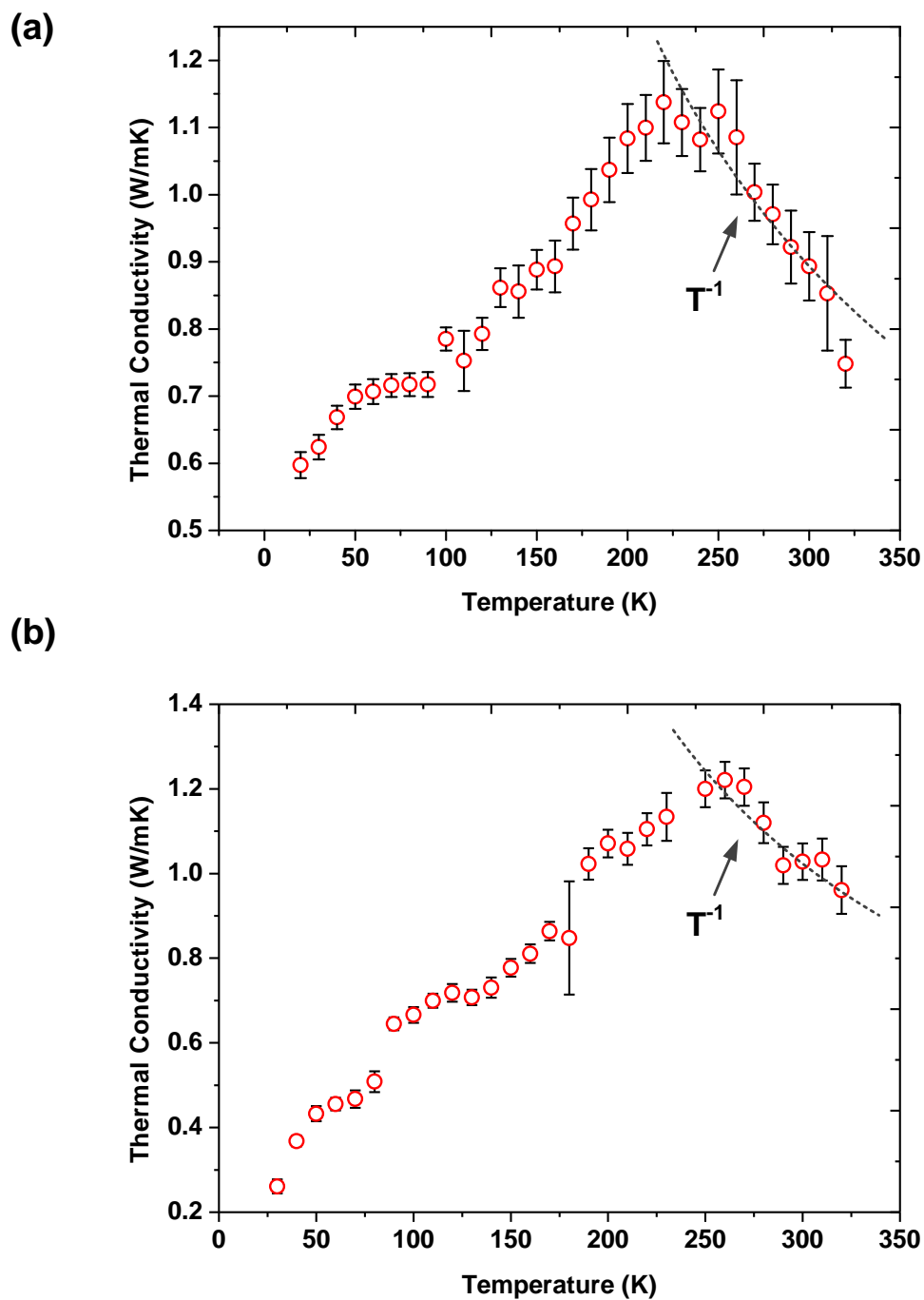


Figure 5-5 Measured thermal conductivities for two samples clamped by super glue, sample 1(a), and sample 2(a).

Four samples have been measured with the conditions mentioned above. For two typical PE nanofibers, figure 5-5 illustrates the thermal conductivity increases with temperature at a low temperature range and decreases at a high temperature range, although the temperature range is slightly different. Sample 1 has a maximum thermal conductivity at 210K, while sample 2 has the maximum at 260K. At the low temperature range, the increasing trend can be explained by the increasing heat capacity due to more excited phonon modes at higher temperature. From figure 5-5, we can also observe that the thermal conductivities of both samples show an approximately inverse proportionality with respect to temperature. The trend is a signature of phonon-phonon scattering in a crystalline solid [34], [47].

However, the effective thermal conductivity of the fibers is significantly lower than what was reported in previous research, especially a thermal conductivity value of 104W/mK for the PE nanofibers which was fabricated with the same method [31]. The measured low effective thermal conductivity is mainly caused by the thermal contact resistance  $R_c$ . As mentioned in the beginning of the section, to meet the requirement of  $R_c \ll R_s$ ,  $k_{eff} \approx ks$ , thermal conductivity of measured samples is normally very small ~1W/mK. However, the thermal conductivity of highly crystalline PE nanofibers is on the order of 20W/mK [27], [31]. For a PE nanofiber with length 5.6  $\mu\text{m}$  and diameter 0.991 $\mu\text{m}$  as measured in figure 5-5(a), assume the thermal conductivity is 20W/mK at room temperature, the thermal resistance  $R_s$  is  $3.6 \times 10^5 \text{K/W}$ . However, the total thermal resistance  $R_{tot}$  measured is  $8.11 \times 10^6 \text{K/W}$  which is much larger than  $R_s$ , which is highly likely caused by a thick layer of glue below the nanofiber.

### 5.3.3 PE nanofibers clamped by focus ion beam (FIB) assisted platinum deposition

Pt deposition by FIB has been used to precisely bond micro/nano filaments onto substrates, because of the high resolution ( $\sim 7\text{nm}$ ) of the ion beam, and the technique can usually achieve a  $50\text{nm}$  minimum deposited line width. The resultant bonds can normally enhance the thermal and electrical conductance between the samples and the substrates [173], [176] due to the inherently high thermal and electric conductivities of the Pt metal. Therefore, to reduce the thermal contact resistance between the PE nanofibers and the heating/sensing islands, A FEI NOVA 600 dual beam system is used to deposit the Pt on the PE nanofibers. During the process, a gas injection system precisely delivers a liquid organometallic precursor (Trimethyl(methylcyclopentadienyl)Platinum(IV) ( $\text{C}_9\text{H}_{16}\text{Pt}$ )) at a location very near the surface of the sample. The high energy gallium ions (accelerating voltage  $30\text{kV}$ , current  $10\text{pA}$ ) from a liquid-metal ion source separate the organic groups and the metal ions. The organic groups as a volatile part are evacuated from the chamber, and the Pt ions acquire electrons and therefore deposit on the bonding areas. The resulting bonds are illustrated in figure 5-6.

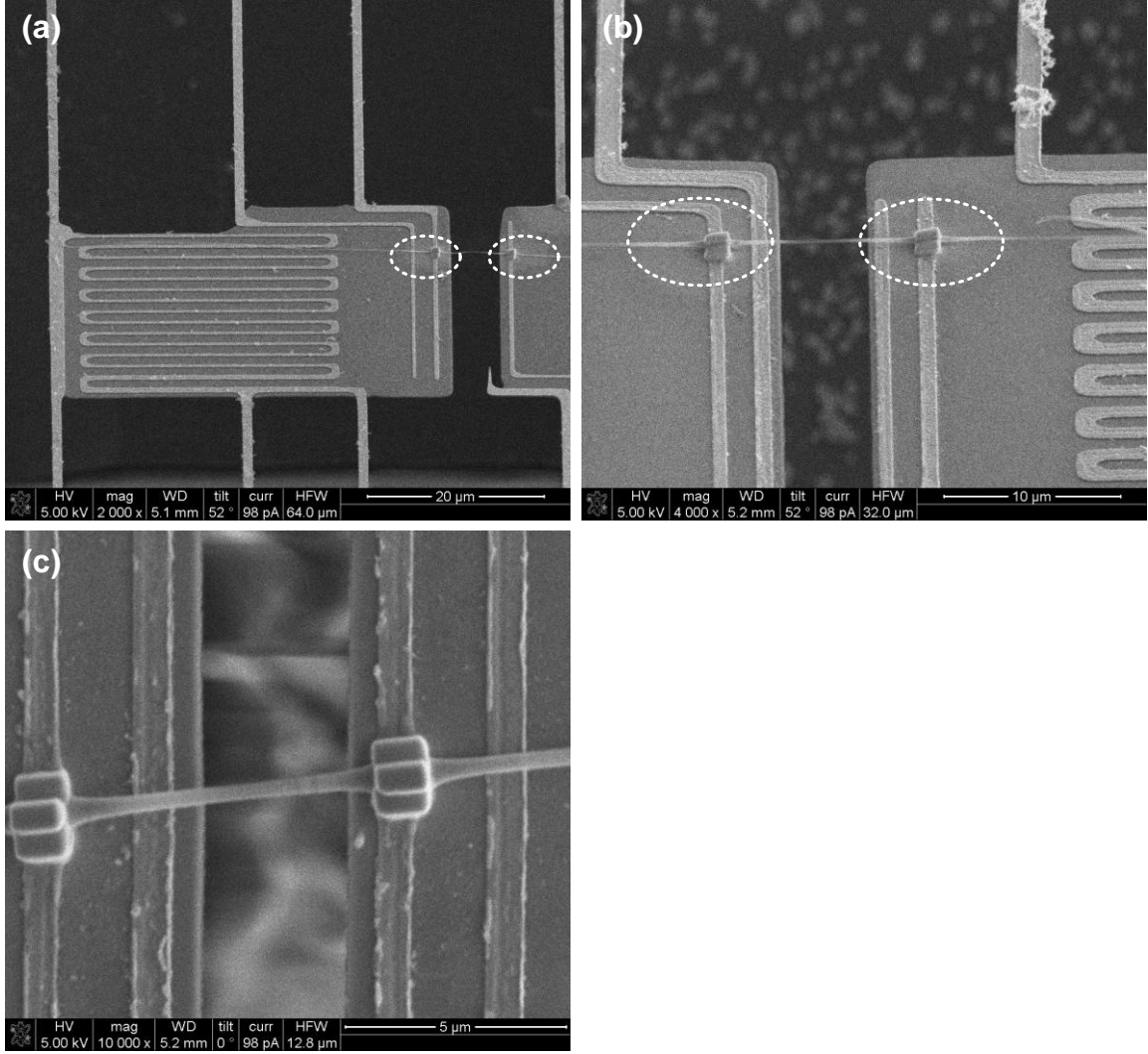


Figure 5-6 (a) and (b) are two typical samples bonded with FIB assisted Pt deposition; the circled areas are contaminated by the Pt atoms. (c) A close look of a PE nanofiber clamped on the islands by Pt blocks.

As shown in figure 5-6, we have successfully bonded the PE nanofibers on the islands. To reduce the potential damage from the electron beam and the ion beam, we use a very low accelerating voltage of 5kV and a beam current of 98pA to image the bonded samples. The dose during SEM imaging is about  $160\mu\text{C}/\text{cm}^2$  which is two orders of

magnitude smaller than critical dose for the destruction of the electron diffraction pattern [177].

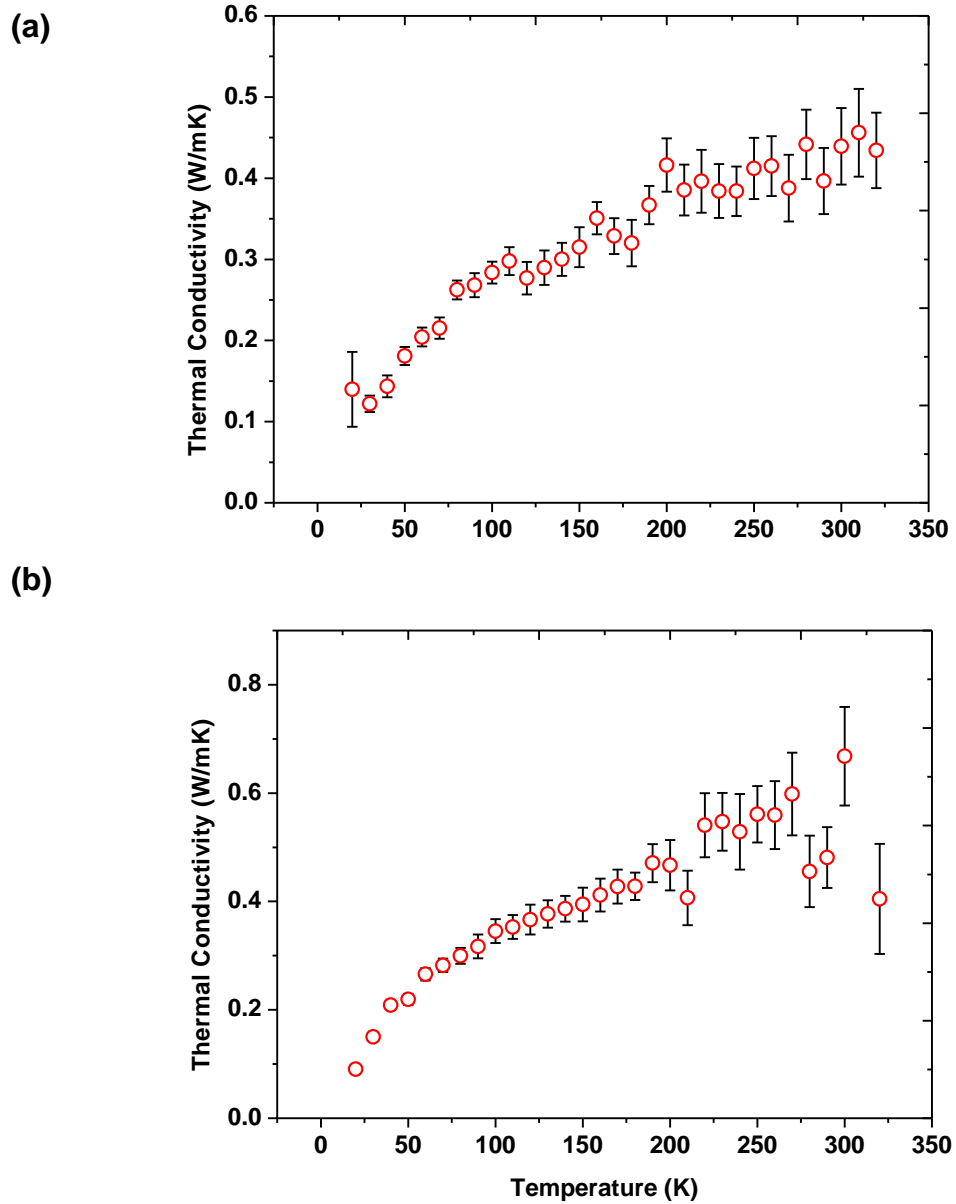


Figure 5-7 Plots of thermal conductivity versus temperature for two PE samples bonded on the micro device with FIB assisted Pt deposition.

Figure 5-7 shows the thermal conductivities of two typical PE samples bonded with FIB assisted Pt deposition. Both plots show an increasing trend of the thermal conductivity against ambient temperature. There is no decreasing trend at a high temperature range as what we observe for PE nanofibers clamped with super glue. Additionally, the measured thermal conductivities at all temperatures are generally smaller than those measured for the super glue bonded PE fibers. We conclude the FIB deposition process causes significant damage on the crystal structure of the PE fibers, although we apply a very low deposition current around 10pA. Due to the long time (~3minutes) exposure of high energy gallium ions, the PE fibers lose their initial crystal structure and become amorphous which results in a very low thermal conductivity. This conclusion can also be verified by figure 5-6(a,b), the circled regions are contaminated by the Pt deposition [178] and extend to an area much larger than the Pt covered area, which indicates the ion damage is not only limited to the Pt deposition region but also a large vicinity.

## **5.4 Conclusion**

PE nanofibers have been fabricated by the two-stage drawing method. For a PE nanofiber simply placed on the micro device without any extra bonds, the contact resistance between the nanofiber and the supporting islands is analyzed by the McGee et al.'s line contact model, and the results suggest a high thermal contact resistance which is close to the thermal resistance of a PE nanofiber on the micro device. However, we may use thermal devices with different gap sizes between the two islands to quantitatively measure the contact resistance. To reduce the thermal contact resistance, we have used two bonding methods, the cyanoacrylate based super glue and the FIB assisted Pt



bonding. Thermal conductivities of the PE fibers bonded by these two methods are measured at a temperature range from 20K to 320K. The experiment results show a crystal-like thermal conductivity trend for super glue clamped samples, while for the samples bonded by Pt deposition, there is only an increasing trend of the thermal conductivity observed.

## CHAPTER 6. Conclusions and outlook

### 6.1 Conclusions

Crystalline polymeric materials have significantly enhanced mechanical and thermal properties, due to their extended and ordered polymer chains. Especially when the dimensions of the crystallizable polymers reduce to micro/nanoscale, the number of defects per unit volume is much lower than that in their bulk counterparts; therefore, the scattering effect of phonons is dramatically alleviated, and the stress concentration which results in material failures is also mitigated. With the remarkable mechanical and thermal properties, and other intrinsic polymer properties, such as low density, high biocompatibility, easy processability etc., we can apply the crystalline polymeric materials in a variety of fields, for example, heat spreaders for electronics industry, personal armors for military, and high strength ropes for aircrafts.

To explore the mechanical properties of crystalline polymers, we use the linear polymer PE as a typical example of crystallizable polymers. A two-stage drawing method is adopted to fabricate the individual PE fibers with diameter size below  $1\mu\text{m}$ . In the two-stage drawing method, we first draw a PE fiber with a diameter in a  $\mu\text{m}$  range from a PE gel which is heated at a temperature  $\sim 130^\circ\text{C}$ , and then keep stretching the fiber at a high temperature environment ( $>90^\circ\text{C}$ ) until the fiber diameter reaches nm level. During the two-stage hot drawing process, the elongational flow initiates great polymer chain extension and ordering; the resulting PE fibers have highly extended and aligned PE chains which form an orthorhombic crystal structure.

We use the force deflection spectroscopy (FDS) technique to obtain the mechanical properties of the PE nanofibers. Typically, the PE nanofiber is placed on a specially designed micro trench by fixing two ends of the fiber using super glue. Atomic force microscopy (AFM) is performed to locate the middle point of the nanofiber. At the middle point, we deflect the nanofiber using an AFM cantilever. By knowing the deflection amount and the spring constant of the cantilever, based on the Bernoulli's beam equation, we are able to calculate the Young's modulus of the PE nanofibers. The experimental results demonstrate a very high Young's modulus  $\sim 312$  GPa of the PE nanofiber, the exceptionally high Young's modulus is attributed to an increased crystallinity in the PE nanofiber which has been proved by the selected area electron diffraction (SAED) pattern in transmission electron microscopy (TEM).

Polysilsesquioxane (PSQ) hybrid crystals are synthesized by a large scale and cheap sol-gel process. The hybrid crystals are formed by hydrogen bonds in the beam direction. We study the thermal transport in the PSQ hybrid crystals with a micro device with built-in heaters and thermometers. The micro device has two suspended islands with patterned Pt coils on the top surfaces. The PSQ beam is placed between the two islands, by applying a DC current to the Pt coil on one of the islands; Joule heating raises the temperature of the island. Heat is then transferred through the PSQ beam to the other island, and the patterned Pt coil serves as a thermometer for measuring the temperature rise. When heat transfer reaches a steady state, we measure the temperature different between the two islands, with the knowledge of the heat transferred through the sample; we are able to calculate a thermal conductance for the measured samples. Thermal conductivity can then

be derived after characterizing the geometric parameters including length and diameter of the samples.

The thermal characterizations of PSQ beams demonstrate a broad maximum of thermal conductivities centering around 120K. At a high temperature range (120K to 320K), the experiment results show that the thermal conductivity of the PSQ crystals is proportional to  $T^{-0.5}$ , which is not the commonly observed  $T^{-1}$  for single crystal solids. Non-equilibrium molecular dynamics (NEMD) simulations reveal that the anharmonic phonon scattering and the interfacial anharmonic coupling effects probably are responsible for the  $T^{-0.5}$  relation.

As the thermal conductivity measurements for PSQ beams, the same micro device based thermal characterization method has been applied on PE nanofibers which are also fabricated by the two-stage drawing method. By analyzing the line contact thermal resistance between a PE nanofiber and a Pt surface without additional bonds, we find the thermal contact resistance is comparable to the intrinsic thermal resistance of the PE nanofibers with a thermal conductivity of 20W/mK. To reduce the thermal contact resistance, we use cyanoacrylate based super glue to increase the contact area between the nanofiber and the supporting islands. The experiment results show a crystal-like trend of thermal conductivity versus temperature. However, the measured thermal conductivities are significantly smaller than the expected values which are about 104W/mK at room temperature. We suspect the super glue might lift the nanofibers above the surface of the islands and make a high thermal resistance between the nanofiber and the islands. We also tried focus ion beam (FIB) based Pt deposition to enhance the interfacial thermal transport; however, the measured thermal conductivities

are all smaller than 1W/mK at the measured temperature range. Careful SEM characterizations illustrate significant Pt contamination and ion beam damage to the PE nanofibers, which result in the very low thermal conductivities.

## **6.2 Outlook and future work**

Crystalline polymers possess interesting properties as demonstrated in the thesis, for example, the enhanced mechanical and thermal properties for the PE nanofibers, and the tunable thermal property of the PSQ crystal. However, there are various other stereoregular polymers which can crystallize, such as polypropylene (PP), poly(ethylene oxide) (PEO), poly(p-phenylene sulfide) (PPS) etc. It will be of great interest to study mechanical and thermal properties of nanofibers derived from these polymers, especially those with aromatic ring backbones or other forms of backbones, rather than carbon-carbon chains. Additionally, mass production of crystalline polymer nanofibers is very important for practical applications of these nanofibers, apparently, the two-stage drawing method presented in the thesis is only for initial characterization and study. Therefore, future effort should be devoted to developing more robust mass production methods which should yield highly crystalline fibers in nanoscale. Furthermore, the study of thermal contact resistance for polymer nanofiber and platinum (Pt) in Chapter 5 illustrates a method and direction for the research of interfacial thermal transport. Further research on this topic will give a fundamental understanding of the thermal properties of composite materials, in which fibers with interested properties are embedded in a polymer matrix.

## References

- [1] M. Ashby, *Materials selection in mechanical design*, 3rd ed. Burlington, Massachusetts: Butterworth-Heinemann, 1999.
- [2] L. Sperling, *Introduction to physical polymer science*, 4th ed. Hoboken, New Jersey: John Wiley & Sons, Inc., 2005.
- [3] J. Lee, D. Yoon, and H. Cheong, "Estimation of Young's modulus of graphene by Raman spectroscopy," *Nano Lett.*, vol. 12, pp. 4444–4448, 2012.
- [4] A. A. Balandin, S. Ghosh, W. Bao, I. Calizo, D. Teweldebrhan, F. Miao, and C. N. Lau, "Superior thermal conductivity of single-layer graphene," *Nano Lett.*, vol. 8, pp. 902–907, 2008.
- [5] M. M. J. Treacy, T. W. Ebbesen, and J. M. Gibson, "Exceptionally high Young's modulus observed for individual carbon nanotubes," *Nature*. 1996.
- [6] P. Kim, L. Shi, A. Majumdar, and P. L. McEuen, "Thermal transport measurements of individual multiwalled nanotubes," *Phys. Rev. Lett.*, vol. 87, p. 215502, 2001.
- [7] A. Toda, "Polyethylene crystallization from dilute solutions: adsorption isotherm on the growth face," *J. Chem. Soc. Faraday Trans.*, vol. 91, no. 16, p. 2581, 1995.
- [8] J. E. Breedon, J. F. Jackson, M. J. Marcinkowski, and M. E. Taylor, "Study of polyethylene spherulites using scanning electron microscopy," *J. Mater. Sci.*, vol. 8, pp. 1071–1082, 1973.
- [9] D. C. Bassett and A. M. Hodge, "On lamellar organization in certain polyethylene spherulites," *Proc. R. Soc. A Math. Phys. Eng. Sci.*, vol. 359, pp. 121–132, 1978.
- [10] Laemmli, "Polyethylene spherulites," *Nature*, vol. 227, pp. 701–702, 1970.
- [11] L. Mandelkern, "Structure and properties of polymer crystals formed in dilute solutions," *Annu. Rev. Mater. Sci.*, vol. 6, no. 7, pp. 119–138, 1976.
- [12] G. C. Oppenlander, "Structure and properties of crystalline polymers," *Science* (80-. ), vol. 159, no. 43, pp. 1311–1319, 1968.
- [13] H. S. Park, J. H. Lee, J. Nam, and Y. K. Lee, "Ultra-drawing of gelfilms of ultra high molecular weight polyethylene/low molecular weight polymer blends containing BaTiO<sub>3</sub> nanoparticles," *Macromol. Res.*, vol. 14, no. 4, pp. 430–437, 2006.

- [14] C. Xu and M. Matsuo, "Crystal Poisson's ratios of polyethylene and poly(vinylalcohol) estimated by X-ray diffraction using the ultradrawn films," *Macromolecules*, vol. 32, no. 9, pp. 3006–3016, May 1999.
- [15] C. L. Choy, Y. W. Wong, G. W. Yang, and T. Kanamoto, "Elastic modulus and thermal conductivity of ultradrawn polyethylene," *J. Polym. Sci. Part B Polym. Phys.*, vol. 37, pp. 3359–3367, 1999.
- [16] C. W. M. Bastiaansen and G. P. Grooters, "Tensile strength of solution-spun, ultradrawn ultra-high molecular weight polyethylene fibres: 2. Influence of propylene comonomer content," *Polymer (Guildf.)*, vol. 33, no. 8, pp. 1653–1655, 1992.
- [17] H. Fujimatsu, Y. S. Kim, H. Matsuzaki, A. Nakamura, H. Usami, and S. Ogasawara, "Drawing properties and physical properties of ultrahigh-molecular-weight polyethylene swollen in mixed solvent," *Polym. J.*, vol. 33, no. 10, p. 709, 2001.
- [18] J. Smook, J. C. Torfs, P. F. van Hutten, and A. J. Pennings, "Ultra-high strength polyethylene by hot drawing of surface growth fibers," *Polym. Bull.*, vol. 2, pp. 293–300, 1980.
- [19] R. Marissen, "Design with ultra strong polyethylene fibers," *Mater. Sci. Appl.*, vol. 02, pp. 319–330, 2011.
- [20] F. S. F. Sarvar, D. C. Whalley, and P. P. Conway, "Thermal interface materials - a review of the state of the art," *2006 1st Electron. Syst. Technol. Conf.*, vol. 2, 2006.
- [21] X. Zhou, S. Yang, C. Yu, Z. Li, X. Yan, Y. Cao, and D. Zhao, "Hexylene- and octylene-bridged polysilsesquioxane hybrid crystals self-assembled by dimeric building blocks with ring structures.," *Chemistry*, vol. 12, no. 33, pp. 8484–90, Nov. 2006.
- [22] P. Smith, P. J. Lemstra, B. Kalb, and A. J. Pennings, "Ultrahigh-strength polyethylene filaments by solution spinning and hot drawing," *Polym. Bull.*, vol. 1, pp. 733–736, 1979.
- [23] G. Capaccio, T. J. Chapman, and I. M. Ward, "Preparation of ultra-high modulus linear polyethylenes: Effect of initial crystallization conditions," *Polymer (Guildf.)*, vol. 16, p. 469, 1975.
- [24] D. J. Dijkstra and A. J. Pennings, "The role of taut tie molecules on the mechanical properties of gel-spun UHMWPE fibers," *Polym. Bull.*, vol. 19, pp. 73–80, 1988.
- [25] J. P. Penning, H. Van Der Werff, M. Roukema, and A. J. Pennings, "On the theoretical strength of gelspun hotdrawn ultra-high molecular weight polyethylene fibers," *Polym. Bull.*, vol. 23, pp. 347–352, 1990.

- [26] A. Henry and G. Chen, “High thermal conductivity of single polyethylene chains using molecular dynamics simulations,” *Phys. Rev. Lett.*, vol. 101, no. 23, p. 235502, Dec. 2008.
- [27] X. Wang, V. Ho, R. a. Segalman, and D. G. Cahill, “Thermal conductivity of high-modulus polymer fibers,” *Macromolecules*, vol. 46, no. 12, pp. 4937–4943, Jun. 2013.
- [28] A. Yamanaka, H. Fujishiro, T. Kashima, T. Kitagawa, K. Ema, Y. Izumi, M. Ikebe, and S. Nishijima, “Thermal conductivity of high strength polyethylene fiber in low temperature,” *J. Polym. Sci. Part B Polym. Phys.*, vol. 43, pp. 1495–1503, 2005.
- [29] T. Zhang and T. Luo, “Morphology-influenced thermal conductivity of polyethylene single chains and crystalline fibers,” *J. Appl. Phys.*, vol. 112, no. 9, p. 094304, 2012.
- [30] D. D. L. Chung, “Materials for thermal conduction,” *Appl. Therm. Eng.*, vol. 21, pp. 1593–1605, 2001.
- [31] S. Shen, A. Henry, J. Tong, R. Zheng, and G. Chen, “Polyethylene nanofibres with very high thermal conductivities,” *Nat. Nanotechnol.*, vol. 5, no. 4, pp. 251–5, Apr. 2010.
- [32] A. Yamanaka, H. Fujishiro, T. Kashima, T. Kitagawa, K. Ema, Y. Izumi, M. Ikebe, and S. Nishijima, “Thermal conductivity of high strength polyethylene fiber in low temperature,” *J. Polym. Sci. Part B Polym. Phys.*, vol. 43, no. 12, pp. 1495–1503, Jun. 2005.
- [33] A. Yamanaka and T. Takao, “Thermal conductivity of high-strength polyethylene fiber and applications for cryogenic use,” *ISRN Mater. Sci.*, vol. 2011, pp. 1–10, 2011.
- [34] C. L. Choy, S. P. Wong, and K. Young, “Model calculation of the thermal conductivity of polymer crystals,” *J. Polym. Sci. Polym. Phys. Ed.*, vol. 23, pp. 1495–1504, 1985.
- [35] C. L. Choy and W. P. Leung, “Thermal conductivity of ultradrawn polyethylene,” *J. Polym. Sci. Polym. Phys. Ed.*, vol. 21, no. 3, pp. 1243–1246, 1983.
- [36] A. G. Gibson, D. Greig, and I. M. Ward, “Thermal conductivity of ultrahigh modulus polyethylene,” *J. Polym. Sci. Polym. Phys. Ed.*, vol. 18, pp. 1481–1482, 1980.
- [37] H. Lodish, A. Berk, S. L. Zipursky, P. Matsudaira, D. Baltimore, and J. Darnell, *Molecular cell biology*, 4th ed. New York: W. H. Freeman, 2000.



- [38] I. Alkorta and I. Rozas, “Non-conventional hydrogen bonds,” *Chem. Soc. Rev.*, vol. 27, pp. 163–170, 1998.
- [39] S. Chen, A. L. Moore, W. Cai, J. W. Suk, J. An, C. Mishra, C. Amos, C. W. Magnuson, J. Kang, L. Shi, and R. S. Ruoff, “Raman measurements of thermal transport in suspended monolayer graphene of variable sizes in vacuum and gaseous environments,” *ACS Nano*, vol. 5, no. 1, pp. 321–8, Jan. 2011.
- [40] C. Yu, L. Shi, Z. Yao, D. Lil, and A. Majumdar, “Thermal conductance and thermopower of an individual single-wall carbon nanotube,” *Nano Lett.*, vol. 5, pp. 1842–1846, 2005.
- [41] L. Zhang, T. Chen, H. Ban, and L. Liu, “Hydrogen bonding-assisted thermal conduction in  $\beta$ -sheet crystals of spider silk protein,” *Nanoscale*, vol. 6, no. 14, pp. 7786–91, Jul. 2014.
- [42] P. A. E. Schoen, B. Michel, A. Curioni, and D. Poulikakos, “Hydrogen-bond enhanced thermal energy transport at functionalized, hydrophobic and hydrophilic silica–water interfaces,” *Chem. Phys. Lett.*, vol. 476, no. 4–6, pp. 271–276, Jul. 2009.
- [43] G.-H. Kim, D. Lee, A. Shanker, L. Shao, M. S. Kwon, D. Gidley, J. Kim, and K. P. Pipe, “High thermal conductivity in amorphous polymer blends by engineered interchain interactions,” *Nat. Mater.*, vol. 14, pp. 295–300, 2014.
- [44] D. A. Loy and K. J. Shea, “Bridged polysilsesquioxanes. Highly porous hybrid organic-inorganic materials,” *Chem. Rev.*, vol. 95, pp. 1431–1442, 1995.
- [45] H. W. J. Oviatt, K. J. Shea, S. Kalluri, Y. Shi, W. H. Steier, and L. R. Dalton, “Applications of organic bridged polysilsesquioxane xerogels to nonlinear optical materials by the sol-gel method,” *Chem. Mater.*, vol. 7, no. 18, pp. 493–498, 1995.
- [46] E. S. Clark and L. S. Scott, “Superdrawn crystalline polymers: A new class of high-strength fiber,” *Polym. Eng. Sci.*, vol. 14, no. 10, pp. 682–686, Oct. 1974.
- [47] C. L. Choy, Y. Fei, and T. G. Xi, “Thermal conductivity of gel-spun polyethylene fibers,” *J. Polym. Sci. Part B*, vol. 31, pp. 365–370, 1993.
- [48] A. Zwijnenburg and A. J. Pennings, “Longitudinal growth of polymer crystals from flowing solutions II. Polyethylene crystals in Poiseuille flow,” *Colloid Polym. Sci.*, vol. 253, pp. 452–461, 1975.
- [49] A. Zwijnenburg and A. J. Pennings, “Longitudinal growth of polymer crystals from flowing solutions III. Polyethylene crystals in Couette flow,” *Colloid Polym. Sci.*, vol. 254, pp. 868–881, 1976.

- [50] A. Zwijnenburg, P. F. Van Hulten, A. J. Pennings, and H. D. Chanzy, "Longitudinal growth of polymer crystals from flowing solutions V.: Structure and morphology of fibrillar polyethylene crystals," *Colloid Polym. Sci.*, vol. 256, pp. 729–750, 1978.
- [51] A. J. Pennings and A. Zwijnenburg, "Longitudinal growth of polymer crystals from flowing solutions. VI. Melting behavior of continuous fibrillar polyethylene crystals," *J. Polym. Sci. Polym. Phys. Ed.*, vol. 17, no. 6, pp. 1011–1032, Jun. 1979.
- [52] P. J. Barham and A. Keller, "High-strength polyethylene fibres from solution and gel spinning," *J. Mater. Sci.*, vol. 20, no. 7, pp. 2281–2302, Jul. 1985.
- [53] P. Smith and P. J. Lemstra, "Ultrahigh strength polyethylene filaments by solution spinning/drawing. 3. Influence of drawing temperature," *Polymer (Guildf.)*, vol. 21, pp. 1341–1343, 1980.
- [54] K. Kageyama, J. Tamazawa, and T. Aida, "Extrusion polymerization: Catalyzed synthesis of crystalline linear polyethylene nanofibers within a mesoporous silica," *Science (80-. )*, vol. 285, no. 5436, pp. 2113–2115, Sep. 1999.
- [55] A. Theron, E. Zussman, and A. L. Yarin, "Electrostatic field-assisted alignment of electrospun nanofibres," *Nanotechnology*, vol. 12, pp. 384–390, 2001.
- [56] E. Zussman, X. Chen, W. Ding, L. Calabri, D. A. Dikin, J. P. Quintana, and R. S. Ruoff, "Mechanical and structural characterization of electrospun PAN-derived carbon nanofibers," *Carbon N. Y.*, vol. 43, no. 10, pp. 2175–2185, Aug. 2005.
- [57] J. H. Wendorff and A. Greiner, "Functional self-assembled nanofibers by electrospinning," *Adv. Polym. Sci.*, vol. 219, pp. 107–171, 2008.
- [58] A. Greiner and J. H. Wendorff, "Electrospinning: A fascinating method for the preparation of ultrathin fibers," *Angew. Chem. Int. Ed. Engl.*, vol. 46, no. 30, pp. 5670–703, Jan. 2007.
- [59] D. Rein, L. Shavit-Hadar, R. Khalfin, Y. Cohen, S. K, and E. Zussman, "Electrospinning of ultrahigh-molecular-weight polyethylene nanofibers," *J. Polym. Sci. Part B Polym. Phys.*, vol. 45, pp. 766–773, 2007.
- [60] J. L. White and Y. Ide, "Instabilities and failure in elongational flow and melt spinning of fibers," *J. Appl. Polym. Sci.*, vol. 22, pp. 3057–3074, 1978.
- [61] J. R. Dees and Spruiell .E., "Structure development during melt spinning of linear polyethylene fibers," *J. Appl. Polym. Sci.*, vol. 18, pp. 1053–1078, 1974.

- [62] P. Smith and P. J. Lemstra, "Ultrahigh-strength polyethylene filaments by solution spinning/drawing, 2(a). Influence of solvent on the drawability," *Makromol. Chemie*, vol. 180, pp. 2983–2986, 1979.
- [63] Z. Yufeng, X. Changfa, J. I. A. Guangxia, and A. N. Shulin, "Study on gel-spinning process of ultra-high molecular weight polyethylene," *J. Appl. Polym. Sci.*, vol. 74, no. 670, pp. 670–675, 1999.
- [64] A. J. Pennings, R. J. Hooft, A. R. Postema, W. Hoogsteen, and G. Brinke, "High-speed gel-spinning of ultra-high molecular weight polyethylene," *Polym. Bull.*, vol. 16, pp. 167–174, 1986.
- [65] T. Subbiah, G. S. Bhat, R. W. Tock, S. Parameswaran, and S. S. Ramkumar, "Electrospinning of nanofibers," *J. Appl. Polym. Sci.*, vol. 96, pp. 557–569, 2005.
- [66] S. H. Tan, R. Inai, M. Kotaki, and S. Ramakrishna, "Systematic parameter study for ultra-fine fiber fabrication via electrospinning process," *Polymer (Guildf)*, vol. 46, pp. 6128–6134, 2005.
- [67] N. Bhardwaj and S. C. Kundu, "Electrospinning: A fascinating fiber fabrication technique," *Biotechnol. Adv.*, vol. 28, pp. 325–347, 2010.
- [68] E. Zussman, M. Burman, A. L. Yarin, R. Khalfin, and Y. Cohen, "Tensile Deformation of Electrospun Nylon-6 , 6 Nanofibers," *J. Polym. Sci. Part B Polym. Phys.*, vol. 44, pp. 9–12, 2006.
- [69] X. Sui, E. Wiesel, and H. D. Wagner, "Mechanical properties of electrospun PMMA micro-yarns: Effects of NaCl mediation and yarn twist," *Polymer (Guildf)*, vol. 53, no. 22, pp. 5037–5044, Oct. 2012.
- [70] S.-H. Lee, C. Tekmen, and W. M. Sigmund, "Three-point bending of electrospun TiO<sub>2</sub> nanofibers," *Mater. Sci. Eng. A*, vol. 398, no. 1–2, pp. 77–81, May 2005.
- [71] S. R. Givens, K. H. Gardner, J. F. Rabolt, and D. B. Chase, "High-temperature electrospinning of polyethylene microfibers from solution," *Macromolecules*, vol. 40, no. 3, pp. 608–610, Feb. 2007.
- [72] A. Nakajima and S. Hayashi, "Lamellar thickness of polyethylene single crystal isothermally crystallized in dilute solution," *Kolloid-Zeitschrift und Zeitschrift fur Polym.*, vol. 225, pp. 116–121, 1968.
- [73] D. E. Smith, H. P. Babcock, and S. Chu, "Single-polymer dynamics in steady shear flow," *Science (80-. )*, vol. 283, no. 5408, pp. 1724–1727, Mar. 1999.

- [74] E. W. Wong, P. E. Sheehan, and C. M. Lieber, "Nanobeam mechanics: elasticity, strength, and toughness of nanorods and nanotubes," *Science* (80-. ), vol. 1971, 2012.
- [75] J. J. Petrovic, J. V. Milewski, D. L. Rohr, and F. D. Gac, "Tensile mechanical properties of SiC whiskers," *J. Mater. Sci.*, vol. 20, pp. 1167–1177, 1985.
- [76] P. Poncharal, Z. Wang, D. Ugarte, and de Heer WA, "Electrostatic deflections and electromechanical resonances of carbon nanotubes," *Science*, vol. 283, no. 5407, pp. 1513–6, Mar. 1999.
- [77] X. Li, H. Gao, C. Murphy, and K. Caswell, "Nanoindentation of silver nanowires," *Nano Lett.*, vol. 3, no. 11, pp. 1495–1498, 2003.
- [78] H. Ni and X. Li, "Young's modulus of ZnO nanobelts measured using atomic force microscopy and nanoindentation techniques," *Nanotechnology*, vol. 17, no. 14, pp. 3591–7, Jul. 2006.
- [79] E. P. S. Tan and C. T. Lim, "Nanoindentation study of nanofibers," *Appl. Phys. Lett.*, vol. 87, no. 12, p. 123106, 2005.
- [80] Q. Xiong, N. Duarte, S. Tadigadapa, and P. C. Eklund, "Force-deflection spectroscopy: a new method to determine the Young's modulus of nanofilaments," *Nano Lett.*, vol. 6, no. 9, pp. 1904–9, Sep. 2006.
- [81] B. Wu, A. Heidelberg, and J. J. Boland, "Mechanical properties of ultrahigh-strength gold nanowires," *Nat. Mater.*, vol. 4, no. 7, pp. 525–9, Jul. 2005.
- [82] J.-P. Salvetat, J.-M. Bonard, N. H. Thomson, A. J. Kulik, L. Forró W. Benoit, and L. Zuppiroli, "Mechanical properties of carbon nanotubes," *Appl. Phys. A Mater. Sci. Process.*, vol. 69, no. 3, pp. 255–260, Sep. 1999.
- [83] Y. Chen, I. Stevenson, R. Pouy, L. Wang, D. N. McIlroy, T. Pounds, M. Grant Norton, and D. Eric Aston, "Mechanical elasticity of vapour-liquid-solid grown GaN nanowires," *Nanotechnology*, vol. 18, no. 13, p. 135708, Apr. 2007.
- [84] P. Zhou, C. Wu, and X. Li, "Three-point bending Young's modulus of nanowires," *Meas. Sci. Technol.*, vol. 19, no. 11, p. 115703, Nov. 2008.
- [85] G. Fang and A. Amirfazli, "Understanding the edge effect in wetting: A thermodynamic approach," *Langmuir*, vol. 28, pp. 9421–9430, 2012.
- [86] B. Cappella and G. Dietler, "Force-distance curves by atomic force microscopy," *Surf. Sci. Rep.*, vol. 34, pp. 1–104, 1999.

- [87] J. Cao, D. K. Pham, L. Tonge, and D. V Nicolau, "Study of atomic force microscopy force distance curves by simulation using the Connolly surface for proteins," *Smart Mater. Struct.*, vol. 11, pp. 767–771, 2002.
- [88] W. T. Johnson, "Using thermal k to calibrate the spring constants (k) of AFM probes," *Agil. Technol.*, 2008.
- [89] D. G. Cahill, "Thermal conductivity measurement from 30 to 750 K: the  $3\omega$  method," *Rev. Sci. Instrum.*, vol. 61, no. 2, p. 802, 1990.
- [90] X. J. Hu, A. a. Padilla, J. Xu, T. S. Fisher, and K. E. Goodson, "3-omega measurements of vertically oriented carbon nanotubes on silicon," *J. Heat Transfer*, vol. 128, no. 11, p. 1109, 2006.
- [91] E. Dechaumphai, J. L. Barton, J. R. Tesmer, J. Moon, Y. Wang, G. R. Tynan, R. P. Doerner, and R. Chen, "Near-surface thermal characterization of plasma facing components using the 3-omega method," *J. Nucl. Mater.*, vol. 455, no. 1–3, pp. 56–60, Dec. 2014.
- [92] T. Tong and A. Majumdar, "Reexamining the 3-omega technique for thin film thermal characterization," *Rev. Sci. Instrum.*, vol. 77, no. 10, p. 104902, 2006.
- [93] W. S. Capinski and H. J. Maris, "Improved apparatus for picosecond pump-and-probe optical measurements," *Rev. Sci. Instrum.*, vol. 67, p. 2720, 1996.
- [94] B. Bonello, B. Perrin, and C. C. Rossignol, "Photothermal properties of bulk and layered materials by the picosecond acoustics technique," *J. Appl. Phys.*, vol. 83, pp. 3081–3088, 1998.
- [95] K. T. Regner, S. Majumdar, and J. A. Malen, "Instrumentation of broadband frequency domain thermoreflectance for measuring thermal conductivity accumulation functions," *Rev. Sci. Instrum.*, vol. 84, 2013.
- [96] A. J. Schmidt, R. Cheaito, and M. Chiesa, "A frequency-domain thermoreflectance method for the characterization of thermal properties," *Rev. Sci. Instrum.*, vol. 80, 2009.
- [97] J. A. Malen, K. Baheti, T. Tong, Y. Zhao, J. A. Hudgings, and A. Majumdar, "Optical measurement of thermal conductivity using fiber aligned frequency domain thermoreflectance," *J. Heat Transfer*, vol. 133, p. 081601, 2011.
- [98] J. H. Seol, A. L. Moore, S. K. Saha, F. Zhou, L. Shi, Q. L. Ye, R. Scheffler, N. Mingo, and T. Yamada, "Measurement and analysis of thermopower and electrical conductivity of an indium antimonide nanowire from a vapor-liquid-solid method," *J. Appl. Phys.*, vol. 101, no. 2, p. 023706, 2007.

- [99] J. Lim, K. Hippalgaonkar, S. C. Andrews, A. Majumdar, and P. Yang, "Quantifying surface roughness effects on phonon transport in silicon nanowires," *Nano Lett.*, vol. 12, no. 5, pp. 2475–82, May 2012.
- [100] Z. Zhong, M. C. Wingert, J. Strzalka, H.-H. Wang, T. Sun, J. Wang, R. Chen, and Z. Jiang, "Structure-induced enhancement of thermal conductivities in electrospun polymer nanofibers," *Nanoscale*, vol. 6, no. 14, pp. 8283–91, Jul. 2014.
- [101] V. Thomsen, "Response time of a thermometer," *Phys. Teach.*, vol. 36, p. 540, 1998.
- [102] M. F. Ashby, *Materials Selection in Mechanical Design*, 3rd ed. Burlington, Massachusetts: Butterworth-Heinemann, 2005.
- [103] Z.-M. Huang, Y.-Z. Zhang, M. Kotaki, and S. Ramakrishna, "A review on polymer nanofibers by electrospinning and their applications in nanocomposites," *Compos. Sci. Technol.*, vol. 63, no. 15, pp. 2223–2253, Nov. 2003.
- [104] P. Smith and P. J. Lemstra, "Ultra-high-strength polyethylene filaments by solution spinning/drawing," *J. Mater. Sci.*, vol. 15, no. 2, pp. 505–514, Feb. 1980.
- [105] P. Smith, P. J. Lemstra, and J. P. L. Pijpers, "Tensile strength of highly oriented polyethylene. II. Effect of molecular weight distribution," *J. Polym. Sci. Polym. Phys. Ed.*, vol. 20, pp. 2229–2241, 1982.
- [106] A. J. Pennings, R. Lageveen, and R. S. De Vries, "Hydrodynamically induced crystallization of polymers from solution VII. : On the origin of persistent lamellar overgrowth of Shish-kebab fibers," *Colloid Polym. Sci.*, vol. 255, pp. 532–542, 1977.
- [107] P. J. Barham and A. Keller, "A study on the achievement of high-modulus polyethylene fibres by drawing," *J. Mater. Sci.*, vol. 11, pp. 27–35, 1976.
- [108] G. Capaccio and I. Ward, "Preparation of ultra-high modulus linear polyethylenes; effect of molecular weight and molecular weight distribution on drawing behaviour and mechanical properties," *Polymer (Guildf)*, vol. 15, pp. 233–238, 1974.
- [109] Y. Zhang, D. Rodrigue, and A. Ait-kadi, "High density polyethylene foams. II. Elastic modulus," *J. Appl. Polym. Sci.*, vol. 90, pp. 2120–2129, 2003.
- [110] J.-W. Jiang, J. Zhao, K. Zhou, and T. Rabczuk, "Superior thermal conductivity and extremely high mechanical strength in polyethylene chains from ab initio calculation," *J. Appl. Phys.*, vol. 111, no. 12, p. 124304, 2012.

- [111] R. Martoňák, W. Paul, and K. Binder, "Orthorhombic phase of crystalline polyethylene: A Monte Carlo study," *J. Chem. Phys.*, vol. 106, no. 21, p. 8918, 1997.
- [112] B. Crist, "The ultimate strength and stiffness of polymers," *Annu. Rev. Mater. Sci.*, vol. 25, no. 1, pp. 295–323, 1995.
- [113] B. Fanconi and J. F. Rabolt, "The determination of longitudinal crystal moduli in polymers by spectroscopic methods," *J. Polym. Sci. Polym. Phys. Ed.*, vol. 23, pp. 1201–1215, 1985.
- [114] R. J. Meier, "Regarding the ultimate Young's modulus of a single polyethylene chain," *Macromolecules*, vol. 26, no. 16, pp. 4376–4378, Aug. 1993.
- [115] A. Keller and H. W. H. Kolnaar, *Processing of polymers*. VCH: New York, 1997.
- [116] R. H. Somani, L. Yang, L. Zhu, and B. S. Hsiao, "Flow-induced shish-kebab precursor structures in entangled polymer melts," *Polymer (Guildf.)*, vol. 46, no. 20, pp. 8587–8623, Sep. 2005.
- [117] P. J. Barham, "Gelation and the production of stiff polyethylene fibres," *Polymer (Guildf.)*, vol. 23, pp. 1112–1122, 1982.
- [118] D. T. Grubb and A. Keller, "Thermal contraction and extension in fibrous crystals of polyethylene," *Colloid Polym. Sci.*, vol. 256, no. 3, pp. 218–233, Mar. 1978.
- [119] D. E. Smith and S. Chu, "Response of flexible polymers to a sudden elongational flow," *Science (80-. )*, vol. 281, no. 5381, pp. 1335–1340, Aug. 1998.
- [120] NT-MDT, "Probe-sample interaction : Lateral forces," <http://www.ntmdt.com>. .
- [121] H. Van Der Werff and A. J. Pennings, "Tensile deformation of high strength and high modulus polyethylene fibers," *Colloid Polym. Sci.*, vol. 269, pp. 747–763, 1991.
- [122] D. M. Rein, Y. Cohen, J. Lipp, and E. Zussman, "Elaboration of ultra-high molecular weight polyethylene/carbon nanotubes electrospun composite fibers," *Macromol. Mater. Eng.*, vol. 295, no. 11, pp. 1003–1008, Nov. 2010.
- [123] F. Chen, X. Peng, T. Li, S. Chen, X.-F. Wu, D. H. Reneker, and H. Hou, "Mechanical characterization of single high-strength electrospun polyimide nanofibres," *J. Phys. D. Appl. Phys.*, vol. 41, no. 2, p. 025308, Jan. 2008.
- [124] S. Cuenot, S. Demoustier-Champagne, and B. Nysten, "Elastic modulus of polypyrrole nanotubes," *Phys. Rev. Lett.*, vol. 85, no. 8, pp. 1690–3, Aug. 2000.

- [125] E. P. S. Tan, Y. Zhu, T. Yu, L. Dai, C. H. Sow, V. B. C. Tan, and C. T. Lim, "Crystallinity and surface effects on Young's modulus of CuO nanowires," *Appl. Phys. Lett.*, vol. 90, no. 16, p. 163112, 2007.
- [126] E. P. S. Tan and C. T. Lim, "Effects of annealing on the structural and mechanical properties of electrospun polymeric nanofibres," *Nanotechnology*, vol. 17, no. 10, pp. 2649–54, May 2006.
- [127] S. M. Cook, K. M. Lang, K. M. Chynoweth, M. Wigton, R. W. Simmonds, and T. E. Schäffer, "Practical implementation of dynamic methods for measuring atomic force microscope cantilever spring constants," *Nanotechnology*, vol. 17, no. 9, pp. 2135–2145, May 2006.
- [128] A. S. Nain, C. Amon, and M. Sitti, "Proximal probes based nanorobotic drawing of polymer micro/nanofibers," *IEEE Trans. Nanotechnol.*, vol. 5, no. 5, pp. 499–510, Sep. 2006.
- [129] J. Zhao, W. Guo, and T. Rabczuk, "An analytical molecular mechanics model for the elastic properties of crystalline polyethylene," *J. Appl. Phys.*, vol. 112, no. 3, p. 033516, 2012.
- [130] M. K. Shin, S. I. Kim, S. J. Kim, S.-K. Kim, H. Lee, and G. M. Spinks, "Size-dependent elastic modulus of single electroactive polymer nanofibers," *Appl. Phys. Lett.*, vol. 89, no. 23, p. 231929, 2006.
- [131] L. Sun, R. P. S. Han, J. Wang, and C. T. Lim, "Modeling the size-dependent elastic properties of polymeric nanofibers," *Nanotechnology*, vol. 19, no. 45, p. 455706, Nov. 2008.
- [132] A. Arinstein, M. Burman, O. Gendelman, and E. Zussman, "Effect of supramolecular structure on polymer nanofibre elasticity," *Nat. Nanotechnol.*, vol. 2, no. 1, pp. 59–62, Jan. 2007.
- [133] R. Wagner, R. Moon, J. Pratt, G. Shaw, and A. Raman, "Uncertainty quantification in nanomechanical measurements using the atomic force microscope," *Nanotechnology*, vol. 22, no. 45, p. 455703, Nov. 2011.
- [134] B. Ohler, "Cantilever spring constant calibration using laser Doppler vibrometry," *Rev. Sci. Instrum.*, vol. 78, no. 6, p. 063701, Jun. 2007.
- [135] L. Sperling, *Introduction to physical polymer science*, 4th ed. Hoboken, New Jersey: John Wiley & Sons, 2005.
- [136] M. Jouni, A. Boudenne, G. Boiteux, V. Massardier, B. Garnier, and A. Serghei, "Electrical and thermal properties of polyethylene/silver nanoparticle composites," *Polym. Compos.*, vol. 34, no. 5, pp. 778–786, 2013.



- [137] Y. P. Mamunya, V. V. Davydenko, P. Pissis, and E. V. Lebedev, "Electrical and thermal conductivity of polymers filled with metal powders," *Eur. Polym. J.*, vol. 38, no. 9, pp. 1887–1897, Sep. 2002.
- [138] M. J. Biercuk, M. C. Llaguno, M. Radosavljevic, J. K. Hyun, A. T. Johnson, and J. E. Fischer, "Carbon nanotube composites for thermal management," *Appl. Phys. Lett.*, vol. 80, no. 15, p. 2767, 2002.
- [139] A. M. Marconnet, N. Yamamoto, M. A. Panzer, B. L. Wardle, and K. E. Goodson, "Thermal conduction in aligned carbon nanotube - Polymer nanocomposites with high packing density," *ACS Nano*, vol. 5, no. 6, pp. 4818–4825, 2011.
- [140] D. Greig and M. Sahota, "Thermal conductivity of extruded polyethylene," *Polymer (Guildf.)*, vol. 19, pp. 503–505, 1978.
- [141] P. Judeinstein and C. Sanchez, "Hybrid organic-inorganic materials: A land of multidisciplinary chemistry: Synthesis of hybrid materials," *J. Mater. Chem.*, vol. 6, no. 4, pp. 511–525, 1996.
- [142] F. Dong and C.-S. Ha, "Multifunctional materials based on polysilsesquioxanes," *Macromol. Res.*, vol. 20, no. 4, pp. 335–343, Apr. 2012.
- [143] L. Wu, Q. Chen, Z. Lv, W. Sun, L. Chen, and J. Wu, "Bithiazole-bridged polysilsesquioxane and its metal complexes: synthesis and magnetic properties," *J. Sol-Gel Sci. Technol.*, vol. 60, no. 2, pp. 214–220, Oct. 2011.
- [144] K. J. Shea and D. A. Loy, "Bridged polysilsesquioxanes molecular-engineered hybrid organic - inorganic materials," *Chem. Mater.*, vol. 13, pp. 3306–3319, 2001.
- [145] A. N. Parikh, M. A. Schivley, E. Koo, K. Seshadri, D. Aurentz, K. Mueller, and D. L. Allara, "n-Alkylsiloxanes: From single monolayers to layered crystals. The formation of crystalline polymers from the hydrolysis of n-Octadecyltrichlorosilane," *J. Am. Chem. Soc.*, vol. 7863, no. 2, pp. 3135–3143, 1997.
- [146] M. Beaudhuin, "Thermal conductivity measurement of thin layers by the  $3\omega$  method," *Koninklijke Philips Electronics*, 2006.
- [147] J.-U. Lee, D. Yoon, H. Kim, S. W. Lee, and H. Cheong, "Thermal conductivity of suspended pristine graphene measured by Raman spectroscopy," *Phys. Rev. B*, vol. 83, no. 8, p. 081419, Feb. 2011.
- [148] R. Yan, J. R. Simpson, S. Bertolazzi, J. Brivio, M. Watson, X. Wu, A. Kis, T. Luo, A. R. H. Walker, and H. G. Xing, "Thermal conductivity of monolayer molybdenum disulfide obtained from temperature dependent Raman spectroscopy," *ACS Nano*, vol. 8, pp. 986–993, 2014.

- [149] B. Stoib, S. Filser, N. Petermann, H. Wiggers, M. Stutzmann, and M. S. Brandt, "Thermal conductivity of mesoporous films measured by Raman spectroscopy," *Appl. Phys. Lett.*, vol. 104, no. 16, p. 161907, Apr. 2014.
- [150] C. Canetta, S. Guo, and A. Narayanaswamy, "Measuring thermal conductivity of polystyrene nanowires using the dual-cantilever technique," *Rev. Sci. Instrum.*, vol. 85, no. 10, p. 104901, Oct. 2014.
- [151] D. Li, Y. Wu, P. Kim, L. Shi, P. Yang, and A. Majumdar, "Thermal conductivity of individual silicon nanowires," *Appl. Phys. Lett.*, vol. 83, no. 14, p. 2934, 2003.
- [152] J. Lim, K. Hippalgaonkar, S. C. Andrews, A. Majumdar, and P. Yang, "Quantifying surface roughness effects on phonon transport in silicon nanowires," *Nano Lett.*, no. 12, pp. 2475–2482, 2012.
- [153] L. Shi, D. Li, C. Yu, W. Jang, D. Kim, Z. Yao, P. Kim, and A. Majumdar, "Measuring thermal and thermoelectric properties of one-dimensional nanostructures using a microfabricated device," *J. Heat Transfer*, vol. 125, no. 5, p. 881, 2003.
- [154] H. Dai, J. H. Hafner, A. G. Rinzler, D. T. Colbert, and R. E. Smalley, "Nanotubes as nanoprobes in scanning probe microscopy," *Nature*, vol. 384, pp. 147–150, 1996.
- [155] J. Yang, S. Meng, L. Xu, and E. G. Wang, "Water adsorption on hydroxylated silica surfaces studied using the density functional theory," *Phys. Rev. B - Condens. Matter Mater. Phys.*, vol. 71, pp. 1–12, 2005.
- [156] K. Bi, A. Weathers, S. Matsushita, M. T. Pettes, M. Goh, K. Akagi, and L. Shi, "Iodine doping effects on the lattice thermal conductivity of oxidized polyacetylene nanofibers," *J. Appl. Phys.*, vol. 114, no. 19, p. 194302, 2013.
- [157] A. Weathers, K. Bi, M. T. Pettes, and L. Shi, "Reexamination of thermal transport measurements of a low-thermal conductance nanowire with a suspended micro-device," *Rev. Sci. Instrum.*, vol. 84, no. 8, p. 084903, Aug. 2013.
- [158] K. Esfarjani, G. Chen, and H. T. Stokes, "Heat transport in silicon from first-principles calculations," *Phys. Rev. B*, vol. 84, no. 8, p. 085204, Aug. 2011.
- [159] T. Luo, J. Garg, J. Shiomi, K. Esfarjani, and G. Chen, "Gallium arsenide thermal conductivity and optical phonon relaxation times from first-principles calculations," *Europhys. Lett.*, vol. 101, no. 1, p. 16001, Jan. 2013.
- [160] D. Macgowan and D. J. Evans, "A comparison of NEMD algorithms for thermal conductivity," *Phys. Lett. A*, vol. 117, no. 8, pp. 5–7, 1986.

- [161] A. Henry, G. Chen, S. J. Plimpton, and A. Thompson, “1D-to-3D transition of phonon heat conduction in polyethylene using molecular dynamics simulations,” *Phys. Rev. B*, vol. 82, no. 14, p. 144308, Oct. 2010.
- [162] T. Luo, K. Esfarjani, J. Shiomi, A. Henry, and G. Chen, “Molecular dynamics simulation of thermal energy transport in polydimethylsiloxane,” *J. Appl. Phys.*, vol. 109, no. 7, p. 074321, 2011.
- [163] T. Zhang and T. Luo, “High-contrast, reversible thermal conductivity regulation utilizing the phase transition of polyethylene nanofibers,” *ACS Nano*, no. 9, pp. 7592–7600, 2013.
- [164] H. Sun, “COMPASS: An ab Initio force-field optimized for condensed-phase applications s overview with details on alkane and benzene compounds,” *J. Phys. Chem. B*, vol. 5647, no. 98, pp. 7338–7364, 1998.
- [165] Z. Wang, J. A. Carter, A. Lagutchev, Y. K. Koh, N.-H. Seong, D. G. Cahill, and D. D. Dlott, “Ultrafast flash thermal conductance of molecular chains,” *Science*, vol. 317, no. 5839, pp. 787–90, Aug. 2007.
- [166] T. Luo and J. R. Lloyd, “Non-equilibrium molecular dynamics study of thermal energy transport in Au–SAM–Au junctions,” *Int. J. Heat Mass Transf.*, vol. 53, no. 1–3, pp. 1–11, Jan. 2010.
- [167] T. Luo and J. R. Lloyd, “Molecular dynamics study of thermal transport in GaAs-self-assembly monolayer-GaAs junctions with ab initio characterization of thiol-GaAs bonds,” *J. Appl. Phys.*, vol. 109, no. 3, p. 034301, 2011.
- [168] M. N. Luckyanova, J. Garg, K. Esfarjani, A. Jandl, M. T. Bulsara, A. J. Schmidt, A. J. Minnich, S. Chen, M. S. Dresselhaus, Z. Ren, E. a Fitzgerald, and G. Chen, “Coherent phonon heat conduction in superlattices,” *Science*, vol. 338, no. 6109, pp. 936–9, Nov. 2012.
- [169] X. Wu and T. Luo, “The importance of anharmonicity in thermal transport across solid-solid interfaces,” *J. Appl. Phys.*, vol. 115, no. 1, p. 014901, Jan. 2014.
- [170] P. Li, L. Hu, A. J. H. McGaughey, and S. Shen, “Crystalline polyethylene nanofibers with the theoretical limit of Young’s modulus,” *Adv. Mater.*, vol. 26, no. 7, pp. 1065–70, Feb. 2014.
- [171] C. Yu, L. Shi, Z. Yao, D. Li, and A. Majumdar, “Thermal conductance and thermopower of an individual single-wall carbon nanotube,” *Nano Lett.*, vol. 5, pp. 1842–1846, 2005.
- [172] A. L. Moore, M. T. Pettes, F. Zhou, and L. Shi, “Thermal conductivity suppression in bismuth nanowires,” *J. Appl. Phys.*, vol. 106, no. 3, p. 034310, 2009.

- [173] C. Yu, S. Saha, J. Zhou, L. Shi, A. M. Cassell, B. A. Cruden, Q. Ngo, and J. Li, "Thermal contact resistance and thermal conductivity of a carbon nanofiber," *J. Heat Transfer*, vol. 128, no. 3, p. 234, 2006.
- [174] G. R. McGee, M. H. Schankula, and M. M. Yovanovich, "Thermal resistance of cylinder-flat contacts: Theoretical analysis and experimental verification of a line-contact model," *Nucl. Eng. Des.*, vol. 86, pp. 369–381, 1985.
- [175] V. Bahadur, J. Xu, Y. Liu, and T. S. Fisher, "Thermal resistance of nanowire-plane interfaces," *J. Heat Transfer*, vol. 127, p. 664, 2005.
- [176] R. Chen, A. I. Hochbaum, P. Murphy, J. Moore, P. Yang, and A. Majumdar, "Thermal conductance of thin silicon nanowires," *Phys. Rev. Lett.*, vol. 101, no. 10, p. 105501, Sep. 2008.
- [177] R. F. Egerton, P. Li, and M. Malac, "Radiation damage in the TEM and SEM," *Micron*, vol. 35, pp. 399–409, 2004.
- [178] Y.-W. Lan, W.-H. Chang, Y.-C. Chang, C.-S. Chang, and C.-D. Chen, "Effect of focused ion beam deposition induced contamination on the transport properties of nano devices," *Nanotechnology*, vol. 26, no. 5, p. 055705, 2015.